An Evaluation of Critical Issues for Microhydraulic Transducers: Silicon Wafer Bonding, Strength of Silicon on Insulator Membranes and Gold-Tin Solder Bonding

by

Kevin Thomas Turner

B.S. Mechanical Engineering, The Johns Hopkins University, 1999

BARKER

Submitted to the Department of Mechanical Engineering in partial fulfillment of the requirements for the degree of

Master of Science in Mechanical Engineering

at the

MASSACHUSETTS INSTITUTE OF TECHNOLOGY

June 2001

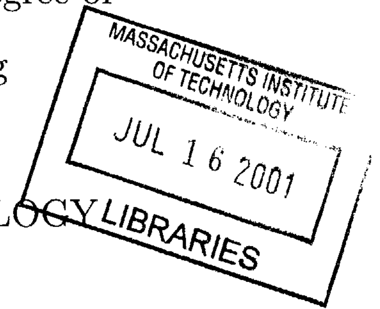

© Massachusetts Institute of Technology 2001. All rights reserved.

Author ....
Department of Mechanical Engineering
June 4, 2001

Certified by.................
S. Mark Spearing
Esther and Harold Edgerton Associate Professor of Aeronautics and Astronautics
Thesis Supervisor

Certified by.........................
Lallit Anand
Professor of Mechanical Engineering
Thesis Reader

Accepted by...............................
Ain Sonin
Chairman, Department Committee on Graduate Students

An Evaluation of Critical Issues for Microhydraulic Transducers: Silicon Wafer Bonding, Strength of Silicon on Insulator Membranes and Gold-Tin Solder Bonding

by

Kevin Thomas Turner

Submitted to the Department of Mechanical Engineering
on June 4, 2001, in partial fulfillment of the
requirements for the degree of
Master of Science in Mechanical Engineering

Abstract

Microhydraulics transducers (MHT) are a class of microelectromechanical systems (MEMS) currently being developed to produce bi-directional transducers with high power densities (500–1000 W/kg). The development of these devices, which combine microfabrication technology and piezoelectric materials, requires the use of variety of materials and fabrication technologies that are not fully developed. Three materials and structures issues, which are essential to the development of MHT devices, are silicon wafer bonding, strength of silicon-on-insulator (SOI) membranes, and gold-tin bonding. Each of these topics was addressed independently. The mechanical integrity of silicon fusion bonds as a function of processing parameters was examined using a four-point bend delamination specimen. The study showed that the specimen was effective for characterizing low toughness bonds and that certain processing conditions can have a profound impact on bond toughness. Bond toughness increased with anneal time and temperature, but, initial contacting conditions, such as time and clamping pressure, proved to have little effect on final bond toughness. The fracture strength of membranes fabricated from SOI wafers using deep reactive ion etching was experimentally measured. Results showed that the strengths of these membranes was less than that of structures etched from bulk silicon and that the strength was dependent on SOI manufacturer. Finally, a thin film gold-tin solder bond was developed to bond bulk piezoelectric material to silicon structures. The process, which uses a sputtered gold-tin eutectic alloy (80wt%Au–20wt%Sn), was refined to produce void-free bonds. Preliminary tensile tests indicated failure was likely to occur in the piezoelectric material itself or along the solder-piezoelectric material interface. The results of these three studies provide information that is essential to the development of MHT devices as well as a wide range of MEMS devices.

Thesis Supervisor: S. Mark Spearing
Title: Esther and Harold E. Edgerton Associate Professor of Aeronautics and Astronautics

Acknowledgments

The work reported in this thesis would not have been possible without the help of many people along the way. First and foremost, I would like to thank my advisor, Mark, for his guidance and advice throughout this work. The help of all the students, staff and faculty on the MHT project is greatly appreciated. In particular, I would like to thank Lodweyk Steyn and Hanqing Li for their help in the tedious task of specimen fabrication and providing general advice regarding microfabrication. Also, numerous discussions with Dave Roberts and Yu-Hsuan Su were indispensable in completing this work. The assistance and guidance provided by Arturo Ayon allowed the study of silicon fusion bond strength to be completed. The help of several undergraduates, Nate Fitzgerald, Rogelio Garcia, Federico Gutierrez, and John Seminatore, was essential in carrying out the silicon fracture and fusion bond tests. Last, but certainly not least, I would like to express my gratitude to the staff of the Microsystems Technology Laboratory (MTL), the Active Materials and Structures Laboratory (AMSL), and the Technology Laboratory for Advanced Composites (TELAC), particularly Dave Robertson and John Kane, for their assistance throughout.

This work was sponsored by DARPA under contract DAAG55-98-1-0361.

Contents

1 Introduction **17**

1.1 Motivation 17

1.2 Objectives 19

1.3 Scope of Thesis 20

2 Silicon Wafer Bonding **23**

2.1 Introduction 23

2.2 Background 25

2.2.1 Silicon Fusion Bonding 25

2.2.2 Mechanical Characterization of Bond Strength 27

2.3 Test Specimen 30

2.4 Crack Initiation and Propagation 33

2.4.1 Crack Initiation 33

2.4.2 Bond Area Reduction 34

2.4.3 Chevron Notch 35

2.5 Specimen Fabrication 37

2.6 Experimental Procedure 40

2.6.1 Test Apparatus 40

2.6.2 Alignment 40

2.6.3 Test Procedure 44

2.7 Test Results 44

2.7.1 Effectiveness of Specimen 45

2.7.2 Effect of Process Parameters on Bond Quality 47

2.8 Conclusion and Recommendations 49

3 Silicon-on-Insulator Membranes **51**

3.1 Introduction 51

3.2 Background 53

3.3 Experimental Method 54

3.3.1 Specimen Geometry and Loading 55

3.3.2 Specimen Fabrication 57

3.3.3 Test Apparatus 59

3.3.4 Test Procedure 62

3.4 Finite Element Modeling and Data Reduction 64

3.5 Results 67

3.6 Conclusions 73

4 Gold-Tin Bonding **75**

4.1 Introduction 75

4.2 Bond Selection 76

4.2.1 Bond Requirements 76

4.2.2 Bonding Techniques 77

4.3 Gold-Tin Bonding Background 79

4.3.1 Applications 79

4.3.2 Material Properties 80

4.3.3 Process Overview 81

4.3.4 Mechanical Integrity 83

4.4 Device Assembly 84

4.5 Bonding Process 87

4.6 Qualitative Evaluation of Bond Quality 90

4.7 Tensile Tests 94

4.7.1 Experimental Procedure 94

4.7.2 Results 95

4.8 Conclusions and Recommendations 99

5 Conclusions and Recommendations 101

A Photolithography Masks 103

B Finite Element Code 109

List of Figures

1-1 A typical MHT device: a piezoelectric micropump. 18

2-1 Techniques to evaluate bond strength. 27

2-2 Schematic of four-point bend delamination specimen. 30

2-3 Ideal load-displacement curve. 32

2-4 Procedure for creating precrack. 34

2-5 Effect of bonded area ratio on toughness. 36

2-6 Standard and chevron notch specimen geometries. 37

2-7 IR image of a bonded wafer pair. 39

2-8 Micrograph of specimen showing interfacial notch. 39

2-9 Strain-displacement for a misaligned specimen. 41

2-10 Schematic of misalignment. 42

2-11 Schematic of alignment fixture. 42

2-12 Strain-displacement for an aligned specimen. 43

2-13 Load-displacement plot for a typical test. 45

2-14 Chevron-notch specimen failure. 46

2-15 Bond toughness as a function of anneal temperature. 47

2-16 Bond toughness as a function of anneal time. 48

2-17 Bond toughness as a function of contacting pressure. 49

2-18 Bond toughness as a function of contacting time. 50

3-1 A SEM micrograph showing a typical MHT drive membrane. 52

3-2 Fracture strength measurement approach. 55

3-3 Schematic of test specimen for measurement of fracture strength. . . 56

3-4 Potential silicon membrane loading configurations. 57
3-5 Different approaches for etching fillets, (a) 'standard', (b) 'alternate'. 58
3-6 Silicon fracture test machine. 60
3-7 Effect of misalignment on maximum stress in a specimen. 62
3-8 Typical fillet radius, (a) viewed from the top, (b) cross-section view. . 63
3-9 Typical defect in fillet radius. 64
3-10 Finite element model of specimen. 65
3-11 Typical shape of etched fillet radius. 66
3-12 Effect of b/a ratio on maximum stress. 67
3-13 Strength results for specimens with oxide. 70
3-14 Strength results for specimens without oxide. 70

4-1 Gold-tin equilibrium phase diagram. 80
4-2 Final MHT bonding process. 85
4-3 Bond pressure as a function of tether width and piezoelectric element oversize. 86
4-4 Deposited metal layers used to fabricate the gold-tin solder bonds. . . 88
4-5 Solder bonding jig. 89
4-6 Temperature and pressure cycle to complete bond. 91
4-7 Two examples of poor bonding, (a) due to the presence of trapped gas, (b) due to poor cleaning. 92
4-8 Void-free AuSn bond of silicon to silicon. 93
4-9 Void-free AuSn bond of PZT-5H to silicon. 93
4-10 Void-free AuSn bond PZN-PT to silicon. 94
4-11 Tensile specimen geometry. 95
4-12 Tensile specimen, (a) mounted to studs, (b) mounted in test machine. 96
4-13 Micrograph of fracture surface of specimen C. 97
4-14 Micrograph of fracture surface of specimen B. 98

A-1 Mask layout to define shallow grooves in standard 4-point specimen. . 104
A-2 Mask layout to define shallow grooves in 4-point chevron specimen. . 105

A-3 Mask layout to define deep trench in 4-point specimens. 106
A-4 Mask layout to define alignment marks and specimen edges in device layer of fracture strength specimen. 107
A-5 Mask layout to define deep trenches in handle wafer of fracture strength specimen. 108

List of Tables

3.1 Process conditions of fabricated wafers. 68

3.2 Fracture strength values of tested wafers. 69

3.3 Consolidated fracture strength values. 69

4.1 Room temperature mechanical Properties of 80 wt.% Au and 20 wt% Sn alloy. 81

4.2 Typical processing conditions for AuSn preform solder bonds. 82

4.3 Typical processing conditions for AuSn thin-film solder bonds. 83

4.4 Tensile test results. 96

Chapter 1

Introduction

1.1 Motivation

A class of Microelectromechanical Systems (MEMS) known as Micro-Hydraulic Transducers (MHT) is currently being developed to produce bi-directional transducers with high power densities (500–1000 W/kg) [1], [2], [3], [4]. The transducers can act as actuators by transforming electrical energy into mechanical energy or as energy harvesting devices by transforming mechanical energy into electrical energy. Potential applications include actuators for distributed arrays and miniature robotics, as well as energy harvesting devices for recovery of electrical energy from human motion. Current efforts are focused on developing and validating the technology required to produce such devices.

MHT devices utilize piezoelectric material as the conversion medium between electrical and mechanical energy. Piezoelectric materials have high bandwidth and are capable of high power output, if this bandwidth is utilized. For this reason, MHT devices are designed to operate at high frequencies (tens of kilohertz) and thus require small length scales to achieve high structural natural frequencies. Microfabrication technology allows mechanical structures to be fabricated with the required dimensions. The combination of high frequencies and piezoelectric material leads to a device with high power output, however, most applications require a relatively low frequency mechanical input/output. In MHT devices, the high frequency operation

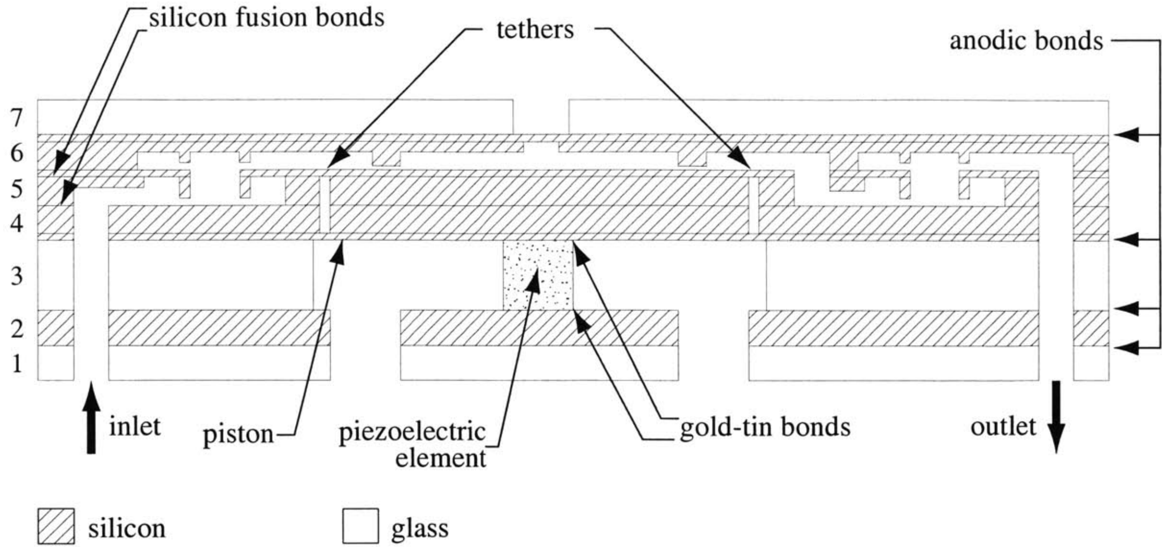

Figure 1-1: A typical MHT device: a piezoelectric micropump.

of the piezoelectric element is rectified to a more useful low frequency mechanical motion through the use of a fluid transfer medium and a series of valves. By incorporating piezoelectric materials, hydraulics, and microfabrication technology, high power density transducers can be produced.

A cross-section of a piezoelectrically driven micropump is shown in Figure 1-1. While this a specific MHT device, it illustrates the basic design and fabrication approach for a wide range of MHT devices [5]. MHT devices are fabricated by bonding multiple bulk micromachined wafers. Moving mechanical components, such as pistons, membranes, and valves, which require precise dimensional control, are micromachined from silicon and silicon-on-insulator (SOI) wafers using a deep reactive ion etching (DRIE) process. The outer packaging layers (layers 1 and 7) and the center isolation layer (layer 3) are fabricated from borosilicate glass wafers, specifically Pyrex 7740, using either conventional diamond drilling or ultrasonic machining techniques. A unique feature of MHT devices is the use of bulk piezoelectric material, rather than thin films. The piezoelectric elements are fabricated from bulk piezoelectric disks, which are ground and polished to the desired thickness and then subsequently core drilled or diced into smaller elements. Assembly of the device is completed through a series of bonding steps that begins with bonding of the silicon

layers to one another. Bonding between the silicon layers is accomplished using silicon fusion bonding. The silicon structures are then bonded to the glass packaging and isolation layers using field-assisted glass bonding (anodic bonding) [6]. Coincident with the bonding of the glass isolation layer to the silicon layers, the piezoelectric element must be inserted and bonded to the lower silicon layer and the silicon piston. A gold-tin solder bond provides the mechanical and electrical connection between the silicon layers and the piezoelectric elements.

The fabrication of the device involves a multitude of different processes, each with its own unique challenges and limitations. In order to ensure a robust and reliable device, the fabrication technologies outlined above must be well understood and controlled. A direct coupling exists between fabrication route and the performance and reliability of the device. While technologies such as anodic bonding have seen widespread use in MEMS devices and are well developed and robust, other technologies employed in the device are not. In order for the development of MHT devices, as well as other MEMS devices, to progress successfully, issues pertaining to silicon fusion bonding, deep reactive ion etched silicon-on-insulator membranes, and bonding of bulk piezoelectric material to silicon must be addressed.

1.2 Objectives

The primary goal of this work is to address the materials and structures issues that are most critical to the development of MHT devices. This overall goal, the nature of the design and fabrication of the device, and the existing technology has resulted in three main objectives for this work. These objectives are diverse and distinct from one another, but contribute to the common goal of developing MHT devices. The three main objectives of this work are:

- To develop a reliable technique for measuring wafer bond quality and to examine the effect of various processing conditions on silicon fusion bond toughness.

- To measure the mechanical strength of membranes fabricated from SOI wafers

using deep reactive ion etching and to make recommendations regarding the fabrication and design of such structures.

- To develop a thin film gold-tin solder bond to secure piezoelectric elements to the silicon structure of the device and to evaluate the mechanical integrity of the bond.

While the overall goal of this work is clearly to validate the technology necessary for the development of MHT devices, a subsequent goal has resulted from the need to characterize accurately various materials properties. The lack of standard test techniques for measuring mechanical properties of MEMS materials and structures requires that test structures and specimens be developed to measure accurately the quantity of interest. Thus, a secondary goal of this work is to develop and validate test methods and tools, which not only provide the information critical to the design of MHT devices, but also have the ability to be applied to a variety of MEMS materials.

1.3 Scope of Thesis

The outline of this thesis is straightforward and follows the objectives outlined in Section 1.2. Chapter 2 addresses the use of a four-point bend delamination specimen to quantify silicon fusion bond quality. It gives a brief review of silicon fusion bonding as well as test techniques commonly employed to measure bond quality. The chapter details the four-point bend specimen employed, the specimen fabrication and bonding process, and the test method. Results for silicon fusion bond toughness as a function of processing conditions are presented and recommendations are made regarding the use of the four-point specimen for evaluation of bond quality. Chapter 3 discusses issues pertaining to the strength of thin silicon membranes fabricated from SOI wafers by deep reactive ion etching. A review of previous work pertaining to the mechanical strength of single crystal silicon is given, followed by an outline of the process employed in the fabrication of membranes for MHT devices. Details are given with regard to specimen fabrication, test method and test apparatus. Experimental

results that were obtained are given as well as design recommendations. Chapter 4 covers the development and testing of a thin film gold-tin eutectic solder bond. Previous work with regard to gold-tin bonding and bonding for microsystems is discussed. Specifics with regard to the bond material selection, process development and refinement are given. Qualitative results demonstrating void-free bonding and quantitative results obtained from simple tensile tests are presented. The final chapter, chapter 5, gives overall recommendations and conclusions regarding the materials and structures issues for MHT devices discussed.

Chapter 2

Silicon Wafer Bonding

2.1 Introduction

In recent years, the number of MEMS devices that are fabricated by bonding multiple bulk micromachined wafers has been steadily increasing. The success of these multi-wafer devices relies on advances in etching technology and reliable bonding between wafers [7], [8], [9]. MHT devices are a typical example and rely on achieving wafer scale silicon-silicon and silicon-glass bonds. Many devices that are currently under development, [10], as well as some devices that are currently produced commercially, [11], [12], employ wafer scale-bonding to produce complex microstructures or to meet packaging requirements. Since silicon remains the material of choice for bulk micromachining operations, a significant amount of work has been devoted to developing robust bonds between etched silicon wafers.

A variety of techniques exist to bond two or more silicon wafers to one another. The more popular techniques include gold-silicon eutectic bonding, anodic bonding and silicon fusion bonding (silicon direct bonding). Gold-silicon eutectic bonding involves depositing a thin layer of gold on one of the wafers to be bonded, placing the wafers in contact, and subsequently heating to above the Au-Si eutectic temperature, 363°C. Upon cooling, the Au-Si eutectic alloy solidifies and secures the wafers together. This bonding method is attractive because it offers a low processing temperature and is electrically and thermally conductive. However, it can be difficult to

achieve large area void-free bonds and the large thermal expansion mismatch between gold and silicon can lead to stresses in the bonded wafers. Anodic bonding, while traditionally used to bond silicon to borosilicate glass wafers, has recently been employed to bond silicon wafers to one another with a thin glass intermediate layer [13], [14]. This is accomplished by either sputtering or evaporating a thin layer of borosilicate glass that has a thermal expansion coefficient close to that of silicon (typically Pyrex 7740 or Schott 8329) on one of the surfaces to be bonded. The wafers are then contacted, heated to 300-500°C, and a potential of 800-1200 V is applied across the interface. A strong hermetic bond is formed at the interface with relatively little residual stress. However, the bond is not electrically conductive and the strength is often limited by that of the glass. Silicon fusion bonding (silicon direct bonding) requires no intermediate bonding layers and can be accomplished between two mirror-polished silicon wafers. Two wafers, which have been cleaned thoroughly, are brought into contact and then annealed at a temperature in the range of 1000°C. The absence of an intermediate layer eliminates thermally induced residual stresses, and bonds with strengths that approach that of silicon can be achieved. Unfortunately, the high anneal temperature prohibits processing steps, such as the deposition of metals, or the integration of sensitive electronics prior to the bonding step.

Despite the high anneal temperatures that are required for silicon fusion bonding, it has gained widespread acceptance in the fabrication of MEMS devices. The fact that it has the potential to yield bonds with mechanical properties virtually identical to silicon itself without inducing residual stresses has made it a very appealing option in device design. Significant effort has been devoted towards characterizing bond integrity as a function of process conditions. A review of this work is given in Section 2.2. This work has demonstrated the profound effect processing route can have on bond integrity and has highlighted the fact that it may be possible to achieve high strength bonds at lower temperatures. The previous work has examined a variety of process conditions and has used various mechanical testing techniques to measure bond integrity. The current study builds on previous work, [15], [16], and focuses on employing a four-point flexure delamination specimen to measure reliably silicon

fusion bond toughness as a function of processing conditions. The study specifically examines the effect of contacting conditions, anneal time, and anneal temperature on bond toughness.

2.2 Background

2.2.1 Silicon Fusion Bonding

There has been an intense effort over the past 15 years to develop wafer scale silicon-silicon bonds where the wafers have a thermally grown oxide or a thin native oxide on the surfaces to be bonded. The concept of bonding silicon wafers with a thermally grown oxide layer at the interface using a room temperature contacting step followed by a high temperature anneal was first demonstrated by Lasky et al. [17], [18] at IBM in 1985 as a means of fabricating silicon-on-insulator wafers for electronic applications. At approximately the same time, Shimbo and colleagues at Toshiba reported bonding silicon wafers with a native oxide and hydrophilic surfaces at room temperature [19]. Shimbo et al. reported that following an anneal step at 1000°C, the bond strength reaches that of bulk silicon and the electrical resistivity across the interface is low. This early work sparked interest in the field that has continued to the present day. A significant number of papers have been published that examine a variety of different topics relating to silicon-silicon direct bonding. Several review articles [20], [21] as well as a book [22] on the subject offer a comprehensive review of direct wafer bonding. A brief review of the work relevant to the current study, concerning bonding of hydrophilic wafers without a thermally grown oxide on a surface, is provided below.

The silicon fusion bonding process is relatively well developed and in general consists of three basic steps [20]:

I. The surfaces of two flat, mirror polished wafers are prepared to achieve the desired surface conditions. On wafers with a thin native oxide, various treatments are used to produce a hydrophilic surface on the wafer.

II. The two wafers are brought into contact at room temperature in a suffi-

ciently clean environment. This step can be carried out in air, an inert atmosphere, or a vacuum. The most critical factor is the cleanliness of the environment, which is essential in avoiding particles between the wafers.

III. Following the room temperature bonding step, the wafers are bonded with weak van der Waals or hydrogen bonds. These bonds are sufficient to adhere the wafers to one another, but have inadequate strength for most applications. To achieve the full strength, the wafer pair is annealed at high temperatures near 1000°C. The result is covalent bonds at the interface which are approximately two orders of magnitude stronger than the initial secondary bonds.

While the general steps are well known, the literature reports a wide array of processing parameters that may be employed at each step. The discussion here is limited to the work that has examined the effect of varying the anneal time and temperature.

The high temperature anneal step is a critical step and essential to achieving robust bonds. The length and temperature of the anneal step has been varied in previous work to examine the effect on bond quality. The initial work by Shimbo, [19] et al. demonstrated the profound effect of anneal temperature. Bonds were fabricated using a 2 hour anneal, at temperatures from 200 to 1200°C. Bond strength measurements indicated that above 300°C, the strength increased with increasing temperature. While the increase was monotonic, the strength reached a plateau between 600 and 800°C and then increased and reached another plateau above 1000°C. Work by Tong et al., [23] yielded similar results for the bond energy as a function of temperature. Bond energy was measured for specimens annealed for 100 hours at temperatures from 25 to 900°C. Between 150 and 800°C the bond energy was approximately half of the value when annealed at high temperatures. Above 800°C the strength increased rapidly and reached its maximum value at 900°C.

The effect of annealing time has been investigated less than that of annealing temperature. Work has been done to characterize bond energy as a function of time for temperatures of 43°C and 150°C, [23]. Results indicated that the bond

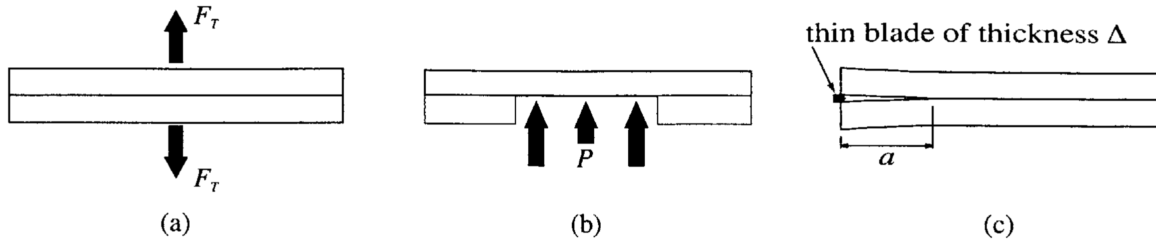

Figure 2-1: Techniques to evaluate bond strength.

energy approached a saturated value, which was more than an order of magnitude less than the bond energy obtained from a high temperature anneal, after approximately 100 hours. A more complete study was conducted in which temperatures from 195 to 700°C and times up to 1106 hours were investigated [24]. Tensile tests demonstrated that at 700°C, the strength was increased by 2.5 times when the anneal time was increased from 1 to 66 hours. However, the strength of specimens annealed at 195°C for 1106 hours only had strengths that were approximately two thirds of the strength that could be achieved by annealing for 66 hours at 700°C. This data, while not comprehensive, does indicate the possibility of achieving robust silicon-silicon fusion bonds at lower temperatures.

2.2.2 Mechanical Characterization of Bond Strength

The quality of silicon fusion bonds has been examined qualitatively and quantitatively using a variety of non-destructive as well as destructive techniques. The discussion here is limited to quantitative techniques that provide either a bond failure stress or a bond toughness value. While there are a range of techniques available to measure bond strength or toughness, three tests in particular have been used in the characterization of silicon fusion bond quality. These tests, which are illustrated in Figure 2-1, are tensile tests, pressure-burst tests and the crack opening method.

The tensile test, which is illustrated in Figure 2-1(a), is attractive due to the ease of specimen fabrication and testing. However, tensile tests may present problems in quantifying the process because the failure load, F_T, is not only a function of the material properties at the interface, but also a function of geometry. Thus, defects

in the bond or damage at the edges due to specimen preparation and handling can lead to low failure stresses with a significant degree of scatter in the data set. In addition, the stress-state at the interface may be dependent on the exact specimen geometry employed, which makes comparing data between different tests difficult. To eliminate the possibility of edge damage, researchers have used patterned wafers to bond selective areas of a wafer [25]. These wafers were then diced, such that the bonded region was far from the dicing path. This eliminated the chance of introducing flaws at the bonded interface that can lead to erroneous failure loads. Despite these efforts though, significant scatter still existed in the reported strength values. Abe et al. utilized a tensile loading as well, but adopted a different geometry in an attempt to eliminate problems such as residual damage. The tests were conducted on a bonded pair, where one layer had been thinned to 2-3 μm. A stud with a 5.7 mm^2 bonding area was affixed using epoxy to the surface of the thinned wafer and subsequently pulled in tension. Since the layer was thin, the measured fracture load was primarily controlled by the bond between the silicon layers. The data obtained showed relatively little scatter, but in strong bonds, failure would occur in the adhesive layer which secures the stud to the silicon.

The pressure-burst test, which is shown in Figure 2-1(b) has been employed to measure failure stress of silicon fusion bonds [19]. Fabrication of the test structures was straightforward and was accomplished by etching through holes in one of the wafers to be bonded. Following bonding, the wafer pair was diced into specimens and the dies were mounted in a fixture which allowed a hydrostatic oil pressure to be applied from beneath. The failure stress was calculated from the applied pressure, P, at failure. While specimen fabrication is simple, the stress state at the interface is complicated and difficulties similar to those of the tensile test may be encountered.

The limitations and complications of these stress-based approaches are clear and well documented. Mazara et al. [26] recognized the difficulties of these tests and employed the double cantilever beam geometry shown in Figure 2-1(c) to quantify the strength of wafer bonds for silicon-on-insulator fabrication. The test, also known as the crack opening method, is accomplished by inserting a thin blade between the

wafers and measuring the extent of the crack propagation. Crack length is typically measured using IR imaging from above or with an optical microscope from the side. The distance the crack propagates can be directly related to bond quality through an energy balance. Based on the thickness of the blade, Δ, the thickness of the bonded layers, h, the elastic properties of the layers, E and ν, and the crack length, a, the critical strain energy release rate, G_c, or the bond toughness can be calculated as:

$$G_c = \frac{3}{16}\frac{\Delta^2 h^3}{a^4}\frac{E}{1-\nu^2}. \tag{2.1}$$

Equation 2.1 is for the specific case where the bonded layers have the same thickness and elastic properties. Similar expressions exist for the general case where the layers are different materials and have different dimensions [27]. Many researchers, who have employed this technique, report specific surface energy values, γ_s rather than the critical strain energy release rate. The two quantities are closely related and simply differ by a factor of two, where $G_c = 2\gamma_S$.

The crack opening method is advantageous because it offers a well defined loading at the interface. The extent of crack propagation is largely unaffected by small flaws at the edges and in general the measured toughness is less sensitive to geometry than the failure stress values in the tensile and pressure tests. However, the technique is not without its limitations and difficulties. The most important concern is the fourth order dependence of G_c on crack length [8], which is seen in equation 2.1. Crack length is a difficult quantity to measure accurately and slight errors in measurement can lead to large errors in the G_c value. In addition, it has been observed that the crack length is dependent on time and humidity, which can make repeatability difficult [28]. Finally, in well-bonded wafers, insertion of the blade is difficult and often leads to wafer fracture. Despite the limitations, it has been the most widely used test in the characterization of silicon-silicon wafer bonds up to this point.

An alternative technique to measure critical strain energy release rate is a four-point bend delamination specimen. The specimen, which was developed for evaluating bimaterial interfaces, does not require the measurement of crack length, [27],[29],[30].

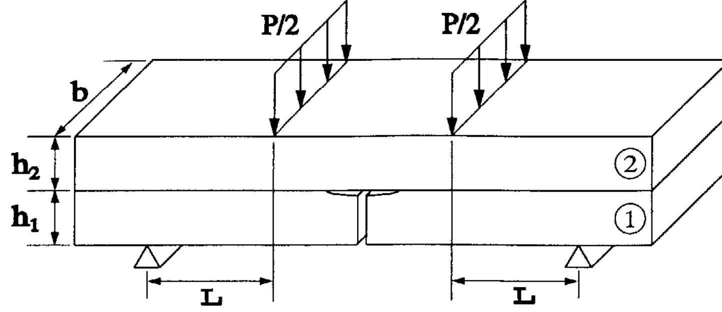

Figure 2-2: Schematic of four-point bend delamination specimen.

The critical strain energy release rate can be determined from a critical load and the dimensions and elastic properties of the specimen. The specimen offers a well-defined loading similar to that of the double cantilever beam and is relatively simple to fabricate. The specimen has not been employed previously to characterize silicon fusion bonds, but has been used to quantify the integrity of wafer-scale gold-gold thermocompression bonds, [31]. Based on the literature, the specimen appears to be an attractive alternative to the crack opening method.

2.3 Test Specimen

The four point bend specimen, which is shown schematically in Figure 2-2, consists of two bonded layers with a central notch and symmetric interfacial pre-cracks. The loading configuration creates a constant moment between the inner loading points. Thus, while the crack is within the inner loading points, the strain energy release rate, G, is independent of crack length. The energy release rate for the case where the crack is within the inner loading points can be determined analytically by calculating the difference in the strain energy in the uncracked and cracked beam [29]. Using Euler-Bernoulli beam theory, the strain energy release rate is expressed as

$$G = \frac{M^2}{2E_2'b}\left(\frac{1}{I_2} - \lambda\frac{1}{I_c}\right) \tag{2.2}$$

where M is the moment between the inner loading points and can be written in terms of the applied load, P, and the distance between the inner and outer loading points,

L.

$$M = PL/2 \tag{2.3}$$

The additional terms of equation 2.2 are simply functions of the geometry and the elastic properties of the specimen layers, and are defined as

$$\lambda = \frac{E_2'}{E_1'} \tag{2.4}$$

$$I_c = b\left(\frac{1}{12}h_1^3 + \frac{1}{12}h_2^3\lambda + \frac{\lambda h_1 h_2 (h_1 + h_2)^2}{4(h_1 + \lambda h_2)}\right) \tag{2.5}$$

$$I_2 = \frac{1}{12}bh_2^3. \tag{2.6}$$

The subscripts $1, 2$, and c refer to the properties of the lower, upper, and composite beams, respectively. The geometry is defined by the thickness of the layers, h_1, h_2, and the width, b, as shown in Figure 2-2. The appropriate choice of E' depends on the geometry of the specimen. In the case of plane stress

$$E_n' = E_n \tag{2.7}$$

and for plane strain

$$E_n' = \frac{E_n}{1 - \nu_n^2}. \tag{2.8}$$

When employing the four-point-bend delamination specimen to measure critical strain energy release rate, it is assumed that at a critical load, P_c, the strain energy release rate at the interface, G, will exceed the critical strain energy release rate (toughness) of the bond, G_c, and delamination will begin. When the interface toughness is constant, the crack will propagate at a constant load while advancing between the inner loading points. A ideal load-displacement curve for a specimen that delaminates at a critical load, P_c, is shown in Figure 2-3. As seen in Figure 2-3, the critical load can clearly be identified from the plateau in the load-crosshead displacement curve. Using the measured critical load and the dimensions and elastic properties of the specimen, critical strain energy rate can be determined using equations 2.2-2.8.

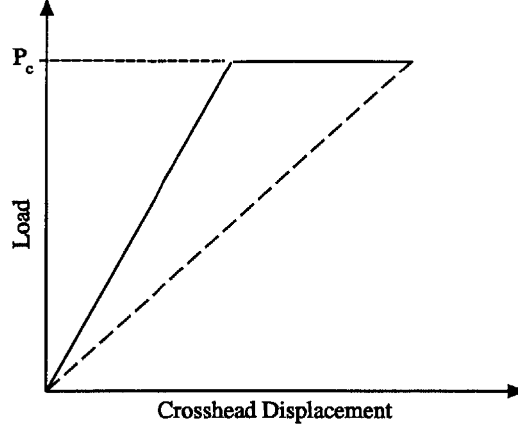

Figure 2-3: Ideal load-displacement curve.

For the current study, layers 1 and 2 are of equal thickness, h, and have the same elastic properties, E, ν. In addition, plane strain is assumed. With these conditions, the critical strain energy release rate, G_c, can be determined using

$$G_c = \frac{21}{16}\frac{P_c^2 L^2}{b^2 h^3}\frac{1-\nu^2}{E}. \tag{2.9}$$

The loading at the interface of the four-point-bend specimen is mixed-mode. The exact phase angle of loading, Ψ, which describes the ratio of mode I to mode II loading, is a function of the ratio of moduli and thickness of the bonded layers [29]. While the crack is within the inner loading points, the phase angle is independent of crack length. For the geometry employed in present study, where $E_1 = E_2, h_1 = h_2$, $\Psi \approx 40°$, which indicates slightly more tensile opening than sliding at the interface ($\frac{G_{II}}{G_I} \approx 0.85$). While the mixed-mode conditions may in fact be closer to the types of loading incurred in real devices, the mixed-mode properties of the specimen pose some challenges in testing. The principal difficulty arises from the fact that in a monolithic material, cracks tend to follow the most energetically favorable path, which is a mode I path. For the majority of applications of the four-point delamination specimen, the interface has a lower toughness than the adjoining layers, such that the crack follows the interface. However, as was stated earlier, silicon fusion bonds have the potential to achieve mechanical properties similar to those of silicon itself. Thus, in

a well-bonded specimen, the crack will not propagate along the interface, but will follow the mode I path and lead to fracture through the middle of the specimen.

2.4 Crack Initiation and Propagation

The two most difficult challenges in employing the four point bend specimen are initiating the crack at the interface and forcing the crack to follow the interface. The latter is due to the mixed-mode conditions and the fact that silicon fusion bonds can be quite strong. Crack initiation is also made difficult by the strength of the bond, but is further complicated by the scale and fabrication method of the specimens. Several different specimen design and fabrication processes were attempted to try to overcome these challenges.

2.4.1 Crack Initiation

Typically, cracks are initiated at the interface of the four-point-bend specimen using a two-step process [27],[31]. First, a cut is made in the lower layer of specimen to define the position of the central notch. The cut is made using a thin saw blade and the depth is set so that the resulting cut falls short of the interface. Following the cut, the specimen is loaded in three-point bending, with the center loading point acting on the upper layer and positioned above the notch that was previously cut. Upon loading in three point bending, a crack initiates at the tip of the saw cut and propagates and branches into the interface. The crack arrests a short distance from the notch since the driving force at the interface diminishes with distance from the center loading point. This technique works well for bimaterial specimens or specimens with intermediate bonding layers. However, in a silicon fusion bond specimen it is unlikely that the crack would deflect at the interface, but would rather continue past the interface into the upper layer.

Recognizing this limitation, an alternate technique for precracking the specimen was developed. Figure 2-4 illustrates the basic approach that was employed. Prior to bonding, a trench was etched in the lower layer of the specimen. The layers were

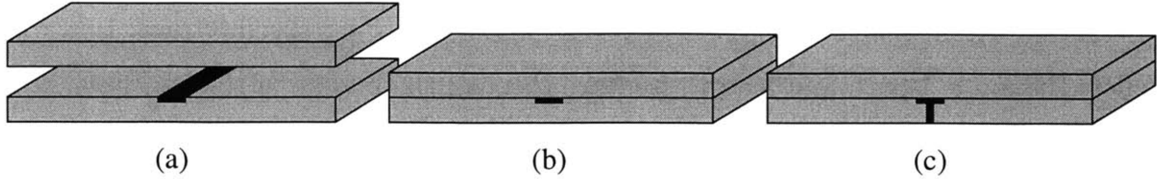

Figure 2-4: Procedure for creating precrack.

subsequently bonded and then a saw cut was made that intersected the previously etched trench. The presence of the trench allows the cut to be made without damaging the upper layer of the specimen. The combination of an etched trench and saw cut form the central notch and precrack.

2.4.2 Bond Area Reduction

The mixed-mode conditions at the interface coupled with the potential strength of silicon fusion bonds created a situation in which it was difficult to force the crack to follow the interface. Analysis indicates for geometries similar to the one used in this study that the ratio of interface to layer toughness determines whether the crack will follow the interface or proceed into the layer above [32]. A novel approach, which entailed reducing the effective interface toughness via a bond area reduction, was employed to alter the ratio of interface toughness to layer toughness. The hope was that by reducing the interface toughness sufficiently, it would become energetically favorable for the crack to propagate along the interface rather than along the mode I path. The bond area reduction at the interface was accomplished by etching shallow grooves, 1-3 μm in depth, on one of the bonding surfaces. The grooves, which run parallel to the length of the specimen, prevent bonding in certain areas, but do not significantly alter the stiffness of the 525 μm thick layer.

By reducing the bond area at the interface, the effective 'global' bond toughness is reduced. While the areas that are bonded have the true interface toughness, the toughness that is measured using the four-point bend specimen is lower because of the reduced area. Toughness, or critical strain energy release rate, for a specimen of

constant width is defined as

$$G = \frac{1}{b}\frac{\partial U}{\partial a} \quad (2.10)$$

where U is the stored energy, b is the width of the specimen, and a is the crack length. Since the grooves are parallel to the length of the specimen, the grooves effectively reduce the width of the specimen in equation 2.10 but do not affect the stored energy. Noting this fact and examining equation 2.10, it is seen that the 'true' toughness of the interface can be calculated from the measured toughness of a specimen with reduced bond area,

$$G_{true} = \frac{1}{AR} G_{measured} \quad (2.11)$$

where AR is the area ratio of the specimen and is defined as the bonded area divided by total specimen area. The validity of equation 2.11 was verified experimentally by testing specimens with various area ratios that were processed under identical conditions. Figure 2-5 shows the results of two such sets of specimens that have been corrected using equation 2.11. In Figure 2-5, specimen set A, which contains 7 specimens, has a mean of 1.51 J/m^2 and a coefficient of variation of 0.05, while set B, which contains 5 specimens, has a mean of 1.57 J/m^2 and a coefficient of variation of 0.04. These results clearly validate equation 2.11. In the current study, bonded area ratios, AR, ranging from 0.1 to 0.9 were utilized so that specimens with a range of interface toughness could be tested.

2.4.3 Chevron Notch

As will be discussed in detail in Section 2.7.1, the use of the etched trench and central notch as the crack initiation site proved successful for specimens with low to intermediate interface toughness values. However, in well bonded specimens, the crack would fail to initiate in the interface and would fracture via a crack propagating through the upper layer. A chevron notch geometry was employed at the end of the bonded areas in an attempt to alleviate this problem. Figure 2-6 illustrates the geometry of the chevron notch specimen as compared to the initial specimen geometry. In the standard specimen, the intersection between the bonded areas and the central

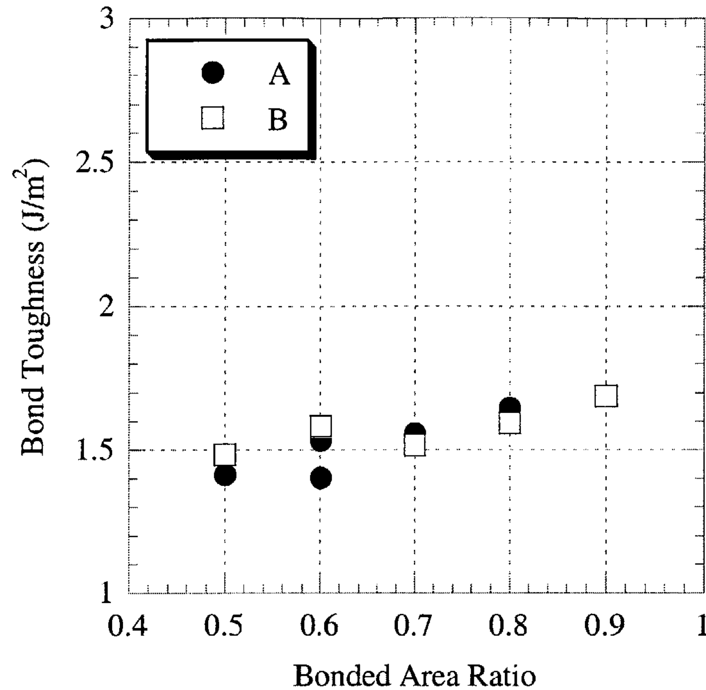

Figure 2-5: Effect of bonded area ratio on toughness.

notch was a line, with a length equal to the width of the bonded areas. The bonded areas in the chevron notch specimens met the central notch at a point. The point was created by incorporating a triangular region at the end of the bonded areas with an included angle of 60°.

The premise of the chevron notch design was that the reduced bonded area at the notch should make it easier for a crack to initiate at the interface. Once the crack has initiated at the interface, it should continue to propagate along the interface if the bonded area is sufficiently low. The fact that the width of the bonded regions vary near the central notch means that delamination in this region will not occur at a constant load. However, once the crack has propagated past the triangular ends of the bonded regions, the specimen will delaminate at a constant load and a plateau will be observed in the load displacement curve. Based on this load, the critical strain energy release rate can be calculated. In the specimens used in this study, the distance from the central notch to the inner loading points was 10 mm and the maximum length

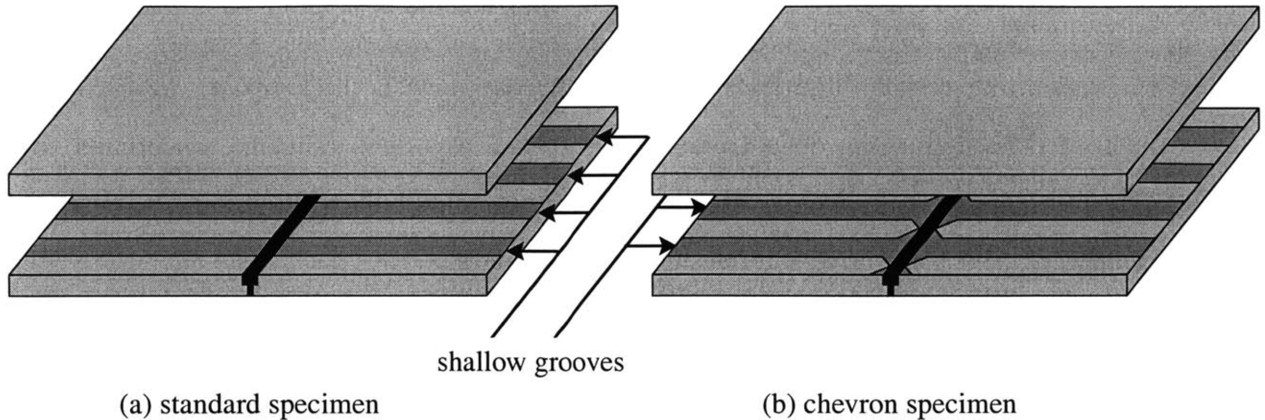

Figure 2-6: Standard and chevron notch specimen geometries.

of the triangular regions was 0.8 mm. Based on these dimensions, it is clear that a large plateau should be observed from which the critical load can be determined.

2.5 Specimen Fabrication

The fabrication process was a two mask process and required two lithography steps, two etches, two 'piranha' cleans, an RCA clean, and the final bonding step. The first mask was used to define the pattern for the shallow grooves, which reduced the bonded area at the interface. The mask layouts for the standard and chevron specimens are included in Appendix A. The pattern was designed so that nine specimens, each 8 mm wide, with varying area ratios from 0.1 to 0.9, were fabricated on a single 4" wafer. The etched shallow grooves resulted in bonded regions varying from 0.1 to 0.9 mm in width. The second mask, which is also included in Appendix A, was used to define a deep trench, which formed the central notch in either the standard or chevron specimens. The central notch was 0.6mm wide and ends short of the edges of the wafer in order to protect against possible wafer fracture. Alignment marks were included in both masks to permit precise positioning between the two etches.

All specimens were fabricated from single-side polished 4", n-type, (100) Czochralski grown, silicon wafers with an average thickness of 525 μm. The pattern for the shallow grooves was defined in a layer of OCG825 photoresist. The wafers were deep reactive ion etched for a brief period to form grooves 1-3 μm deep. The wafers were

subsequently cleaned using a standard 'piranha' clean (3:1 H_2SO_4:H_2O_2) to remove the remaining resist. The wafers were then coated with thick resist, AZ4620, and patterned to define the deep trench. The trench was deep reactive ion etched to a depth of 100 μm at an average etch rate of 2.5 μm/min. Following etching, a 'piranha' clean was used to remove the resist from the wafers.

To prepare for bonding, an etched silicon wafer and bare silicon wafer were cleaned using a standard RCA™ clean. In the RCA™ clean, organics are removed using a 5:1:1 H_2O:H_2O_2:NH_4OH solution. A thin silicon dioxide layer is then removed using a 50:1 H_2O:HF solution. An ionic clean in 6:1:1 H_2O:H_2O_2:HCl solution followed by distilled water rinse and spin dry are the final steps of the clean procedure. The RCA™ clean results in a surface that is hydrophilic and ready to be contacted. Immediately following the RCA clean, an etched wafer was aligned to a bare wafer and transferred to an Electronic Visions AB1-PV bonder. The chamber was purged with nitrogen and then evacuated to 5×10^{-2} mbar. After the desired chamber pressure had been achieved, the wafers were contacted and clamped with a specified pressure. A pressure of 4000 mbar applied over a period of 30 s is the baseline process. In this study, the magnitude and duration of the applied pressure were varied systematically between 150-2000 mbar and 60-1200 s respectively. Following contacting, the chamber was vented to atmosphere and the wafer pair was removed. The wafer pair, which is held together by weak surfaces forces following contacting, was inspected for large voids using IR imaging. A typical IR image of a bonded wafer pair is shown in Figure 2-7. To achieve full bond strength, the bonded pair was annealed in a nitrogen atmosphere. The effect of annealing time and temperature were the primary interest in this work, thus a considerable range was examined. A series of six bonded pairs were annealed for 24 hours at temperatures from 500-1000°C in increments of 100°C to examine the effect of annealing temperature. The effect of annealing time was investigated by fabricating seven bonded pairs at an anneal temperature of 600°C for anneal times from 48 to 336 hours in 48 hour increments.

Following bonding, the location of specimens were marked on the exterior of the bonded wafer pair using IR imaging. Following marking, one cut using a wet diamond

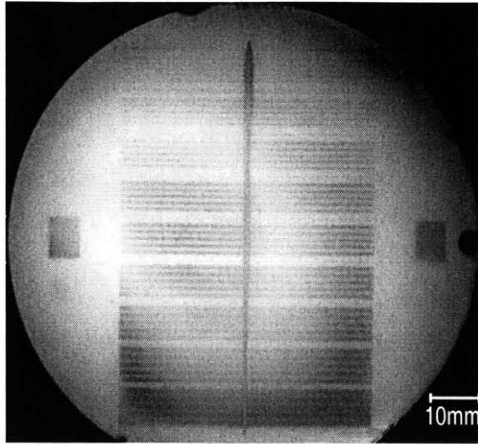

Figure 2-7: IR image of a bonded wafer pair.

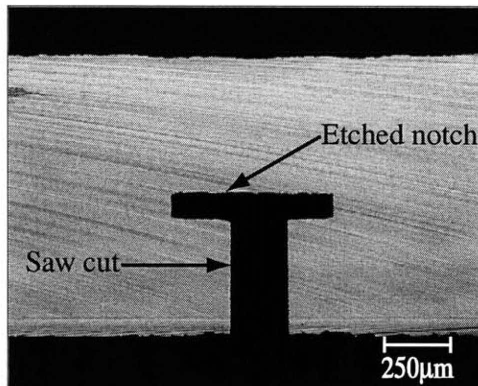

Figure 2-8: Micrograph of specimen showing interfacial notch.

wafer saw was made at each end of the wafer parallel to the specimens. These cuts allowed the location of the deep trench to be viewed directly and marked accurately. Marking the location of the deep trench using this procedure proved to be significantly more accurate than marking it using IR imaging. Mechanical testing specimens were then fabricated from the bonded wafer pairs with two sequences of cuts using a wet diamond wafer saw. First, the saw was used to cut through the lower wafer and intersect with the deep trench. This saw cut and the deep etched trench form the central notch as shown in Figure 2-8. Following the fabrication of the central notch, nine specimens were cut from each wafer by dicing into 8 mm wide strips. Finally, the diced specimens were removed from the mounting tape, which is required for the dicing saw, and cleaned thoroughly with an acetone rinse.

2.6 Experimental Procedure

2.6.1 Test Apparatus

Testing was carried out in a commercial servo-hydraulic test machine fitted with a four-point loading fixture. The four-point loading fixture is a commercial fixture and accepts specimens up to 8 mm wide of any thickness. The inner loading points are 20 mm apart and are centered between the outer rollers which are spaced 40 mm apart. The rollers are 4.8 mm diameter carbon steel pins and rest on half-moon shaped alumina supports. The half-moon supports allow the rollers to articulate around the longitudinal axis of the specimen. The test machine offers direct measurement of crosshead displacement and a 100 N load cell was used to ensure accurate load measurement in the range of interest. The load and crosshead displacement were monitored and recorded using a microcomputer with a data acquisition board and LabVIEW™ software. While not required, crack propagation was monitored using a Questar™ telemicroscope.

2.6.2 Alignment

Early tests revealed that the alignment of the standard four-point test fixture was quite poor. The presence of the misalignment was identified from force-displacement plots of tests and observations through a telemicroscope. The plots showed that delamination was not occurring at a constant load and crack opening observations revealed that the crack would consistently propagate first on one side of the fixture. This behavior is indicative of a jig that is misaligned such that one of the inner rollers contacts the specimen before the other inner roller. This results in three-point bending initially and a larger loading on one side of the specimen. This behavior was verified by instrumenting an 8 mm wide by 1 mm thick silicon beam with two piezoresistive strain gages. The strain gages were mounted on the bottom of the beam and positioned 20 mm apart on center. The beam was placed in the four-point fixture such that the gages were aligned with the inner loading points. While loading

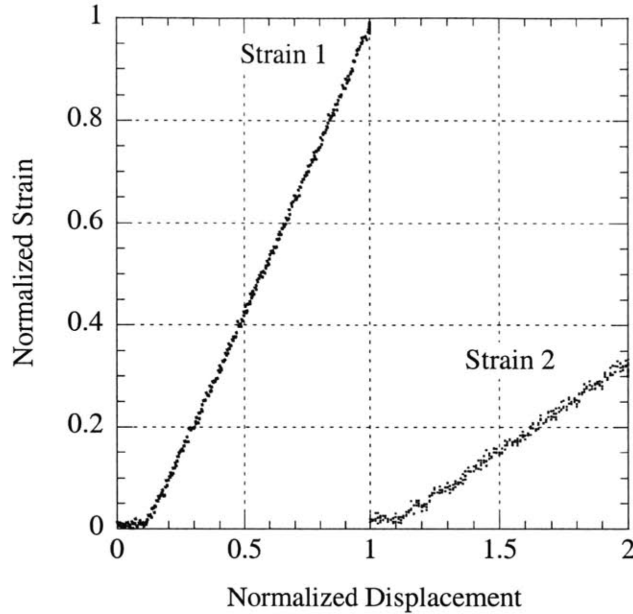

Figure 2-9: Strain-displacement for a misaligned specimen.

the specimen under displacement control, the strain was monitored on the two gages to observe the relative loading of the two sides of the specimen. By comparing the strain-crosshead displacement curves for the two strain gages, it can be determined whether or not the jig is properly aligned to provide four-point bending. Figure 2-9 shows the strain-displacement curves obtained from a specimen that was tested using the standard four-point test jig. Since this test is simply a comparison between the two strain gages, the strain and displacement values have been normalized. The strain 2 curve was shifted by 1.0 on the displacement axis to permit a clearer representation of the data. The important point to recognize from Figure 2-9 is that the slopes of the two curves are significantly different, and at equal displacements strain 2 is significantly lower than strain 1. This indicates that the roller located above strain gage 1 comes into contact with the specimen prior to the roller above strain gage 2. This type of misalignment is illustrated in Figure 2-10.

To correct for the misalignment, a custom fixture was designed and constructed. The fixture, which is illustrated schematically in Figure 2-11, consists of two aluminum plates pivoted on a center roller. Two springs on the ends of the plates provide a

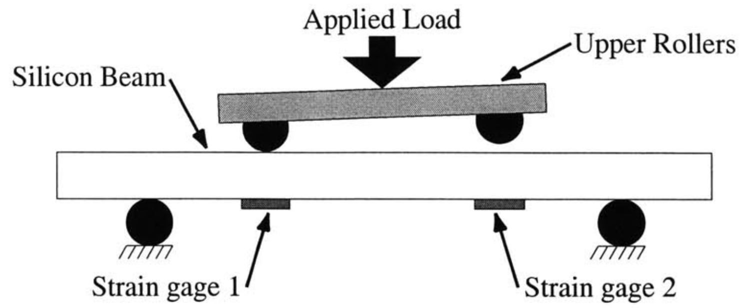

Figure 2-10: Schematic of misalignment.

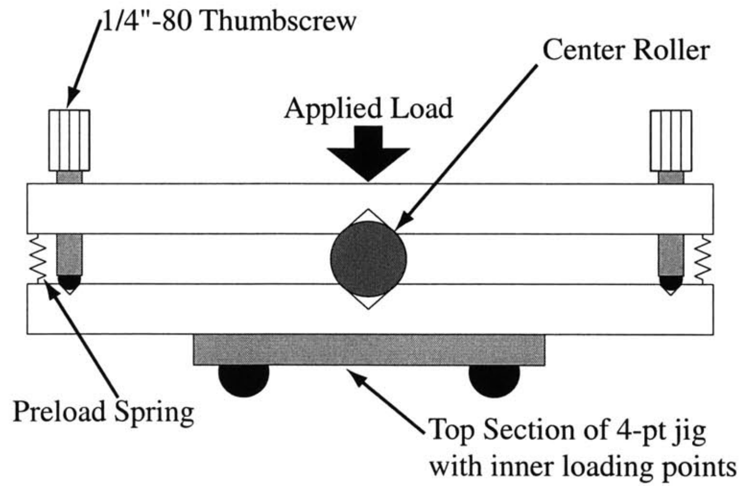

Figure 2-11: Schematic of alignment fixture.

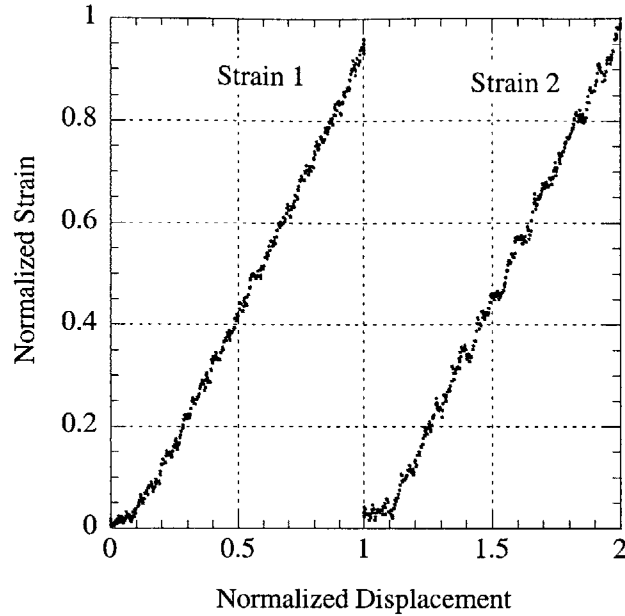

Figure 2-12: Strain-displacement for an aligned specimen.

preload, which keeps the plates firmly against the center roller. Two 1/4"-80 thumbscrews are mounted in the top plate and allow the relative angle between the two plates to be varied by approximately +/- 10° from the parallel position. Care must be taken when using the alignment fixture to avoid displacing the thumbscrews too far and lifting the plates off of the center roller. If the plates are separated from the center roller, the jig will be unstable. To be effective, the center line of the alignment jig must be aligned with the center line of the four-point-loading fixture.

Employing this alignment fixture and adjusting it appropriately resulted in a uniform loading of the specimen. Strain-displacement curves obtained using a strain-gaged beam are plotted in Figure 2-12. It is evident from the similar slopes of the two curves shown in Figure 2-12 that the misalignment was significantly reduced. While the alignment jig provides the potential to achieve good alignment, as seen in Figure 2-12, it does not guarantee it. The jig must be adjusted carefully to ensure that the specimen is uniformly loaded. Proper adjustment of the alignment jig was an iterative process, and involved loading a strain gaged beam specimen up to a specified displacement that corresponds to a range similar to that expected in actual

tests. While the beam had a static load applied, the thumbscrews were adjusted to balance the strains on the two sides. The specimen was then unloaded and reloaded to ensure the strain-displacement curves had similar slopes. Experience demonstrated that several loading and adjustment steps are required to achieve balanced loading on the two strain gages. Following alignment, load-displacement curves obtained on delamination specimens exhibited the load plateau that was expected.

2.6.3 Test Procedure

Specimens were placed in the four-point bending fixture such that the central notch of the specimen fell within the inner loading points. While exact alignment is not critical, since the moment between the inner rollers is constant, an attempt was made to align the central notch of the specimen with the center line of the fixture. Centering the specimen allows the maximum amount of crack growth at a constant load and hence a larger plateau in the force-displacement curve. Friction between the rollers and specimen, which can have a significant effect on the measured G_c value [30], was minimized through the use of a dry graphite lubricant. Specimens were loaded under displacement control at a constant rate of 0.15 mm/min. Crack propagation was permitted to continue until the crack reached the inner loading points, at which point the specimen was unloaded. The actual dimensions of the specimen, including the overall width, the interface grooves, and the thickness of the layers, were measured. The width and thickness were measured using a digital micrometer and the groove dimensions were measured using an optical microscope with a measurement feature. These dimensions and the critical load from the test were used to calculate G_c values using equations 2.9 and 2.11.

2.7 Test Results

A force-displacement plot from a typical test is shown in Figure 2-13. The specimen loads elastically until a critical load is reached. This elastic loading region is observed in Figure 2-13. The fact that the loading is not entirely smooth was a result of

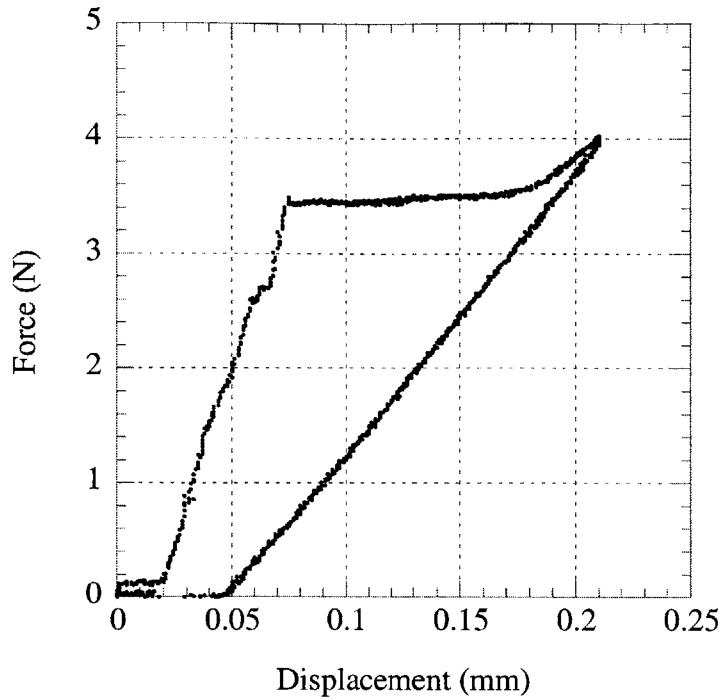

Figure 2-13: Load-displacement plot for a typical test.

the specimen and rollers seating themselves. At a critical load of approximately 3.5 N, delamination began and proceeded at a constant load. After propagating at a constant load, the load began to increase, which indicates the crack had reached the outer loading points. Following this, the specimen was unloaded. The specimen unloaded in an elastic manner and was more compliant because of the crack growth at the interface. The unloading path does not pass through the origin of the plot because the crack fails to close completely due to particulates that accumulate at the interface after delamination.

2.7.1 Effectiveness of Specimen

Delamination and steady-state crack growth, as observed in Figure 2-13, was routinely obtained for low toughness bonds ($G_c < 2.5$ J/m^2). While the test specimen allowed low toughness bonds to be characterized, it proved ineffective in quantifying the toughness of well bonded wafers. Rather than delaminating along the interface, the

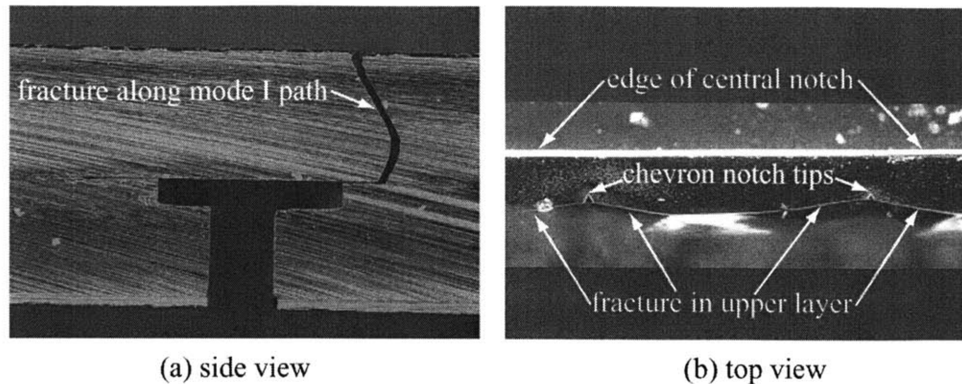

(a) side view (b) top view

Figure 2-14: Chevron-notch specimen failure.

crack would either fail to initiate or would propagate a short distance along the interface and quickly deflect into the unnotched silicon layer. When either of these situations occurred, exact bond toughness values, could not be obtained, but a lower limit could be established. The reduction of the bonded area at the interface and the chevron notch had a limited effect in mitigating these difficulties.

The use of shallow grooves to reduce the effective toughness proved unsuccessful in preventing crack deflection. Tests of specimens with low toughness bonds verified equation 2.11 and demonstrated that the shallow grooves reduce the effective 'global' toughness of the interface. However, this proved to be inadequate in preventing crack deflection in well bonded specimens. It is believed that this occurred because of the scale of the groove pattern and that while the 'global' interface toughness is reduced, the 'local' toughness in the bonded regions is the quantity that actually controls crack deflection. A crack that is propagating along one of the bonded regions, which is hundreds of microns wide, deflects from the interface to follow a mode I path and subsequently leads to fracture of the upper silicon beam

The chevron notch geometry, which was implemented to encourage crack initiation at interface, did not notably change the delamination success rate in well-bonded specimens. In specimens annealed at temperatures greater than 800°C, failure through the upper silicon layer was common. A specimen that fractured through the upper silicon layer is shown in Figure 2-14. The path of the crack shown in Figure 2-14(a) is typical of the majority of failures observed. Figure 2-14(b) demonstrates that in

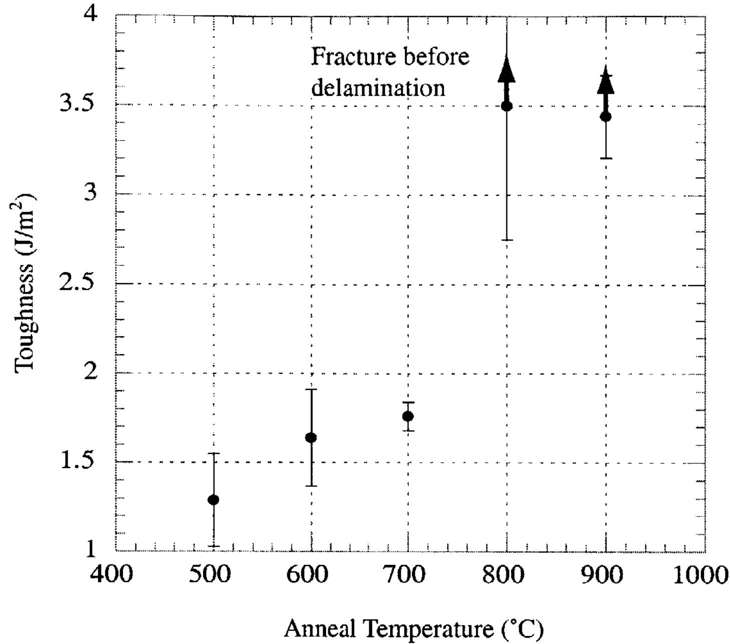

Figure 2-15: Bond toughness as a function of anneal temperature. Anneal time, contacting pressure, and contacting time held constant at 24 hours, 4000 mbar and 30 s, respectively.

well-bonded specimens, the crack often fails to propagate a significant distance along the interface. As illustrated from these micrographs, the chevron notch geometry, did not offer a notable improvement over the original specimen design.

2.7.2 Effect of Process Parameters on Bond Quality

Despite the limitations of the specimen, mixed-mode toughness values were obtained for silicon fusion bonds under various processing conditions. The reported data is limited to low toughness bonds and includes data from specimens fabricated under various annealing temperatures and times, and contacting conditions. For each set of processing conditions, multiple specimens from a single wafer pair were tested. Thus, in the plots that follow each data point represents an average of the specimens tested, typically four to five specimens. The error bars indicate the standard deviation of the data set.

Figures 2-15 and 2-16 demonstrate the effect of annealing temperature and time, respectively. All the specimens in Figure 2-15 were annealed for 24 hours at the spec-

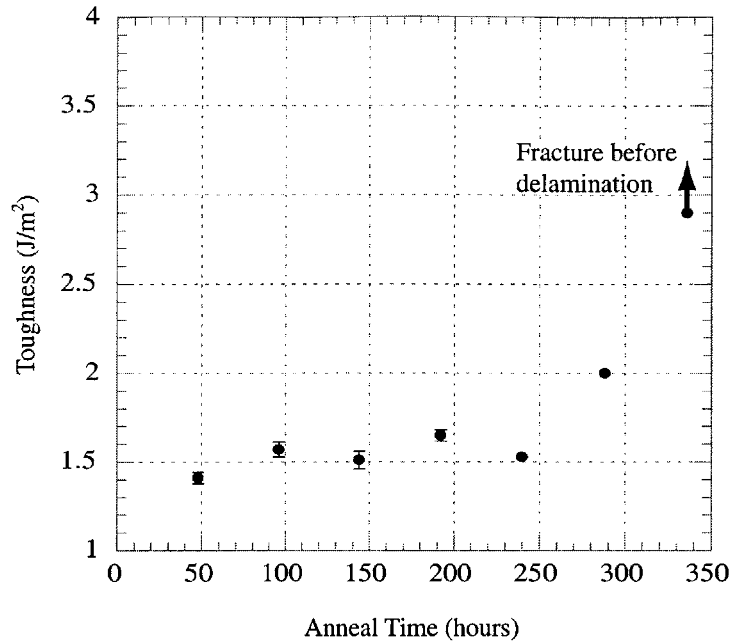

Figure 2-16: Bond toughness as a function of anneal time. Anneal temperature, contacting pressure, and contacting time held constant at 600 C, 4000 mbar and 30 s, respectively.

ified temperature. Figure 2-15 shows that bond toughness increases monotonically, but not linearly, with temperature. The specimens that were annealed at 800°C and 900°C failed to delaminate. As indicated on the plot, the measured toughness values for bonds at 800°C and 900°C only provide a lower limit on toughness. The lack of delamination indicates strong bonds, but specific values could not be obtained for G_c. The specimens used to obtain the data plotted in Figure 2-16 were annealed at 600°C for varying lengths of time. Delamination did not occur in the set of specimens annealed for 336 hours, thus, the data represents a lower limit on bond toughness at that point. Figure 2-16 suggests that annealing time has little effect on bond strength until some critical time is reached, at which point bond strength increases dramatically. The data in Figure 2-16 and the fact that specimens annealed at 336 hours did not delaminate suggests that bond strength can be increased after long anneal times. The trends observed with respect to annealing time and temperature are consistent with data for silicon fusion bonds reported elsewhere [20].

The effect of the parameters used during the initial contact of the wafers was

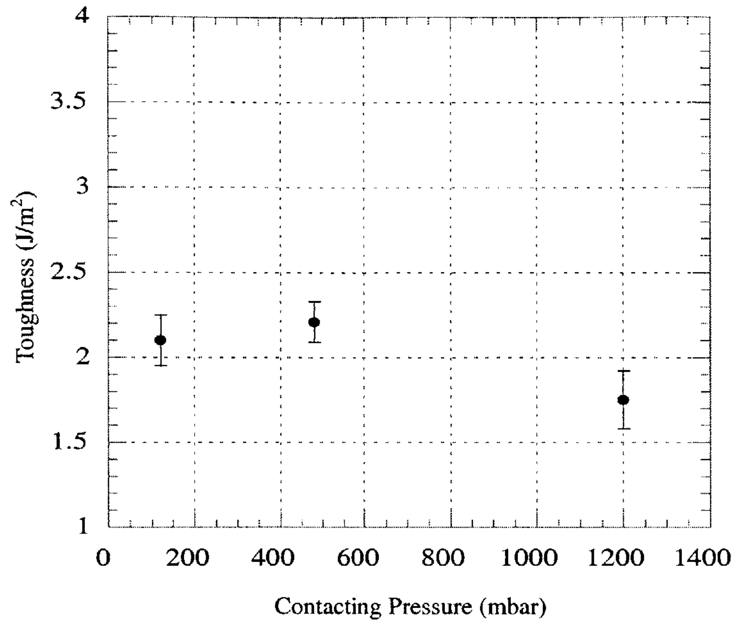

Figure 2-17: Bond toughness as a function of contacting pressure. Anneal temperature, anneal time, and contacting time held constant at 700 C, 24 hours and 30 s, respectively.

also examined in this study. To examine the effect of these, the anneal temperature and time were held constant at 700°C for 24 hours. The magnitude and time of the pressure applied during contacting were varied systematically. Figures 2-17 and 2-18 show the effect of the magnitude and time, respectively. Both parameters seem to have little effect on bond toughness. This is reasonable considering contacting is performed at room temperature and the lengths of time are relatively short.

2.8 Conclusion and Recommendations

A four-point bend delamination specimen has been employed to characterize the quality of silicon fusion bonds. A wafer-scale specimen fabrication process was demonstrated and test techniques developed. The study illustrated the need for proper alignment and provided a means to achieve it. The specimen was effective in characterizing low toughness bonds, however delamination and crack propagation along the interface could not be achieved in well-bonded specimens. The reduction of bonded area at the interface and the use of a chevron notch geometry proved ineffective in

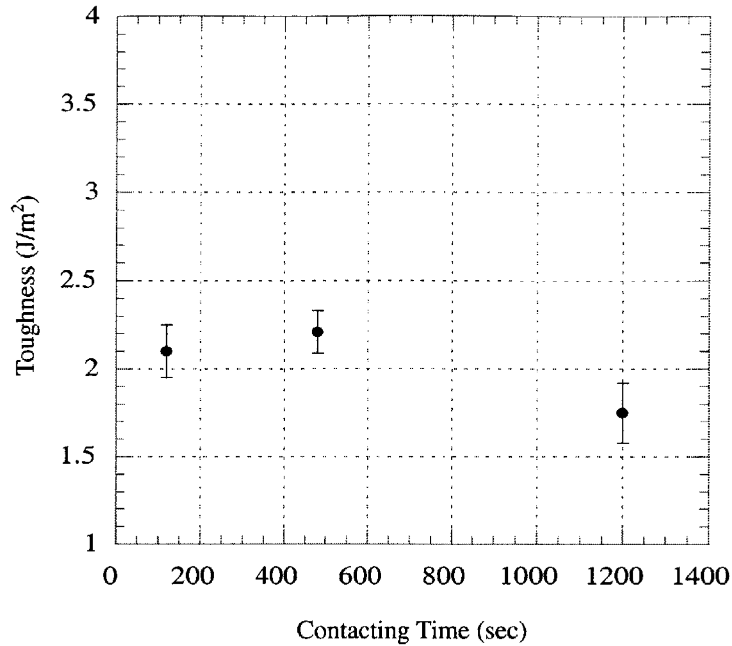

Figure 2-18: Bond toughness as a function of contacting time. Anneal temperature, anneal time, and contacting pressure held constant at 700 C, 24 hours and 4000 mbar, respectively.

encouraging crack initiation in high toughness interfaces. Tests of specimens with interface toughness values less than 2.5 J/m^2 were quite successful and demonstrated the expected behavior of stable crack propagation at a constant load. The increase in bond strength with annealing time and temperature that was observed is consistent with results reported elsewhere. The effect of contacting pressure and time were examined and found to have little effect on bond quality. The study clearly showed the applicability as well as the limitations of the four-point bend delamination specimen in characterizing silicon fusion bonds.

While the test technique has been developed and bonds have been characterized, further tests are required to completely map the process parameters of interest. The limitations of the specimen prevented bond toughness measurements on specimens fabricated under the full-range of process conditions. To examine the full range of process conditions, a different specimen geometry that permits delamination rather than fracture of specimens with well-bonded interfaces is required.

Chapter 3

Silicon-on-Insulator Membranes

3.1 Introduction

A common technique for producing thin single crystal silicon membranes of uniform thickness is to etch a cavity in the backside of a silicon-on-insulator (SOI) wafer. The thin oxide layer, which bonds the substrate to the device layer, acts as an etch stop. Thus, the membrane thickness is defined by the thickness of the device layer, which can range from less than 1 μm up to several hundred microns. The tethered pistons in MHT devices, which can be seen in Figure 1-1, are fabricated from SOI wafers using this basic approach. To produce the piston structure, a circular trench is deep reactive ion etched (DRIE) in the backside of the wafer, resulting in a central boss connected to the substrate via a thin tether. A typical tethered piston structure that has been cross-sectioned is shown in Figure 3-1. The central boss is the total thickness of the wafer and the tether thickness is defined by the device layer thickness. In typical MHT devices, the membrane is 5-15 μm thick, the boss is 405-415 μm thick, the boss has a diameter of 5-8 mm, and the trench is 150-225 μm wide.

The pistons are the primary moving mechanical components in MHT devices and allow the motion of the piezoelectric element to be transferred to the fluid medium. The tether serves as a seal, while permitting motion of the piston. The tethered pistons are loaded severely and two competing requirements are placed on the piston structure. The piston must allow for large displacements of the piezoelectric element,

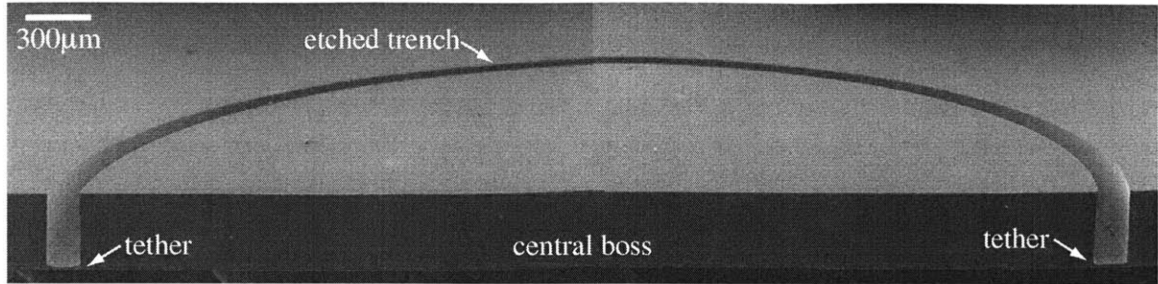

Figure 3-1: A SEM micrograph showing a typical MHT drive membrane.

but must also be stiff enough to withstand the high pressure loads from the fluid. This means that relatively stiff pistons must have the ability to withstand large deflections. Based on this, it is clear that high stresses cannot be avoided in the structure. Device modeling has indicated a clear link between device performance and the maximum allowable stress on the silicon structures [33]. Clearly, utilizing the full strength of the silicon membranes is required to achieve maximum device performance.

Single crystal silicon, while primarily used for microelectronics applications, has seen use as a mechanical material for close to three decades [34]. It is a high strength material and reported fracture strengths often exceed 1 GPa. The difficulty with employing this material for high stress applications is that it is has a low fracture toughness, and thus the tensile fracture strength is highly dependent on the presence of defects and the surface roughness of the structure. Furthermore, the surface roughness is highly dependent on fabrication process. Thus, while strength values are reported in the literature, the actual strength of silicon components must often be measured experimentally to ensure optimal and safe device design. The purpose of this work is to measure the strength of silicon membranes fabricated from SOI wafers in order to provide a realistic design strength for the development of MHT devices. This was accomplished by carrying out tests on specimens with a fabrication process and geometry similar to the piston structures found in MHT devices. Background material regarding the strength of silicon is followed by a summary of the specimens and the test method employed. The results of the mechanical tests are presented and recommendations regarding further process development and testing are made.

3.2 Background

While no published data exists on the strength of membranes fabricated from SOI wafers, several researchers have investigated the strength of single crystal silicon as a function of processing conditions. One of earliest investigations was completed by Hu in 1982 [35]. Hu loaded simply supported specimens at the center and measured fracture strengths for wafers with various surface treatments. For well polished (100) wafers, a mean fracture strength of 2.8 GPa with a standard deviation of 1.2 GPa was reported. The range of strengths observed in the study was large, with a low value of 0.3 GPa and a high value of 6.9 GPa. Wilson et al. loaded microcantilever silicon beams, which had been etched from (100) wafers using a KOH solution, to fracture [36]. A strong dependence of strength on surface roughness was observed. Mean fracture strengths between 1.0 and 3.6 GPa were reported. Chen et al. examined the strength of silicon using two different specimens, a biaxial flexure specimen and a geometry termed the radiused hub flexure specimen, in which a circular trench is etched and a load is applied on the resulting central hub [37], [38], [39]. The data was presented in Weibull form, which is typically used to present strength data of brittle materials. For specimens with various surface conditions, reference strengths from 1.2 to greater than 4 GPa were reported, with Weibull moduli ranging from 2.7 to 7.5. While the reference strengths indicate that high fracture strengths can be achieved, the low Weibull moduli indicate a large degree of scatter in the data. Of particular interest to the current study, are the results of radiused hub flexure specimens, which were fabricated by DRIE and had a geometry similar to the pistons in MHT devices. Using these specimens, Chen et al. demonstrated that the strength of DRIE structures could be improved significantly using either an isotropic wet etch or a SF_6 dry etch following the DRIE step.

The brittle nature of silicon, makes the fracture toughness an important quantity when considering the mechanical integrity of silicon structures. The fracture toughness determines the sensitivity of the fracture strength to flaws. Several studies report fracture toughness values for single crystal silicon. Early work, in which a

specimen with a flaw was loaded in four-point bending, measured fracture toughness as a function of crystal orientation. The highest fracture toughness, which was observed in the {100} orientation, was 0.95 $MN/m^{3/2}$. A lower fracture toughness of 0.82 $MN/m^{3/2}$ was observed for specimens with {111} orientation [40]. More recent work supports these findings and reports fracture toughness values of 0.83 $MN/m^{3/2}$ for specimens with a {111} orientation and 0.91 $MN/m^{3/2}$ for specimens with a {100} orientation [41].

Based on the reported strength values, it is clear that the strength of silicon is highly dependent on the fabrication route and geometry of the structure. The previous work provides a range of strength values, but is insufficient to use for design purposes. The reported fracture toughness values provide insight into the factors that control strength in silicon structures. The low fracture toughness suggests that the fracture strength is highly sensitive to flaws. The wide range of stress values and the low fracture toughness support the assertion that to obtain accurate design data, measurement of strength on specimens with a fabrication process and geometry similar to actual structures is required.

3.3 Experimental Method

The approach employed in the current study to measure the fracture strength of silicon membranes is illustrated in Figure 3-2. Specimens, which had a geometry similar to the drive pistons in MHT devices, were simply supported at the edges while a point load was applied at the center of the boss. The center loading point was actuated at a constant displacement rate until fracture of the membrane occurred. Based on the failure load and the measured geometry of the specimen, the fracture stress was determined using a finite element model. The details regarding the test specimen, apparatus, and procedure are presented below.

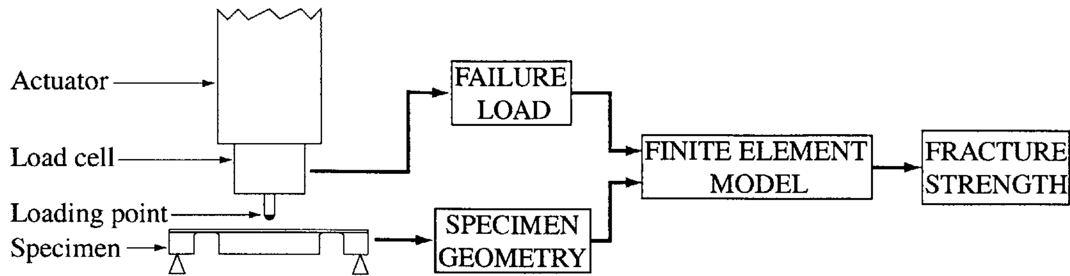

Figure 3-2: Fracture strength measurement approach.

3.3.1 Specimen Geometry and Loading

The test specimen was designed such that the geometry replicated the tethered drive pistons in the MHT device. This was done to ensure that the measured strength was an accurate representation of the strength expected in the device. The geometry must be similar because issues relating to etching, such as surface roughness, fillet radius control and etch rate, all depend on the geometry. The goal was to replicate faithfully the process used in device fabrication in order to not only quantify the strength, but to also gain a better understanding of the actual etched geometry and the difficulties in fabricating these structures. While these specimens allow the measurement of strength for these structures, the results may not be generally applicable due to the specific geometry.

The test specimen that was employed is shown in Figure 3-3. The specimen consisted of a central boss, 5.7 mm in diameter, connected via a 150 μm wide tether to a 10 $\times$ 10 mm die. The membrane thickness, which was defined by the thickness of the SOI device layer, varied in the current study from 5 to 18 μm. The tether was defined by etching a trench through the 400 μm thick substrate and controlling the etch appropriately to achieve a fillet radius at the bottom of the trench. The geometry is representative of that found in MHT devices, however, due to varying design requirements, the exact dimensions of the structures may vary. Pistons in current MHT devices have central bosses with diameters from 5 to 8 mm and tether widths from 150 to 225 μm.

In addition to matching the geometry, an effort was also made to achieve a stress distribution in the specimen similar to that in the device. The loading on the piston

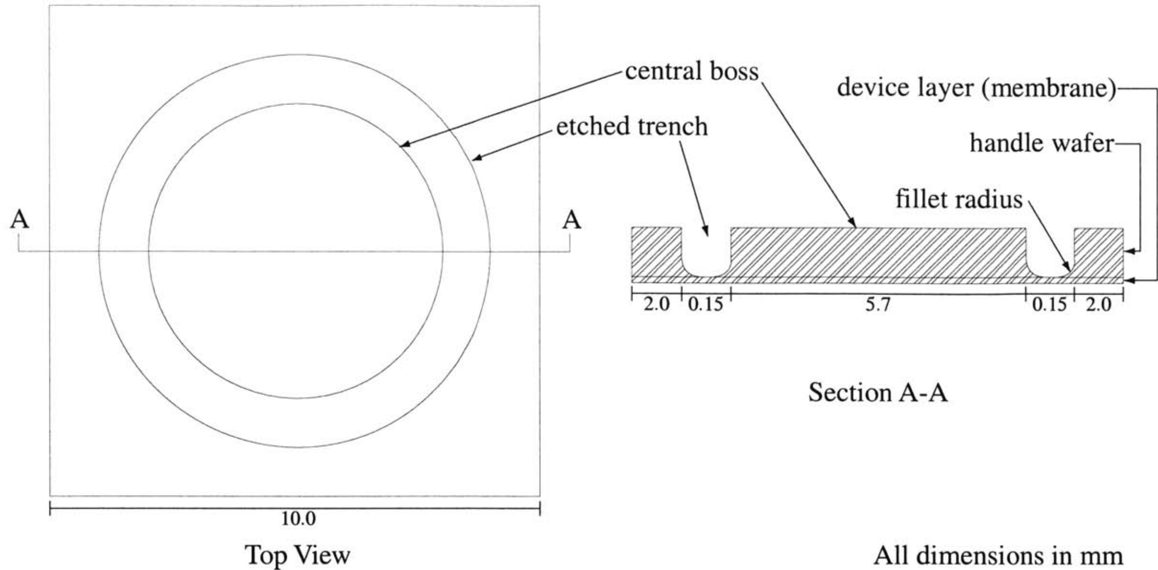

Figure 3-3: Schematic of test specimen for measurement of fracture strength.

structure during assembly and operation in MHT devices is quite complicated. Various combinations of pressure loads and displacements are applied to the tether during the device's lifetime. The highest tensile stresses are typically observed at the fillet radius at the base of the trench. Thus, a loading configuration that resulted in high tensile stresses at the fillet was chosen for this study. Two loading configurations, which are shown in Figure 3-4, that satisfy this requirement are a pressure load and a central point-load. The stress distribution does vary between the two cases, but, for the current geometry, the maximum tensile stress is found in the fillet for either loading scenario. The difficulty with the pressure load is that the specimen must be mounted securely in order to apply pressure from beneath. This mounting can induce residual stresses in the membrane and can be difficult to model accurately since the boundary conditions are not ideal. The point-load configuration, however, can be simply supported at the edges, which makes specimen mounting simpler and quicker. In addition, it is felt that the boundary conditions are easier to model accurately. Hence, in the current work, the specimen is simply supported at the edges and a load is applied at the center of the boss, as shown in Figure 3-4(b).

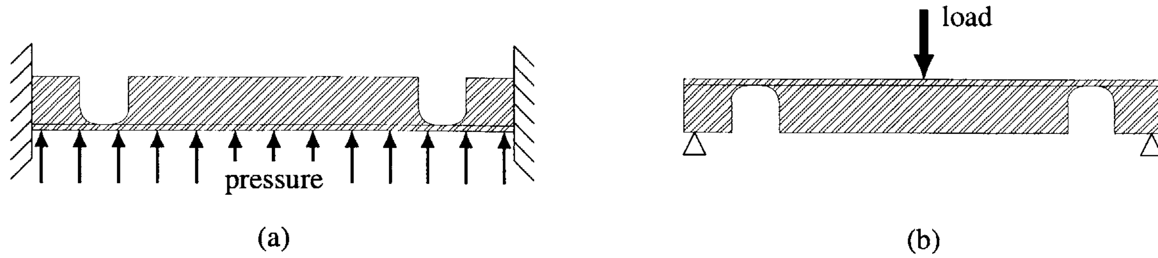

Figure 3-4: Potential silicon membrane loading configurations.

3.3.2 Specimen Fabrication

Specimens were fabricated from 4", (100), n-type double-side polished SOI wafers. The SOI wafers, which were purchased commercially, had been fabricated by bonding two (100) Czochralski grown silicon wafers together with a thermal oxide at the interface. Following bonding, the device layer was thinned using chemical-mechanical polishing. The specimens had features that required lithography and etching on both sides of the wafer. On the device layer, a shallow etch was used to create features that indicated the center of specimen, the specimen location on the wafer, and the edges of the specimen for dicing. A deep-etch from the backside was used to create the trenches that define the piston-like structure.

In order to achieve a fillet radius at the base of the trench, the deep etch must be controlled precisely. Control is difficult, and two different approaches to form and control the fillet radius were employed in the fabrication of specimens. The 'standard' approach, shown in Figure 3-5(a), is to etch a trench with straight sidewalls and carefully time the etch so that a fillet radius remains at the base of the trench. This approach is difficult because the etch must be controlled to within a few microns. Variations in etch uniformity across the wafer require that the wafer be inspected and that complete membranes be manually covered with photoresist, while etching is completed on others. An alternative approach employed is shown in Figure 3-5(b). A narrow trench is etched partially through the wafer, then a mask with a wider opening is used to complete the trench. This approach allows better control because the fillet does not recede as quickly during etching. While control is better, individual inspection and covering is still required.

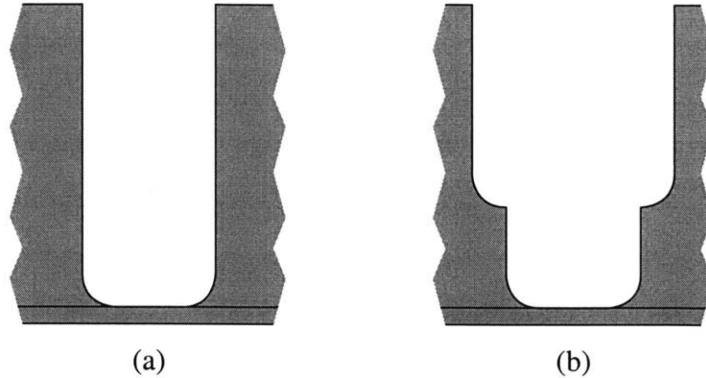

Figure 3-5: Different approaches for etching fillets, (a) 'standard', (b) 'alternate'.

To fabricate the standard test specimens, the device layer was coated with OCG825 thin photoresist. The resist was patterned to define alignment marks at the center of each specimen as well as marks to facilitate die-sawing. The wafer was etched briefly using DRIE to create features ≈4-6 μm deep. Following etching, the resist was stripped and the backside was coated with AZ4620 resist. The pattern to form the deep trench was defined in the resist. Alignment between the patterns on the two sides of the wafer was accomplished through the use of alignment features on the masks and a mask aligner with backside alignment capability. The trenches were etched at a rate of approximately 3 μm/min using DRIE. When the trench approached the oxide layer, the wafer was removed and the membranes were inspected. Membranes that had a suitable fillet radius were covered with resist using a swab and then baked to cure the resist. Following protection of complete membranes, the wafer was etched further to complete the remaining membranes. This process of inspection, protection and additional etching was repeated until all specimens had suitable fillet radii. Given the nature of this process, it is easy to see that it is time consuming and has the potential for large variations in quality. On a portion of the specimens fabricated, the oxide at the base of the trench was removed using a buffered oxide etch (BOE). Finally, specimens were mounted on a handle wafer using photoresist and separated into 10×10 mm dies using a diamond wafer saw. The mask layout used permitted 48 specimens to be fabricated per 4" wafer.

The 'alternate' specimen geometry was fabricated using the same process as the

standard specimens, with the exception of the backside etch. The trenches were fabricated using a nested mask to allow the stepped geometry to be formed. The nested mask consisted of an oxide mask, which defined the wider trench, and a photoresist mask to define the narrow section. Using the resist mask, a narrow trench was etched 100–200 μm deep. The resist was then stripped, and the oxide mask was used to etch the wider trench. The second etch, using the oxide mask, forms the step in the wall and completes the narrow trench in the center. The second etch is continued until the oxide is exposed. The fillet radii are then trimmed using the same procedure as employed on the standard specimens.

The basic DRIE process consists of sequential SF_6 dry etch and polymer passivation steps. The etch removes material and the passivation layer protects the sidewalls of the feature being etched. As discussed previously, Chen indicated the possibility to increase fracture strength of silicon by conducting a dry SF_6 etch without passivation at the end of a deep etch [38]. A portion of the specimens fabricated utilized this approach in an attempt to increase strength. This was accomplished by etching the majority of the depth using the standard DRIE process and then completing the final fillet radius trimming using a dry SF_6 etch. This process results in more mask undercutting and slightly wider trenches, since the SF_6 etches isotropically, however, surface finish is improved.

3.3.3 Test Apparatus

Typical failure loads for specimens employed in this study were between 1 and 15 N depending on the exact membrane thickness and fillet dimensions. In addition to the relatively low loads, the maximum deflection at failure for these specimens was typically less than 6 μm. Thus, to test mechanically such specimens, a test machine that permitted submicron actuation and had the ability to measure loads well under 1 N was required. Furthermore, the test machine had to allow the specimens to be mounted and provide a means to align the loading point to the center of the specimen. The test machine that was developed and constructed for the current study based on these requirements is illustrated schematically and pictured in Figure 3-6.

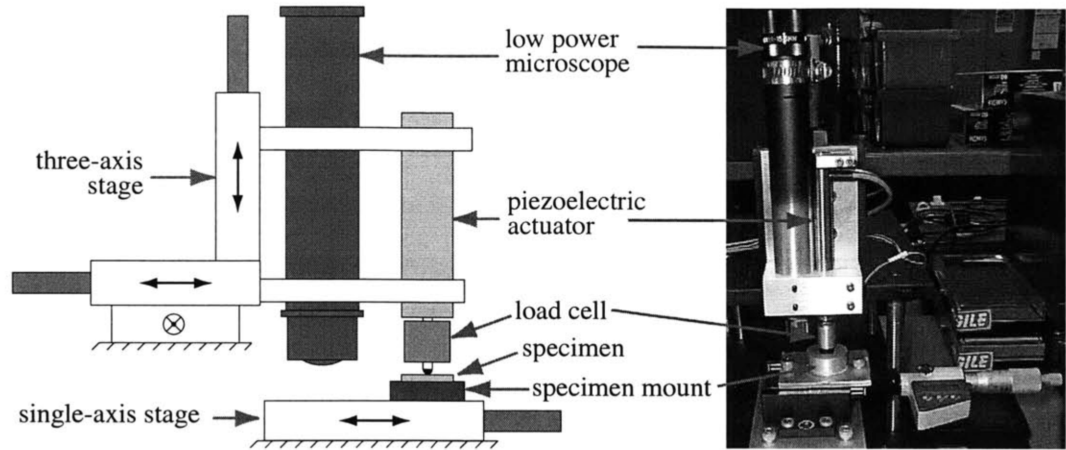

Figure 3-6: Silicon fracture test machine.

The layout of the test machine shown in Figure 3-6 is straightforward and consists of five basic components: an actuator, a load cell, a low-power microscope, a three-axis translation stage, and a precision single-axis translation stage. The basic theory of operation was that using the three-axis stage, the microscope, which contains a reticle with cross-hairs, was aligned to the etched feature at the center of the specimen. Following alignment, the single-axis stage was translated a fixed amount such that the loading point was aligned to the center of the specimen. The actuator was then used to displace the loading point and load the specimen. The load cell, which sits between the actuator and loading point, measured the force applied to the specimen.

The small displacements that were required, were achieved through the use of a commercially available piezoelectric stack actuator with a range of 60 μm. Loads were measured with a commercially available strain-gage based load cell with a full-scale range of 20 N. The load cell was calibrated in compression by applying a static load using weights. The results of multiple calibrations throughout the testing program demonstrated that the load cell sensitivity was repeatable to within +/- 5% of the original calibration. The single-axis stage used was a commercial optical stage fitted with a digital micrometer with a quoted accuracy of +/- 1 μm. The other essential components in the test setup included the specimen mount, loading point, and the data acquisition system. The specimen mount, which sits on the single axis translation stage, was an aluminium block with a machined groove to locate the specimen

and a through hole 6.4 mm in diameter to permit the membrane to deflect. The loading-point was a 1.5 mm steel ball that was mounted to the end of the load cell. The actuator was controlled and the load was recorded using a microcomputer and LabVIEW™ data acquisition software.

Extensive efforts were taken to ensure proper alignment and calibration of the test machine. As stated previously, the calibration of the load cell was checked periodically throughout the testing program. An additional source of error that was of concern was misalignment of the loading point with respect to the center of the specimen. While alignment marks are etched on the center of each specimen, the process of aligning to the marks using the reticle and then translating the stage to align the loading point is a potential source of error. To ensure that the loading-point position matched that of the reticle once translated, a series of tests were completed in which a soft wax was indented to check the alignment and positioning accuracy. The results of the tests demonstrated that the loading-point could be repeatedly aligned to within +/- 50 μm of the initial position of the reticle. The effect of this error on the stress state in the specimen was examined using a linear 3-D finite element model of a typical specimen. The model, which consisted of half of a specimen with a 3 mm outer diameter, 150 μm tether width, 400 μm thick boss and 10 μm thick membrane, was solved using the commercial finite element package ANSYS™. A copy of the batch file defining the model is included in Appendix B. A 5 μm fillet radius was assumed at the base of the trench and a 2 N point load was applied near the center of the boss. The position of the point load was shifted different distances from the center of the specimen to observe the effect of misalignment on the maximum stress in the structure at the fillet radius. Figure 3-7 shows the percent change in maximum stress as the 2 N point load is shifted from the center. It is seen that if the position error is less than 50 μm, the maximum stress increases by less than 4%. This result is quite reasonable considering the stiffness of the boss relative to the membrane and the relatively large diameter of the boss compared to the magnitude of the position error.

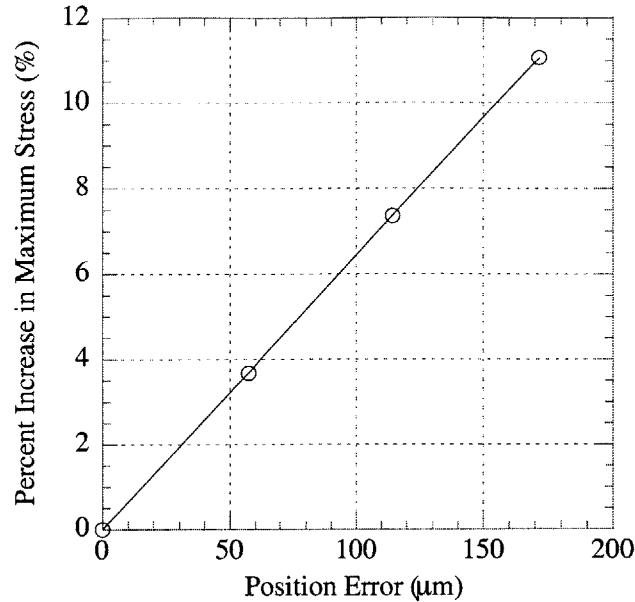

Figure 3-7: Effect of misalignment on maximum stress in a specimen.

3.3.4 Test Procedure

Following specimen fabrication and dicing, the specimens were separated from the handle wafer and cleaned in acetone. The trench width and fillet radius of the specimens were measured using an optical microscope with a calibrated digital measuring feature. The top width and fillet radii were measured in three locations around the circumference of the trench. The fillet radius was measured by viewing the bottom of the etched trench and measuring the width of the membrane between the fillets as seen in Figure 3-8(a). The fillet radius was then calculated by subtracting this length from the measured top width and dividing by two. This method is only valid when the sidewalls of the trench are straight, the fillets on both sides of the trench are equal size and the fillet geometry can be inferred from the length alone. Numerous specimens were cross-sectioned to verify that these conditions were true for the specimens in this work. The straight sidewalls and equal size fillets can be seen in Figure 3-8(b). The fillet shape appears to scale relatively well with length and the effect of slight variations in exact fillet geometry do not effect the calculated stress values significantly as discussed in Section 3.4. The features observed in Figure 3-8(b)

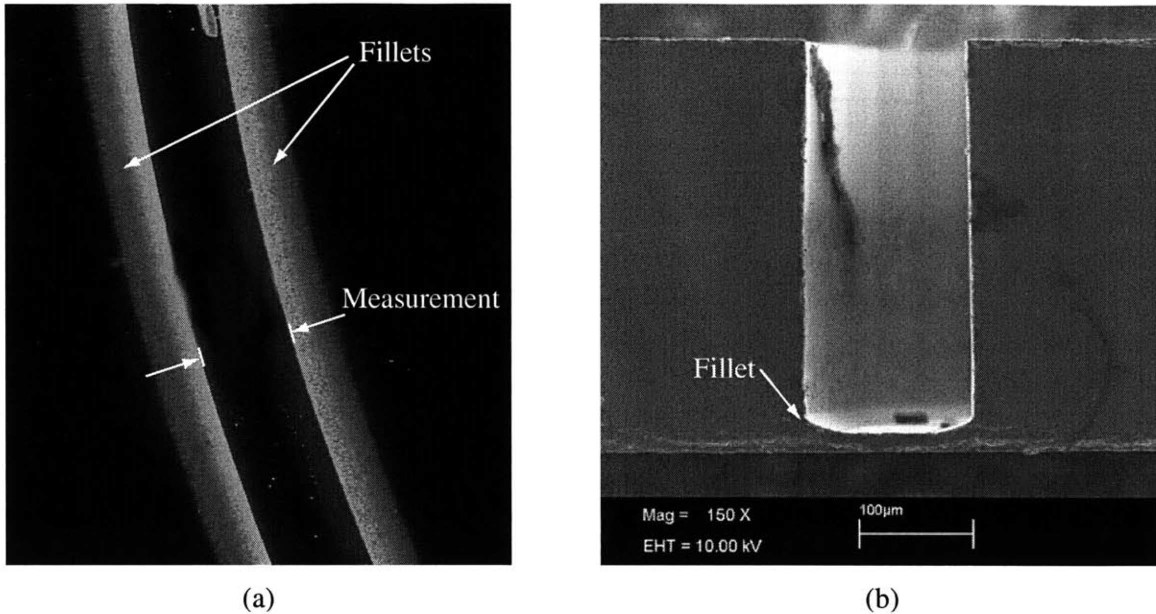

(a) (b)

Figure 3-8: Typical fillet radius, (a) viewed from the top, (b) cross-section view.

were consistent among the specimens cross-sectioned, thus it was concluded that it was reasonable to measure the fillet geometry using the method described. For the 'alternate' specimen geometry, a similar procedure was used, but, the width of the trench at the step was also measured to allow the fillet radius to be calculated.

In addition to the measurements with the optical microscope, several specimens from each wafer were cross-sectioned and the membrane thickness was measured using a scanning electron microscope (SEM). The calibration of the SEM was checked using a measurement standard with 1.9 and 10 μm features, immediately prior to measuring any specimens. It is assumed that the thickness of the membrane is uniform across the wafer, thus, measurements from 1 or 2 specimens were used to determine the thickness of all the specimens on a wafer.

Along with the measurements, the specimens were also inspected for defects in the membrane or fillet using an optical microscope. Defects in the fillet are common and specimens with large defects were not tested. Defects, such as the example shown in Figure 3-9, are caused by poor photoresist coverage during the inspection and protection stage of the fabrication process. This problem has recently been solved by using a thin photoresist and increasing the bake times during the individual fillet

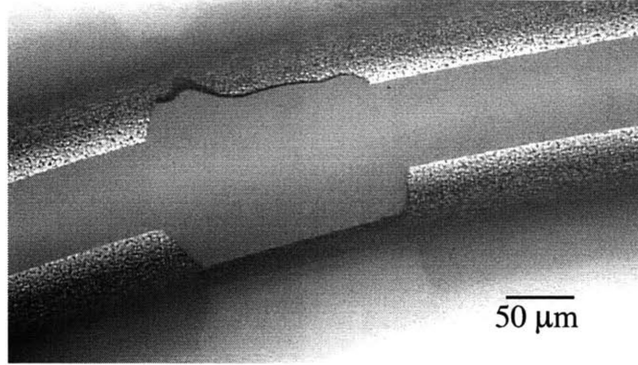

Figure 3-9: Typical defect in fillet radius.

protection process. Between defects such as these, membranes that were over or under-etched, and membranes that fractured during fabrication and handling, the typical specimen yield on a wafer was 30 to 50%.

Following measurement and inspection, the specimens were mounted in the test machine. The specimens were aligned and loaded at a constant displacement rate to fracture, as discussed in Section 3.3.3. The load was recorded as a function of time using LabVIEW™. The failure load was obtained from the recorded data and a failure stress was obtained from a simple finite element model using this load value and the measured geometry of the specimen. The finite element model is detailed in the following section.

3.4 Finite Element Modeling and Data Reduction

To extract the failure stress from the measured failure load and geometry, a finite element analysis of the specimen was used. A full three dimensional model was too computationally expensive to use for this stress analysis, thus a 2-D axisymmetric model was employed. The basic form of the model, including boundary conditions and loading is shown in Figure 3-10. The model was meshed with 8-node plane strain axisymmetric elements as seen in Figure 3-10. Single crystal silicon, which is an anisotropic material with diamond cubic symmetry, has stiffness coefficients C_{11}=1.657, C_{12}=0.639, and C_{44}=0.796 10^{11}Pa [42]. For the purposes of the axisym-

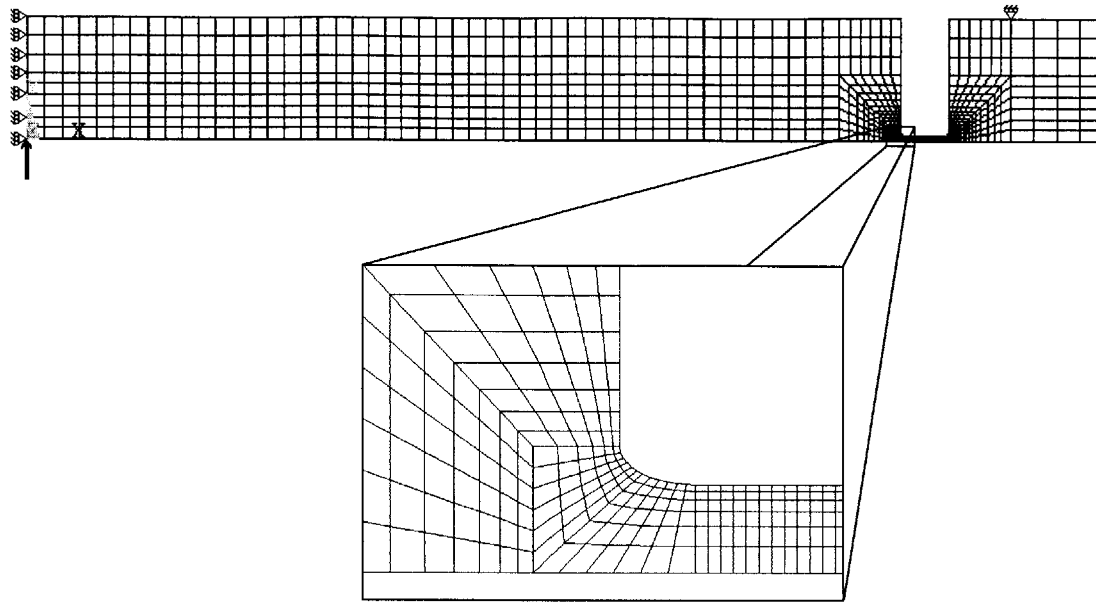

Figure 3-10: Finite element model of specimen.

metric finite element model, an isotropic equivalent Young's modulus of 165 GPa and a Poisson's ratio of 0.22 were assumed. The material is linear elastic up to the fracture point, thus material nonlinearities were not included. However, the deflections of the structure have the potential to be large relative to the membrane thickness, thus, nonlinearities due to large deflections and stress stiffening were included.

To extract the stress from a measured failure load, the geometry of the model was defined using the experimentally measured values. The measured trench width, membrane thickness, and fillet radius were used when determining the fracture stress for each specimen. The shape of the fillet radius was assumed to be a quarter-ellipse as seen in Figure 3-11. The b/a ratio, which defines the aspect ratio of the ellipse, was assumed to be 0.5 for all specimens. From the specimen cross-sections examined, it was seen that the b/a ratio was typically near 0.5, but occasionally was greater. A b/a ratio greater than 1.0 was never observed. The sensitivity of the maximum stress to the b/a ratio of the fillet was examined for a typical specimen with a 6 mm outer diameter, 5.7 mm inner diameter, 12 μm thick membrane, and a 6 N load applied at the center. The maximum stress as a function of fillet radius length, a, for b/a ratios from 0.5 to 1.0 is plotted in Figure 3-12. It is seen that the effect of the exact fillet

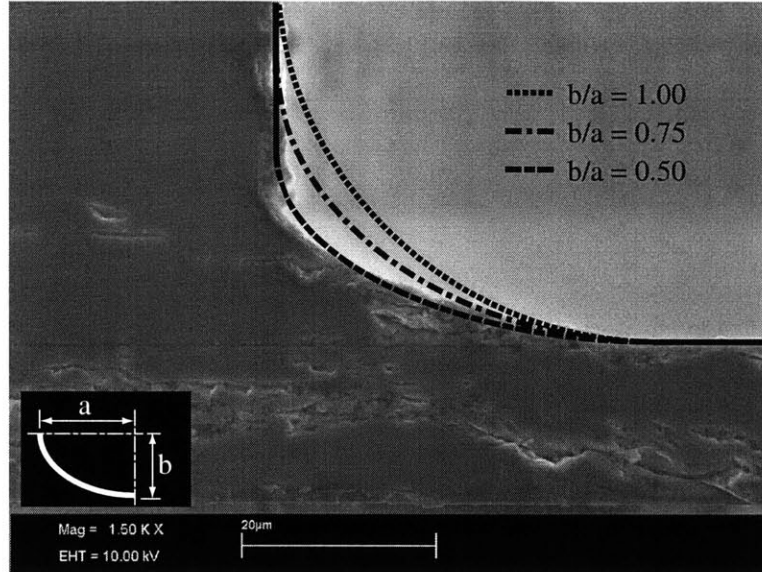

Figure 3-11: Typical shape of etched fillet radius.

radius shape on the maximum stress in the structure is small. This suggests that it is reasonable to assume $b/a = 0.5$ for all specimens and to infer the fillet geometry from the measured fillet length alone.

This finite element model, for which the batch file is included in Appendix B, was used to determine the fractures strength of all specimens tested. The fracture strength was taken as the maximum tensile stress (the first principal stress), which was located near the base of the fillet. Since silicon is a brittle material, failure does not simply depend on the maximum stress, but rather depends on the probability of a critically sized flaw being located and oriented relative to a tensile stress. Thus, strength data for brittle materials is usually represented using Weibull statistics, where the probability of failure depends on the stress distribution over a volume or surface area. Chen et al. used Weibull statistics to represent strength data of DRIE silicon and found the data only fit the Weibull distribution moderately well [38]. In the current study, significant scatter was present in the data and it did not appear to fit a Weibull distribution well. Thus, the data is presented in terms of maximum stress in the structure at failure. This approach is reasonable since the area and stress distribution of the specimen and the structures in MHT devices are quite similar. While this data may not necessarily be used to design a broad range of structures, it

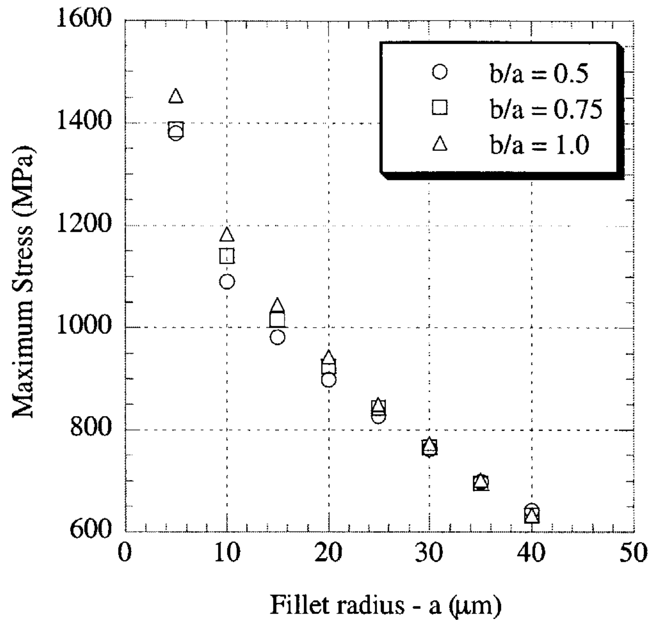

Figure 3-12: Effect of b/a ratio on maximum stress.

should provide moderately good estimates for the design of MHT devices.

3.5 Results

Through the course of this study, 7 wafers were fabricated and tested, yielding 129 specimens. The nominal thickness of the device layer, manufacturer of the wafer, and details with regard to the process, such as the use of a dry SF_6 etch or the removal of oxide are listed in Table 3.1. The wafers with 5 μm thick device layers were purchased from BCO Technologies[1], while the wafers with thicker device layers, 12.5 and 18 μm, were donated to the MIT Microsystems Technology Laboratory several years ago by Motorola. The specimens listed in Table 3.1 were fabricated in two batches. The first batch, which included wafers A and B, were fabricated using the standard process outlined in Section 3.3.2. The dry SF_6 etch was not used and the oxide at the base of the trenches was not removed. The second batch, which included wafers C through G, were fabricated with either the standard or alternate fabrication process discussed

[1]BCO Technologies, 5 Hannahstown Hill, Belfast, BT17 OLT United Kingdom

Table 3.1: Process conditions of fabricated wafers.

Wafer	Thickness	Manufacturer	Process	SF_6 dry etch?	Oxide removed?
A	5 μm	BCO	standard	no	no
B	18 μm	Motorola	standard	no	no
C	18 μm	Motorola	standard	yes	yes
D	18 μm	Motorola	standard	yes	yes
E	5 μm	BCO	standard	yes	yes
F	12.5 μm	Motorola	alternate	yes	yes
G	18 μm	Motorola	alternate	yes	yes

in Section 3.3.2. The fillet radius trimming was completed using the dry SF_6 etch and the oxide at the base of the etched trenches was removed. The oxide was removed at the base of the trenches because process development for the MHT device revealed that this oxide would have to be removed when fabricating the actual device.

All wafers were measured and tested according to the procedures outlined above. The fracture strength mean and coefficient of variation ($C.V. = \frac{Std.Dev}{Mean}$) for each wafer is listed in Table 3.2. In addition, the number of specimens tested from each wafer is provided. From the values listed, it is seen that the mean fracture strengths vary considerably between the BCO and Motorola wafers. One also notices that the coefficient of variation among specimens from a single wafer is quite large, typically near 0.25. This large coefficient of variation, which indicates considerable scatter in the data, is not entirely surprising given the fact that silicon is a brittle material. An additional factor, which may contribute to the scatter in the data, is the fact that the size of the fillet radius often varied by as much 50% around the circumference of the membrane. For the purpose of calculating fracture stress, an average fillet width was used, which yields a more conservative estimate of strength than if the minimum fillet dimension is used.

While the data in Table 3.2 summarizes the data from all the wafers, it is useful to group specimens with the same manufacturer and similar fabrication processes. The strength data presented in Table 3.2 was consolidated into four groups:

I. This group includes all the specimens from wafer A. The starting SOI wafer was from BCO, the SF_6 dry etch was not used, and the oxide was

Table 3.2: Fracture strength values of tested wafers.

Wafer	Measured Thickness	Mean (GPa)	C.V.	Number of Specimens
A	5.3 μm	1.67	0.27	10
B	17.5 μm	0.77	0.22	12
C	17.1 μm	0.54	0.26	26
D	17.4 μm	0.47	0.24	25
E	4.6 μm	1.30	0.37	19
F	13.1 μm	0.46	0.19	24
G	17.8 μm	0.40	0.29	13

Table 3.3: Consolidated fracture strength values.

Group	Mean (GPa)	C.V.	Number of Specimens
I	1.67	0.27	10
II	0.77	0.22	12
III	1.30	0.37	19
IV	0.48	0.26	88

not removed. The distribution of strength for this set is shown in Figure 3-13(a).

II. This group includes all the specimens from wafer B. The starting SOI wafer was from Motorola, the SF_6 dry etch was not used, and the oxide was not removed. The distribution of strength values for this set is shown in Figure 3-13(b).

III. This group includes all the specimens from wafer E. The starting SOI wafer was from BCO, the SF_6 dry etch was used, and the oxide was removed. The distribution of strength values for this set is shown in Figure 3-14(a).

IV. This group includes all the specimens from wafers C,D,F, and G. This set includes wafers fabricated using the 'standard' and 'alternate' trench geometries. The starting SOI wafers were from Motorola , the SF_6 dry etch was used, and the oxide was removed. The distribution of strength values for this set is shown in Figure 3-14(b).

The fracture strength mean and coefficient of variation for each group listed above are summarized in Table 3.3.

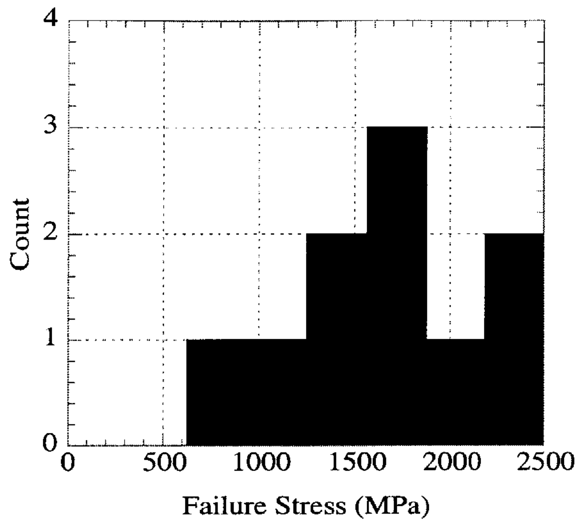

(a) BCO wafer.

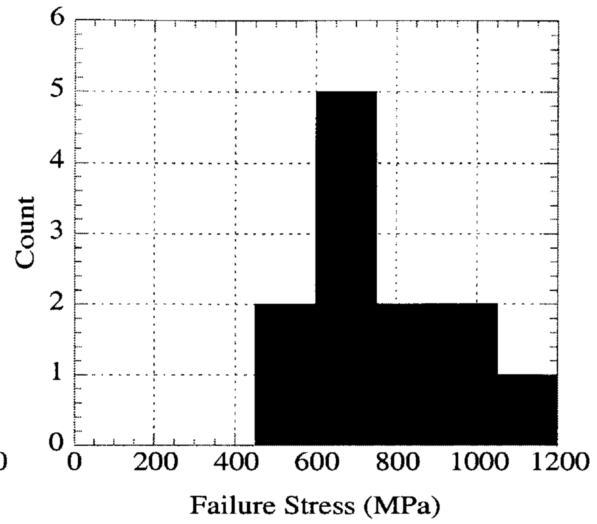

(b) Motorola wafer.

Figure 3-13: Strength results for specimens with oxide.

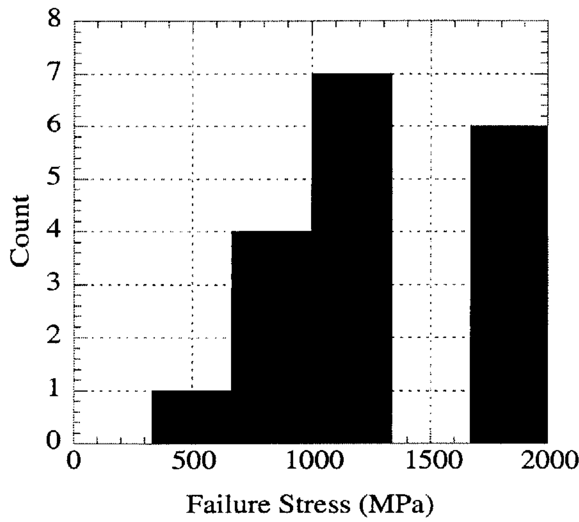

(a) BCO wafer.

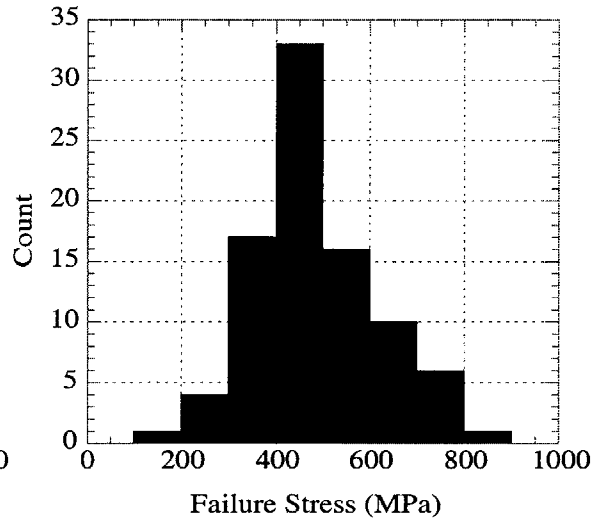

(b) Motorola wafers.

Figure 3-14: Strength results for specimens without oxide.

Based on the mean fracture strengths of the four groups discussed above, two clear trends can be identified. The first is that removal of the oxide at the base of the trench reduces fracture strength. The data shows a clear decrease of approximately 0.3-0.4 GPa in the strength of specimens when the oxide is removed. While this is a concern, it is a reasonable result. The oxide, which most likely contains a compressive residual stress, maintains a compressive stress on the surface of the structure. The compressive stress on the surface reduces the effective tensile stress on flaws and thus allows the structure to carry a higher load. The other trend, which is clear from the data, is that the BCO wafers are significantly stronger than the Motorola wafers. While one could argue that this may be due to the size effect, since the BCO specimens had thinner membranes than the Motorola specimens, it is unlikely this is the cause, since strength controlling defects in single crystal silicon are usually on the surface. While the volume of these specimens is different, the surface area and stress distribution is nearly the same. Thus, one would expect the two thicknesses to have similar failure probabilities. A more likely explanation is that there is a difference in the quality of the SOI wafers themselves. While both the Motorola and BCO wafers were manufactured with the same basic process, slight differences in the individual vendor's process may effect the strength. In addition, SOI fabrication is still a developing field and the Motorola wafers were fabricated several years before the BCO wafers, thus it is likely process improvements have been made since the Motorola wafers were fabricated.

An unfortunate artifact of how the specimens were fabricated is that all the specimens which had the oxide removed, also had the SF_6 dry etch. Since the oxide effects the strength, the effect of the SF_6 etch could not be observed in the data. While it is possible that the SF_6 etch could actually reduce the strength and be responsible for the decrease in strength attributed to the removal of the oxide, it is unlikely. SEM observations of the etched trench clearly show that specimens trimmed with the SF_6 have smoother etched surfaces. The smoother surfaces should result in higher strength, not lower strength as was observed. Thus, it is believed that the conclusion, that the removal of oxide reduces the strength, is a valid one.

While there are clear trends observed, the degree of scatter present is a concern. The scatter is present despite attempts to inspect specimens for defects prior to testing. The reason that this inspection process does not result in a tight strength distribution is because of the scale of the defects detected in the inspection process. During the inspection, defects with sizes on the order of 10-100 microns were observed. The difficulty arises from the fact that the defects that control strength are several orders of magnitude smaller than this. Using an average fracture toughness of silicon of K_{IC}=0.89 MN/m$^{3/2}$ and assuming failure occurs at a stress, σ_f, the critical flaw size that results in failure is,

$$a_{crit} \geq \frac{1}{\pi}\left(\frac{K_{IC}}{\sigma_f}\right)^2 . \tag{3.1}$$

Based on this, it easily seen that to achieve a fracture stress of 0.5 GPa, flaws must be less than 1.0 μm in size. Furthermore, to achieve a strength of 1 GPa, the maximum flaw size must be less than 0.25 μm. These flaws are well below the resolution of the inspection process used, and it would be difficult to inspect the entire structure, which is on the order of millimeters, for flaws less than 1 μm in dimension. Thus, the scatter in the data is not unreasonable. A degree of scatter is to be expected in strength data of brittle materials and that is why failure probabilities rather than strengths are often defined. Unfortunately, the data in the current study did not fit the typical Weibull distribution well and thus, strengths are reported rather than failure probabilities. The most likely cause of the poor fit is that there are several types of defects that control the strength.

3.6 Conclusions

In this study, the fracture strength of tethered piston structures fabricated from SOI wafers has been measured. The results indicate a strong dependence of strength on the SOI manufacturer as well as the processing route. It was observed that of the SOI wafers currently used in the fabrication of MHT devices, the strength of the BCO

wafers was significantly higher than that of the Motorola wafers. While no qualitative difference between the wafers could be observed, the strength tests clearly indicate a difference in quality. In addition, it was also observed that removal of the oxide at the base of the etched trench appears to reduce the fracture strength of the membrane structures. There was a large degree of scatter in the data and coefficient of variations of 0.25 were common. The strength values measured for these DRIE SOI structures was well below strengths reported elsewhere for similar DRIE structures fabricated from bulk silicon wafers [38]. The cause of this difference in strength between SOI wafers and bulk silicon wafers is not clear.

The study clearly indicated the need to develop a better fabrication process for membranes. Controlling the size of the fillet is difficult and variations in geometry are believed to be partly responsible for the scatter in the data. A better process is essential for improving yield and reducing manufacturing time. Based on the strength data, it clear that SOI wafers from different sources should be tested to verify the strength prior to integration in a device. Finally, it would be highly desirable to obtain additional strength data and to fit the data to a suitable statistical distribution. This would allow probabilistic design techniques to be used to ensure the reliability of MHT devices.

Chapter 4

Gold-Tin Bonding

4.1 Introduction

The integration of bulk piezoelectric material is a key factor in the design of micro-hydraulic transducers that allows high power density devices to be achieved. The bulk piezoelectric material, which may be a polycrystalline material such as PZT-5H (lead zirconate titanate) or a single crystal material such as PMN-PT (lead magnesium niobate-lead titanate) or PZN-PT (lead zinc niobate-lead titanate), allows significantly more actuation capability than thin-film piezoelectric materials that are typically found in microscale devices. In order to use the full potential of bulk piezoelectric materials, a reliable means of bonding the material to micromachined silicon structures is required. The bond must provide a mechanical and electrical connection, allow adequate dimensional control, and be compatible with the device fabrication process.

The focus of the current work is the development of the bonding process and preliminary mechanical characterization of bond strength. In this chapter, the requirements of the bond and the selection of the gold-tin solder bond are detailed. Previous work pertaining to gold-tin solder is briefly reviewed to establish a basic process and typical bond strength values. The process that has been developed to produce void-free bonds is described and the critical factors necessary to achieve robust bonds are identified. Results of tensile tests that were conducted to verify the

mechanical integrity of the bond and demonstrate potential weaknesses are presented. Recommendations regarding further process development and characterization are given.

4.2 Bond Selection

4.2.1 Bond Requirements

The primary function of the bond is to provide a mechanical connection between the piezoelectric element and the silicon structure. While efforts are made to keep the bond in compression during device operation, scenarios exist where a tensile load may be applied to the bond. In addition, the bond is subjected to cyclic shear strains from the lateral expansion of the piezoelectric element. Large numbers of cycles are expected to accumulate quickly, given that typical drive frequencies are between 10 and 30 kHz. These factors all contribute to a general requirement that the bond be mechanically robust. Equally important, the bond must provide an electrical connection between the silicon electrode and the piezoelectric element. While actuation could be achieved with a dielectric layer between the piezoelectric element and the silicon, the layer would act as a capacitor and would result in a voltage drop across the bond, thus requiring higher drive voltages. For a typical piezoelectric element (dielectric constant, $\kappa \approx 5000$) of height 1 mm bonded with a 1 μm thick bond of epoxy or glass ($\kappa \approx 5$) on both ends, the drive voltage required would be approximately three times higher than if the bond was conductive. An increase of drive voltage by a factor of three is a serious issue, since typical design voltages are near 1000 V. Finally, the bonding technique must also be compatible with the materials and fabrication processes of the device. Bonding mediums that have low maximum temperatures are not feasible because the final anodic bond, which requires a processing temperature of 300°C, must be completed coincident with or following the piezoelectric bonding step. Similarly, bonds which require high temperatures are limited by the softening point of the Pyrex glass, which is near 800°C, and the upper processing limit of

the piezoelectric material. It should be noted that at temperatures above 100°C the piezoelectric material de-poles, but it can easily be re-poled following bonding. These requirements dictate the selection of a suitable bonding technique.

4.2.2 Bonding Techniques

Bonding of dissimilar materials to construct mechanical structures on the microscale is an area of limited research. However, the area of packaging microdevices and die-attach techniques is a rich subject and is closely related to the task at hand. Packaging individual devices usually involves bonding dissimilar materials (one of them often silicon and the other often a ceramic) with relatively small areas, typically 4-100 mm^2. The piezoelectric elements in MHT devices must be bonded to silicon and have bonding areas approximately 1-3 mm^2. Thus, many of the techniques that were considered for the current application were based on die-attach and packaging techniques. Among the methods that were considered are solder bonding or brazing, organic adhesives, and glass bonding mediums.

Organic adhesives, such as polyimides and epoxies can be filled with a metal powder to provide electrical conductivity [43], however their temperature range is limited. The maximum service temperature, which is near 200°C for high performance adhesives, is inadequate to withstand the 300°C temperature required for the anodic bond. Glass frit bonds and anodic bonds, which permit bonding of dissimilar materials through the use of a thin intermediate glass layer, can withstand the required temperatures of the final bond step of the device. A glass frit bond, where the glass acts as an adhesive, is accomplished by applying a glass layer at the interface, then heating sufficiently to drive out the organic binders that are present in the glass. The glasses can be metal filled to produce an electrically conductive bond and low temperature glasses with processing temperatures near 400°C are available. The primary drawback of this method, though, is that it is difficult to remove the solvents and binders in the glass completely [44]. This problem is further complicated by the fact that, in MHT devices, the bond is contained in a small cavity. The other method in which a glass layer can be used to bond piezoelectric material to silicon

is to sputter or evaporate a thin layer of borosilicate glass on the piezoelectric element. An anodic bond can then be formed between the silicon and the glass layer by heating to a temperature of 300-500°C and applying an electric potential across the interface. This approach has successfully been used to bond bulk piezoceramics to silicon wafers [45], [46]. The use of an anodic bond is attractive because the thermal expansion of the glass can closely match that of silicon and the temperatures required are compatible with the existing processes in the device. The difficulty with the anodic bonding technique is that the glass can not be electrically conductive because of the voltage that must be applied across the interface to achieve a bond.

Brazing and soldering involve a wide range of materials and processing conditions. A typical process consists of heating the bond material, which is typically a metal alloy, above its liquidus temperature, allowing it to wet the surfaces to be bonded, and then cooling to solidify. The only difference between soldering and brazing is the temperature at which the bond is completed. If the alloy being used melts above 450°C, it is considered a braze, and if it falls below this temperature it is a solder. Solders are more prevalent in the realm of microelectronics packaging, because the lower processing temperatures prevent damage of sensitive electronics. In general, solders are divided into two basic categories, soft and hard. Soft solders typically have melting temperatures below 200°C, have low yield strengths, and are more susceptible to thermal fatigue and creep. Hard solders, which include eutectic compositions of AuSi (97wt.%Au-3wt.%Si), AuSn (80wt.%Au-20wt.%Sn) and AuGe (87.5wt.%Au-27.5wt.%Ge), have higher melting temperatures and yield strengths and are used more frequently in packaging applications, [43], [44]. Besides packaging applications, AuSi has also been used to bond three dimensional silicon microstructures [47], and AuGe to bond quartz layers in an accelerometer, [48].

The gold-based eutectic solders have excellent mechanical properties and are electrically conductive, which make them an attractive option for the bonding of piezoceramics to silicon. In addition, the bonds can be completed in a reducing atmosphere without the use of flux. The AuSi, AuSn, and AuGe eutectic solders melt at 363, 278 and 361°C, respectively. To ensure complete melting, bonds are often completed at

20-40°C above these temperatures. Thus, the fabrication temperatures are compatible with those required for the anodic bond. Further, the gold-tin processing temperature, which is close to 300°C, allows the anodic bond and silicon-piezoelectric bond to be accomplished simultaneously. Gold-tin has the lowest melting temperature, highest yield strength, and lowest modulus of the gold-based eutectic solders discussed [49]. The principal disadvantages of the gold-tin solder are the large thermal expansion coefficient of the solder, which can lead to large residual stresses, and the high gold content, which makes the bonding method expensive. Despite these drawbacks, the advantages of the gold-tin solder lead it to it's selection to bond piezoelectric elements to silicon in MHT devices. The gold-tin is a clear choice, however there have been various gold-tin bonding processes reported and the exact implementation of the bond was based on previous work and factors specific to the MHT device.

4.3 Gold-Tin Bonding Background

4.3.1 Applications

Gold-tin alloys have been used in a variety of packaging and microelectronic applications for more than 20 years. The principle use of the solder has been for die-attach applications, in which the gold-tin bond secures a silicon or gallium arsenide (GaAs) die to a ceramic substrate, such as alumina. The excellent thermal conductivity and high yield strength of the bond are often cited as the important factors in selecting gold-tin. More recently, gold-tin bonds have been used for optoelectronic packaging applications that require bonding of laser dies to diamond or silicon substrates. The relatively high melting temperature of the gold-tin, compared to typical lead-based solders, make the gold-tin system well-suited for these devices, which operate at elevated temperatures. Gold-tin bonds have also recently been used in electronic flip-chip applications [50], and the packaging of MEMS devices. In particular, it has been used to form interconnects in chemical sensors, [51], and is used to hermetically seal a glass cover on a commercial electrostatic projection display [52].

Figure 4-1: Gold-tin equilibrium phase diagram. [53].

4.3.2 Material Properties

The equilibrium phase diagram of the gold-tin binary system is shown in Figure 4-1 [53]. It is one of the more complicated binary systems and has two eutectic points. The common eutectic composition of 80 wt.% Au and 20 wt.% Sn melts at 278°C. Alloys of the second eutectic composition, 10 wt.% Au and 90 wt.% Sn melt at 217°C. A detailed review of the metallurgy is provided in reference [54]. Virtually all applications of the gold-tin system as a solder utilize the 80/20 eutectic composition.

Limited data exists on the mechanical properties of the gold-tin alloy. Olsen et al. report values for the thermal expansion, elastic modulus, and strength as a function of temperature for the 80 wt.% Au and 20 wt.% Sn alloy [49]. The room temperature values are listed in Table 4.1. These values were obtained from tensile tests conducted on cast specimens with a 2.8 cm gage length and cross-sections ranging from 0.12 to 0.2 cm^2. The size and fabrication of the specimen are significantly different than those of typical bonds. However, the values for thermal expansion and modulus should be reasonably good approximations. The strength values, though, will likely be different given the significant difference in geometry and loading between the specimens used and an actual bond.

Table 4.1: Room temperature mechanical properties of 80 wt.% Au and 20 wt% Sn alloy [49].

Young's Modulus	59.2 GPa
CTE	15.93 μm/m°C
Yield Strength	275 MPa
Ultimate Strength	275 MPa

4.3.3 Process Overview

Two primary methods have been employed for fabricating gold-tin bonds. The difference between the two methods is in how the gold-tin material is applied. The traditional approach is to use a gold-tin preform, which is a thin strip of the alloy that is typically 25-50 μm thick. The bond is accomplished by placing the preform between the die and substrate and heating to above the melting temperature of the alloy. The surfaces to be bonded must typically be metallized so that the solder wets the components. In addition, a clamping pressure or a scrubbing motion is used to promote wetting and break the tin oxide, which is found on the as-fabricated preforms. The alternative approach is to deposit a series of gold and tin layers on one of the components to be bonded. Upon heating, the gold and tin melt and interdiffuse to form a gold-tin alloy. This approach was developed so that thinner bonding layers could be achieved and oxide on the surface reduced. The tin-oxide on the surface is prevented by depositing the gold and tin layers such that gold is the final layer deposited, thus protecting the tin layer from atmosphere and oxidation. Details of these methods, which have been used in previous work to bond silicon and GaAs dies to alumina substrates, are described below.

Preforms are commercially available in a variety of dimensions and can be purchased in ribbon form or stamped geometries. The solder will not readily wet silicon dies, GaAs dies, or ceramic substrates, thus the bonding surfaces need to be metallized prior to bonding. The metallizations typically employed consist of multiple layers and must adhere well to the components, protect against diffusion, and provide a layer that is easily wetted. Successful bonding of silicon and GaAs dies to alumina substrates has been reported using gold-tin preforms, where a chromium and a gold

Table 4.2: Typical processing conditions for AuSn preform solder bonds.

	DIE			SUBSTRATE	
	Material	Deposition (μm)	Size	Material	Deposition (μm)
A	GaAs	0.04 Cr, 0.5 Au	4x4 mm	alumina	0.025 Cr, 5.0 Au
B	Si	0.04 Cr, 0.5 Au	4x4 mm	alumina	0.025 Cr, 5.0 Au
C	GaAs	0.1 Ti, 0.5 Au	5.14x5.18 mm	alumina	0.5 Cr, 7.0 Au
D	GaAs	0.1 Ti, 0.5 Au	1.16x0.81 mm	alumina	0.5 Cr, 7.0 Au

	PROCESS			STRENGTH		
	Temperature	Atmosphere	Pressure (MPa)	Loading	Value (MPa)	Ref.
A	310°C	H_2,N_2	0.28-0.42	shear	2.45-6.8 MPa	[56]
B	305°C	H_2	0.14	tensile	>1.4 MPa	[57]
C	310°C	N_2	0.05 w/ scrubbing	shear	>4.5 MPa	[58]
D	310°C	N_2	0.05 w/ scrubbing	shear	19.6-23.6 MPa	[58]

capping layer were deposited on the dies and substrates. The chromium layer, which was deposited first, served as an adhesion layer and a diffusion barrier, and the gold layer was employed to promote wetting [55], [56], [57]. Other studies have reported the use of a two-layer metallization of titanium and gold to achieve similar results [58]. To complete the bond, the gold-tin preform is placed between the metallized components and heated to approximately 310°C. A nitrogen or hydrogen ambient is typically used to prevent oxidation during heating [56], [58]. A scrubbing technique or an applied static pressure has been used to break the surface oxide and produce bonds with good homogeneity and relatively few voids. The magnitude of the clamping pressures used range from 0.05 to 0.42 MPa. The details of the work discussed above are summarized in Table 4.2.

The alternative approach that has been employed to form gold-tin bonds is to deposit layers of gold and tin on one of the components to be bonded. In previous work, the gold and tin films were deposited using evaporation over an adhesion layer of chromium or titanium, which was deposited on to the silicon or GaAs dies [59], [60], [61]. All the films are deposited in one vacuum cycle to avoid oxidation of the tin. The component that mates with the layer containing the gold-tin composite must be metallized. Typical metallization schemes have included a chromium or titanium adhesion layer followed by a gold capping layer. To complete the bond,

Table 4.3: Typical processing conditions for AuSn thin-film solder bonds.

	DIE			SUBSTRATE	
	Material	Deposition (μm)	Size	Material	Deposition (μm)
A	Si	0.1 Cr, 0.1 Au, 1.0 Sn, 0.1 Au	10x10 mm	Si	0.1 Cr, 1.0 Au
B	GaAs	0.07 Cr, 0.815 Sn, 0.065 Au	5x5 mm	Si	0.07 Cr, 1.6 Au
C	GaAs	0.03 Cr, 0.5 Au, 2.25 Sn, 0.75 Au	4x4 mm	alumina	0.03 Cr, 6.4 Au

	PROCESS			STRENGTH		
	Temperature	Atmosphere	Pressure (MPa)	Loading	Value (MPa)	Ref.
A	350°C	air	0.07	tensile	2.0 MPa	[60]
B	272 or 286°C	H_2 w/ N_2	used, not specified	-stronger than GaAs-		[61]
C	320°C	H_2	0.28	-not tested-		[59]

the pieces were assembled and heated in an inert or reducing atmosphere to a temperature between 310° and 350°C. It should be noted that this multilayer concept is only effective because of the fact that the tin melts at 232°C, which is lower than the melting temperature of the 80/20 eutectic alloy. This approach would not work for the AuSi or AuGe solders in which the individual constituents melt at a higher temperature than the eutectic compositions [59]. With the gold-tin multilayer bonds, a static pressure of the same magnitude as that used for preform bonding was used. It is interesting that a pressure appears to be required despite the absence of the tin-oxide layer. Specific processes that have been employed to achieve bonds with few voids are detailed in Table 4.3.

4.3.4 Mechanical Integrity

Reported failure stress values are listed in Tables 4.2 and 4.3 for gold-tin bonds formed using preforms and thin-films. The degree of mechanical characterization is quite limited in the work outlined above. The relative paucity of the data is primarily due to the fact that the majority of work has been devoted towards packaging applications. Detailed understanding of the mechanical integrity of the bond is often not the objective of the work, but rather the focus is to determine whether or not the bond is comparable to other packaging technologies. This is often assessed by conducting simple tensile or shear tests and comparing the results to guidelines

outlined in a specific standard. A common standard, which was used to assess bond strength in references [56], [57], and [58], is MIL-STD-883 [62]. The standard gives simple criteria, which consist of certain failure loads that dies of different sizes must be able to withstand for various loading configurations. Thus, data on the mechanical properties of the bond are limited.

Despite the limited data, it is possible to establish a general range of expected bond strengths from the values listed in Tables 4.2 and 4.3. Typical strengths are below 10 MPa and the highest value that was reported is 23.6 MPa. The type of tests used to obtain these values are quite sensitive to the exact geometry tested and any flaws that may be present. In addition, the failure stress values are likely a function of the substrate and die material being bonded. Researchers have reported die fracture rather than failure in the bonding layer in several studies [57], [55]. Thus, while values given Tables 4.2 and 4.3 establish a general range of bond strength values, the factors discussed above should be considered when examining this data.

4.4 Device Assembly

In order to design the bonding process, an understanding of the MHT device assembly process is required. The bonding of the piezoelectric element to the silicon is one of the final fabrication steps of the device. This bond is completed on the die-level with the upper and lower layers fully assembled. Figure 4-2 illustrates the basic process of the final bonding step. The lower layer, composed of two glass layers and one silicon layer, forms a chamber which holds the piezoelectric element. The top layer includes a stack of multiple silicon wafers bonded to a glass packaging layer. The drive piston, which the piezoelectric element actuates during device operation, is located in the silicon structure of the upper layer. Assembly is accomplished by manually placing a small piezoelectric cylinder in the lower chamber and aligning and bonding the upper stack to the lower stack using an anodic bond. A gold-tin solder layer on the ends of the piezoelectric element is melted by heating to approximately 300°C, the temperature used for the anodic bond. Upon cooling, the solder layer bonds

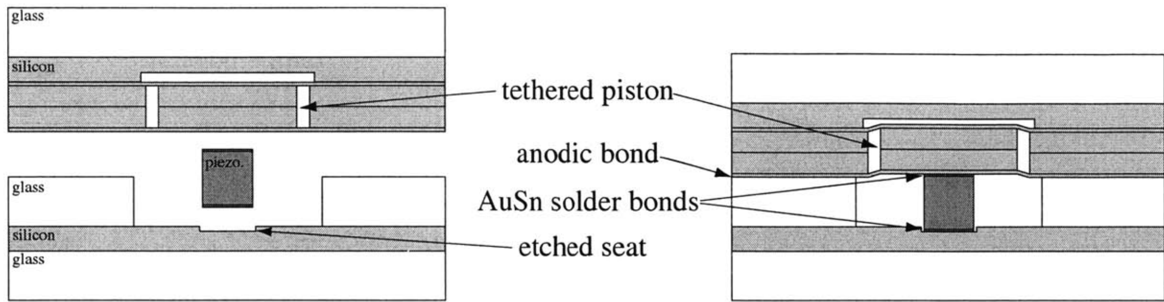

Figure 4-2: Final MHT bonding process.

the piezoelectric element to the silicon piston. A shallow etch in the lower silicon layer defines a seat, which allows precise positioning of the piezoelectric element. The height of the piezoelectric element, the height of the middle glass layer, and the depth of the etched seat are carefully controlled and measured such that the piezoelectric element is oversized and causes the membrane to be displaced 1-2 μm prior to any actuation. The displacement of the piston leads to a preload on the piezoelectric element, which supplies a clamping pressure to the bond and assists in keeping the bond in compression during device operation.

The magnitude of this pressure is important in designing the bonding process since it is the only clamping force that can be applied to the joint during bonding. The oversized piezoelectric element displaces the tethered piston, compresses the piezoelectric element slightly, and causes limited deflection in the lower plate. The tethered piston, which typically has tethers 10-20μm thick, and the piezoelectric element, which has a relatively low elastic modulus (E_{PZT-5H} = 63 GPa, E_{PZN-PT} = 9 GPa), are the most compliant components in the system. The bottom plate, which is a 500 μm thick silicon layer laminated to a 3 mm layer of glass, is assumed to be rigid compared to the membrane and piezoelectric element. Based on these assumptions, the force

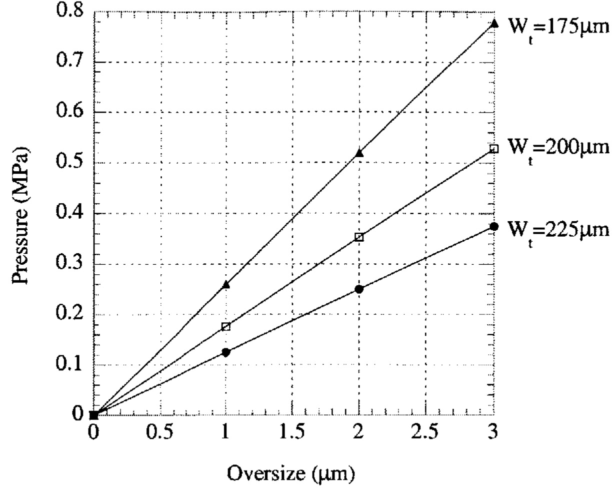

Figure 4-3: Bond pressure as a function of tether width and piezoelectric element oversize.

acting on the piezoelectric element, F_P, due to an oversize, δ, can be written as

$$F_P = \delta \frac{k_m k_p}{k_p + k_m}, \tag{4.1}$$

where k_m and k_p are the stiffness of the membrane and the piezoelectric element, respectively. The force on the piston and the corresponding pressures on the bond were calculated for a range of typical oversize values, δ. The results, which are plotted in Figure 4-3, are for a typical double layer piston geometry with a 6.8 mm inner diameter, a tether thickness of 10μm, and the tether widths shown. It was assumed there were three PZN-PT piezoelectric elements in the chamber each with a diameter of 1.5 mm and a length of 1 mm. These results are for a specific case, however, it is believed that the values chosen above result in the most conservative pressure estimate (the lowest applied pressure possible is seen as the conservative case, since higher applied pressures appear to lead to better bonding) based on the current design of MHT devices. Since a minimum oversize of 1 μm is expected and 225 μm is currently the widest tether in the design, the bond should have a minimum of 0.13 MPa applied during device assembly.

4.5 Bonding Process

The previous work using gold-tin bonding summarized in Section 4.3.3 illustrates the basic bonding process and the approaches that have been employed. The dimensional tolerances required in MHT devices led to the selection of a thin film gold-tin bond rather than the use of a preform. The piezoelectric element with the bonding layer must be sized to within 1 μm of the specified length. Commercially available preforms have thicknesses between 25 and 50 μm and thickness tolerances of +/- 5μm. This tolerance, along with the difficulty of handling a preform that is 25 μm thick and 1-2 mm in diameter, were the principal factors in choosing to use a thin-film bond. The approach adopted differs from the thin-film bonding techniques discussed in Section 4.3.3 in that the gold-tin is deposited as an alloy rather than alternating layers of gold and tin. The device geometry and assembly prohibits the use of a scrubbing technique and requires that a static pressure be applied to the bond. The process was developed with these constraints in mind. The details of the bonding process that has been developed are given below.

The multiple layers of metal that are deposited on the silicon and the piezoelectric components to be bonded are shown in Figure 4-4. The starting piezoelectric material were PZT-5H or PZN-PT plates, 12 to 25 mm in diameter, that were ground and polished to a thickness of 1 mm and a surface roughness of 0.5 μm. Prior to deposition, the plates were cleaned using a weak nitric acid solution (20:1 H_2O:HNO_3) followed by a deionized water rinse. The four layer film structure on the piezoelectric plates was deposited in one vacuum cycle using RF sputtering. The 50 nm thick titanium layer and the 250 nm thick platinum layer serve as the adhesion layer and diffusion barrier, respectively. The gold-tin layer, which is 4 μm thick, is sputtered from an alloy target that has an 80 wt.% Au - 20 wt.% Sn composition. Sputtering was chosen over evaporation because sputtering allows the stoichiometry of the target to be maintained in the deposited film [63]. The final layer is a gold capping layer, 50 nm thick, that serves to prevent the gold-tin film from oxidizing. The multi-layer film structure on the silicon pieces allows the solder to wet the silicon. The films were

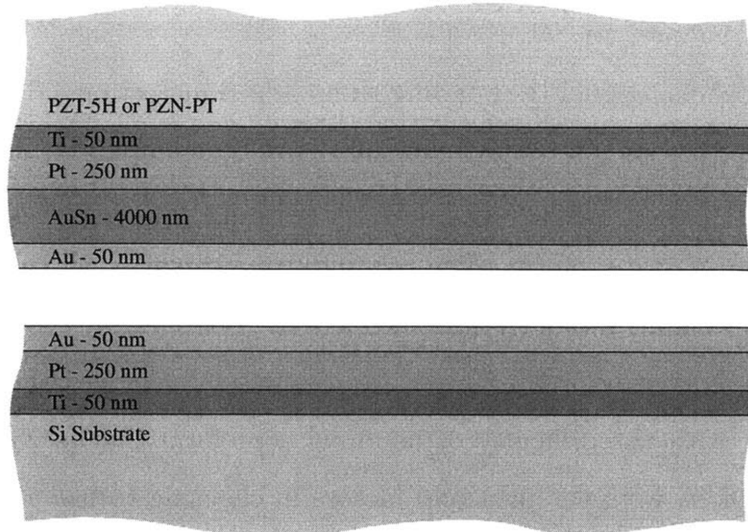

Figure 4-4: Deposited metal layers used to fabricate the gold-tin solder bonds.

deposited on the silicon pieces, which had been cleaned with a standard 'piranha' clean (3:1 H_2SO_4:H_2O_2), using electron-beam evaporation in one vacuum cycle. For the test bonds in this study, the metallization layer was deposited uniformly on a 4" silicon wafer. In the actual device, where selective deposition of the metallization layer is required, deposition is done on the die-scale using a shadow mask. The titanium adheres well to the silicon and the platinum helps to prevent diffusion. The gold layer ensures that the gold-tin solder can easily wet the surface. The gold capping layer on the silicon pieces as well as the piezoelectric elements causes the gold-tin alloy to become slightly gold-rich. However, since the gold layers are thin (50 nm), as compared to the 4 μm thick gold-tin layer, the change is small and the gold fraction in the final bond remains less than 80.5 wt.%.

The test specimens used in developing the process were nominally 2.5×2.5 mm and 3.5×3.5 mm piezoelectric pieces bonded to 10×10 mm silicon dies. The individual piezoelectric pieces and silicon dies were cut from the larger piezoelectric plates and silicon wafers using a diamond wafer saw. Prior to dicing, the surfaces were coated with a thin layer of Crystallbond™ thermal wax, which was applied by heating the pieces to 100°C and spreading the wax. The wax, which is hard at room temperature, was used to suppress chipping of the film at the die edges and to protect the surface

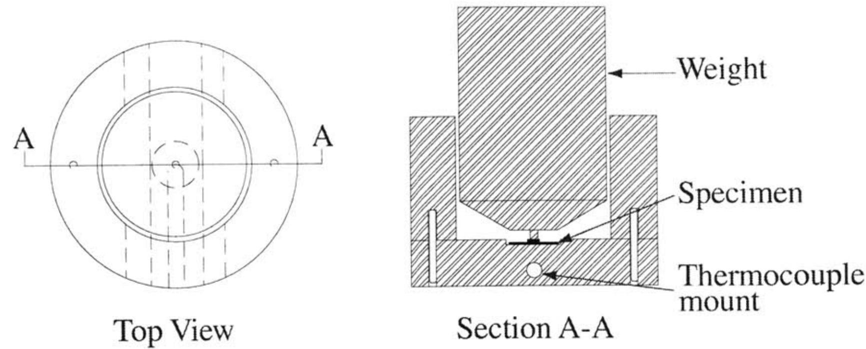

Figure 4-5: Solder bonding jig.

from particulates during dicing. While this method has proved successful in protecting the specimens during dicing, heating to 100°C has the possibility to lead to oxidation of the tin. The wax was removed by soaking the diced pieces in acetone. Complete removal of the wax was ensured by a second acetone clean in an ultrasonic bath. Immediately prior to bonding, the silicon and piezoelectric components were cleaned with sequential acetone, methanol, and isopropanol rinses. The specimens were dried with filtered N_2 following the isopropanol rinse.

The bonds were assembled and a clamping pressure was applied using a special jig. The jig, which is illustrated in Figure 4-5, applies a static pressure using a weight. A weight was used to provide the loading in order to avoid changes in clamping pressure due to thermal expansion of the jig. The jig dimensions were chosen such that the pressure applied on the specimen was near the minimum clamping pressure expected in the device, 0.13 MPa. A type K thermocouple, located in the jig directly beneath where the specimen sits, permitted an accurate measurement of the temperature of the specimen. Following assembly and mounting, the specimen and jig were transferred to a vacuum oven. The vacuum oven used has the capability to heat to 600°C and maintain pressures as low as 5×10^{-3} torr.

To prevent oxidation of the tin in the solder, bonding was carried out in an Ar-5%H_2 atmosphere. The presence of H_2 in the atmosphere produces a reducing atmosphere that can help to remove any stable oxides that may be present on the solder. To achieve the desired atmosphere in the oven, the chamber was evacuated to

10^{-2} torr and then purged with the Ar-5%H_2 gas. The chamber was backfilled with the gas until a pressure of 20 inHg was reached. The chamber was then evacuated a second time to 10^{-2} torr. The chamber was backfilled again with the reducing atmosphere until a pressure of 20 inHg was reached. A slight vacuum of 20 inHg was maintained when backfilling because the seals on the oven do not support positive pressures. Following the two evacuation and purge sequences, the chamber was heated to a maximum temperature between 300 and 325°C. A range of temperatures is given because it was discovered that solder from different deposition runs often melt at slightly different temperatures. This variation is believed to be due to slight compositional variations in the solder. Once the maximum temperature was reached, the chamber was evacuated to 10^{-2} torr. The bond was allowed to soak at the desired temperature for approximately $\frac{1}{2}$ to 1 hour. Following the soak time, the bond was cooled under vacuum. The soak and cool stages are completed under vacuum to ensure that any trapped gases are removed from the bond. The temperature and pressure cycle used to complete a bond is summarized in Figure 4-6. As seen in Figure 4-6, the heat and cool times are quite long. The length of these times is due to the nature of the oven and the mass of the jig that was used. It is believed that shorter times could be realized if different equipment was employed.

Following cooling, the bond was removed from the oven. Bonds produced via this process were examined for voids and mechanically tested using a tensile loading. The process outlined above was developed iteratively based on the results of these experiments. The details and results of the qualitative evaluation of bond quality and the mechanical characterization are detailed in the following sections.

4.6 Qualitative Evaluation of Bond Quality

The primary focus of the process development work was to produce void-free bonds. Elimination of voids in the bond is critical. Voids inherently reduce the strength of the bond and are stress raisers, which can serve as fatigue crack initiation sites. To inspect for voids, bonded specimens were cross-sectioned and polished, then examined using

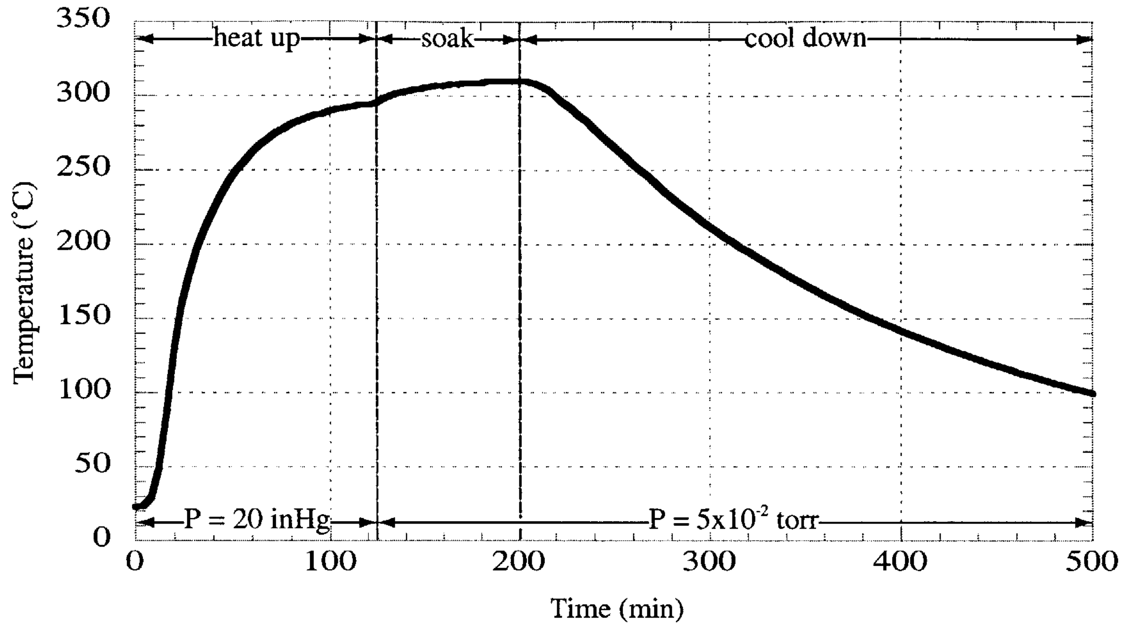

Figure 4-6: Temperature and pressure cycle to complete bond.

a scanning electron microscope (SEM). The inspection process, while destructive, is straightforward and allows small voids to be identified. The results of several examinations of gold-tin bonds between two silicon pieces or silicon and PZT-5H or PZN-PT are discussed below. All the bonds discussed were fabricated according to the process outlined in Section 4.5 except where differences are noted. The bonds between two silicon pieces were carried out identically to the silicon-piezoelectric bonds, except for the fact that the substrate with the gold-tin layer was silicon rather than a piezoelectric material.

Figure 4-7 shows two examples of early bond attempts. While the bonds appeared mechanically sound, the cross-sections revealed that the bond contained numerous voids and un-bonded regions. The bond in Figure 4-7(a) was bonded with no applied pressure and cooled in an Ar-5%H_2 environment with a pressure of 5 inHg. It was found that voids such as those shown in Figure 4-7(a) could be eliminated by applying a static pressure during bonding and cooling under vacuum. Experiments indicated that either cooling under vacuum or applying a static pressure alone, was not sufficient to eliminate voids of this nature. The use of both appears to be required to consistently prevent voids such as these. Figure 4-7(b) shows a poorly bonded inter-

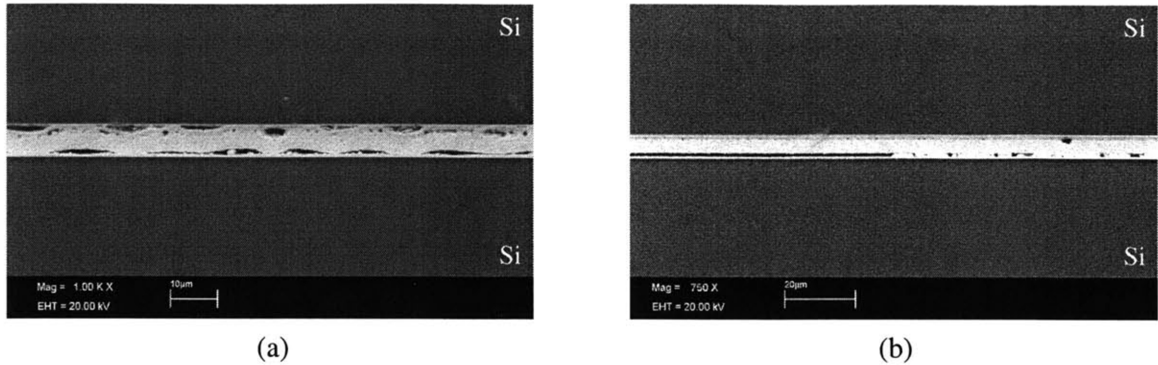

(a) (b)

Figure 4-7: Two examples of poor bonding, (a) due to the presence of trapped gas, (b) due to poor cleaning.

face of a different nature. Large un-bonded regions are visible at the interface, where the layer with the deposited gold-tin solder mates with the substrate with the gold metallization layer. It is believed that poor bonds such as these are a result of poor cleaning of the interfaces prior to bonding.

Void-free bonds, such as the one shown in Figure 4-8, were routinely obtained if the cleaning procedure and process outlined in Section 4.5 were followed. Figure 4-8 shows a void-free bond between two silicon pieces. The final bonding layer is 5.4 μm thick, which is thicker than the total specified thickness of the deposited films. Bonds with thicknesses varying from 3.5 μm to 5.5 μm have been observed. It is believed this is due to variations in the thickness of the deposited films, since specimens cut from the same silicon wafer or piezoelectric disk tend to have similar bond thickness. A variation of 1-2 μm from the design value is not a major concern in device fabrication, since the piezoelectric element dimensions are measured following deposition and the fact that the device fabrication process permits compensation of small deviations. However, it should be possible to obtain films of consistent thickness, if the deposition system is well calibrated and the same system is used for all depositions. Deposition in the current study was outsourced and two different vendors[1,2], were used over the course of this work.

Once a reasonable process was established for producing void-free gold-tin bonds

[1] Vacuum Process Engineering, 4261 Power Inn Road, Sacramento, CA 95826
[2] Professor Sy-Hwang Liou, University of Nebraska, 364 Behlen, Lincoln, NE 68588

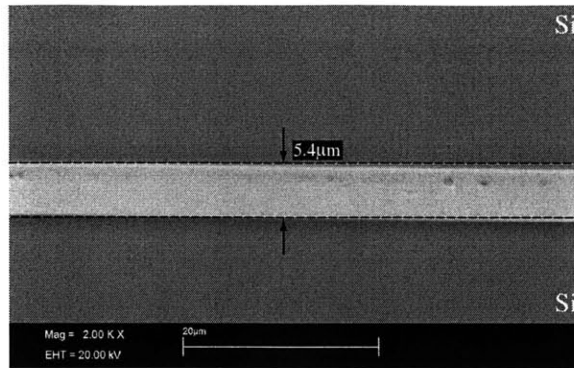

Figure 4-8: Void-free AuSn bond of silicon to silicon.

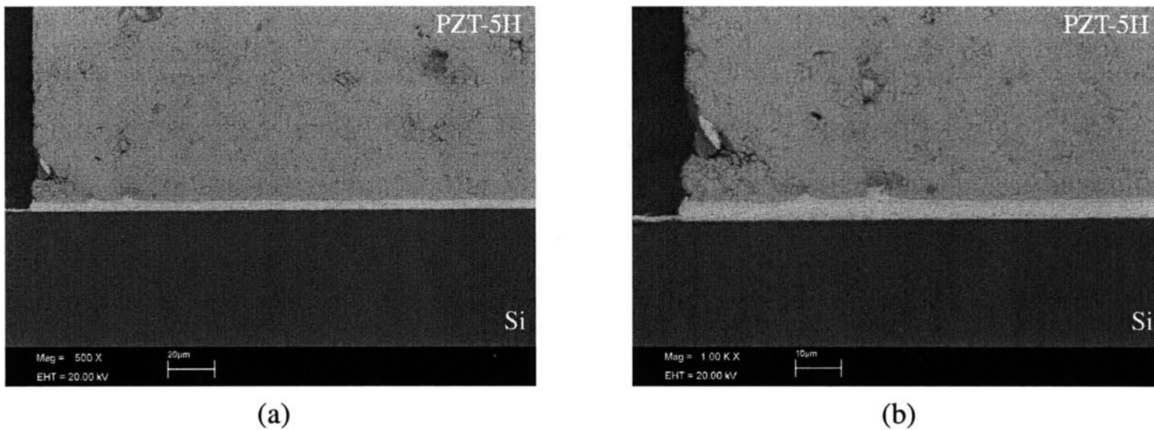

(a) (b)

Figure 4-9: Void-free AuSn bond of PZT-5H to silicon.

between two silicon components, PZT-5H/Si and PZN-PT/Si bonds were fabricated. A cross-section of a gold-tin bond between PZT-5H and Si is shown in Figure 4-9. The specimen appears well bonded and to be void free. While the PZT-5H is polished prior to bonding, small surface defects are sometimes present. Small defects in the PZT-5H that were filled by the solder are clearly observed in the cross-sections shown in Figure 4-9. This is encouraging because it indicates that the solder allows for compensation of rough or imperfect surfaces. The final important feature to recognize in Figure 4-9 is the geometry of the bond layer at the edge. A fillet is not formed and there appears to have been little flow of the solder beyond the edge of the PZT-5H material. This behavior was routinely observed and has the potential to limit the load carrying capability of the bond.

The gold-tin bonds between PZN-PT and silicon had appearances similar to the

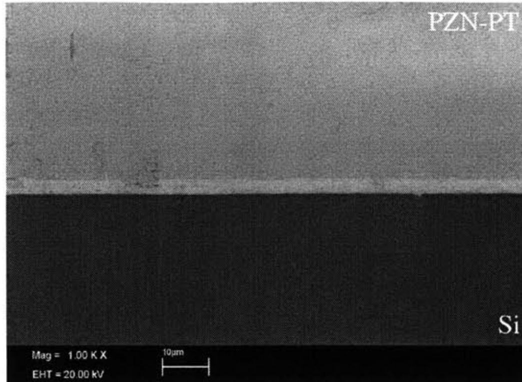

Figure 4-10: Void-free AuSn bond PZN-PT to silicon.

bonds fabricated between PZT-5H and silicon components. A PZN-PT element bonded to a Si substrate is shown in Figure 4-10. The bond layer is continuous and void-free. Again, the capability of the gold-tin to fill imperfections in the surface can be observed.

The SEM evaluations of the bonds allowed a bonding process to be developed to produce void free bonds. The results presented demonstrate that bonds can be achieved between two silicon pieces, or a silicon and a PZT-5H or PZN-PT piece. While these results were encouraging and were useful for process development, they did not provide any information pertaining to the mechanical strength of the bond. Thus, following development of a process to produce void-free bonds, simple mechanical tests were conducted to gain additional information regarding the bond integrity.

4.7 Tensile Tests

4.7.1 Experimental Procedure

Simple tensile tests were performed on piezoelectric elements bonded to silicon substrates using the thin film gold-tin solder bond developed in this work. The purpose of these tests was not to investigate systematically the effect of processing parameters, but, rather was to establish typical strength values for the bonds and to identify potential weaknesses of the bonding technique. The specimens were designed to replicate closely the actual geometry found in the device. The specimen, which is shown

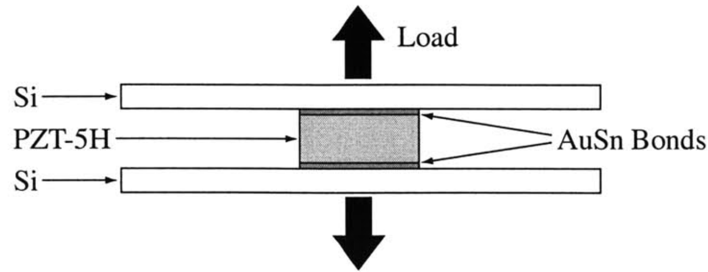

Figure 4-11: Tensile specimen geometry.

schematically in Figure 4-11, consists of a nominally 2.5×2.5 mm or 3.5×3.5 mm PZT-5H element bonded between two 10×10 mm silicon dies. The specific specimen geometry was chosen to facilitate specimen gripping and mounting. The area-ratio between the silicon plates and the solder-bonds allow bonds with strengths greater than that of the epoxy used to mount the specimen to be tested. It should be noted though, that while the specimen geometry makes mounting possible, the presence of two interfaces increases the probability that a specimen will fail at a lower load. Specimens were fabricated using the process outlined in Section 4.5.

The specimens were mounted to aluminum studs using Devcon 5-Minute Epoxy™. A mounted specimen is pictured in Figure 4-12(a). As shown in Figure 4-12(b), the aluminum studs were secured into two collars mounted in a standard servo-hydraulic testing machine. The lower collar was mounted to the movable crosshead of the test machine. The upper collar was attached to a 100 N load cell mounted on the fixed crosshead. The upper collar was connected to the load cell via a 0.3 m long 0.5 mm diameter steel cable. The cable provided a compliant coupling between the test machine and the load cell and was included to mitigate the effects of any misalignment that may have been present. Specimens were loaded at a constant displacement rate of 0.3 mm/min until failure occurred. The failure stress was calculated from the load at failure and the cross-sectional area of the specimen as measured using a micrometer.

4.7.2 Results

The results of five tensile tests that were conducted on PZT-5H bonded to silicon are listed in Table 4.7.2. The failure stress values listed span an order of magnitude,

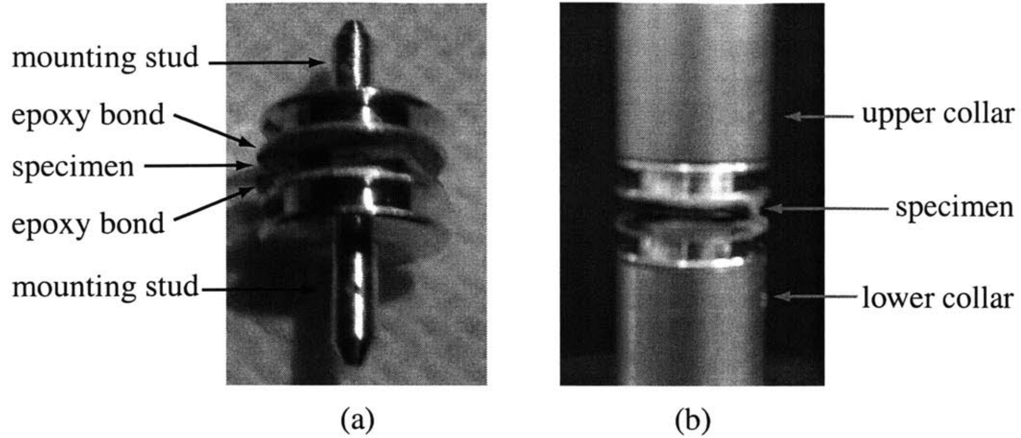

Figure 4-12: Tensile specimen, (a) mounted to studs, (b) mounted in test machine.

Table 4.4: Tensile test results.

Specimen	Processing Temperature (°C)	Applied Pressure (MPa)	Failure Stress (MPa)
A	305	0.15	2.8
B	305	0.15	3.2
C	305	0.15	9.0
D	325	0.15	0.8
E	305	0.31	5.0

0.8 MPa to 9.0 MPa. The scatter in the data is not entirely surprising given the geometry of the specimen. The measured failure load is very sensitive to defects in the bond or piezoelectric material. While there is scatter in the data, a degree of correlation exists between the failure stresses measured and the appearance of the fracture surfaces.

Significant differences in the appearance of the fracture surfaces were observed between the specimens that failed at higher loads, specimens C and E, and the specimens that had lower failure stresses, specimens A, B, and D. Figure 4-13 and Figure 4-14 show the fracture surfaces of specimens C and B, respectively. In specimen C, the failure occurred primarily along the interface between the PZT-5H and the titanium adhesion layer. The speckled pattern observed on the surfaces in Figure 4-13 are small PZT-5H pieces that have pulled out from the surface of the piezoelectric element. Over a small area near the center of the specimen, failure did not occur at the PZT-5H/film interface, but, rather occurred within the bonding layer. The fracture

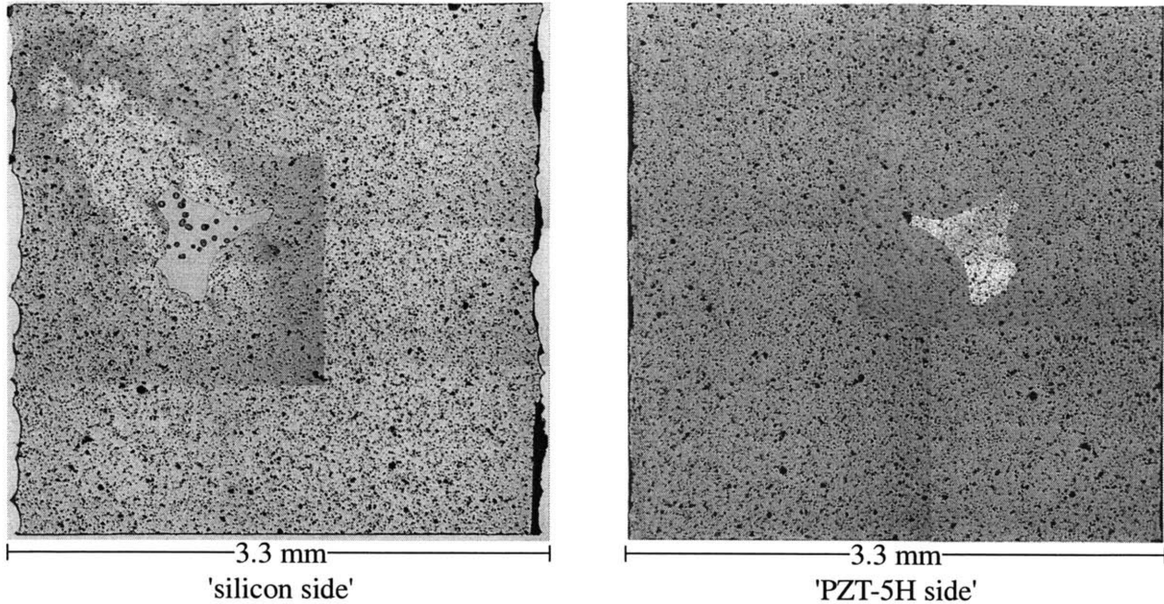

Figure 4-13: Micrograph of fracture surface of specimen C.

surface of this specimen indicates that at high failure loads the interface between the film and the piezoelectric element is the factor that limits bond strength.

The fracture surface of specimen B, pictured in Figure 4-14, is similar in appearance to the surfaces of specimens A and D. The following features, which can be observed in Figure 4-14, were present on all of these specimens that failed at relatively low stresses.

- Areas with pull-out of large pieces of piezoelectric material. These areas, which appear as black regions, are where significant fracture has occurred in the piezoelectric material.

- Small areas where failure has occurred between the film and the PZT-5H. These areas are identical to those observed in specimen C and consist of delamination between the titanium film and the PZT-5H as well as the pull-out of small pieces of PZT-5H.

- Large areas of failure within the bonding layer. This failure is believed to occur at the interface between the gold-tin alloy and the gold metallization layer on the silicon substrates.

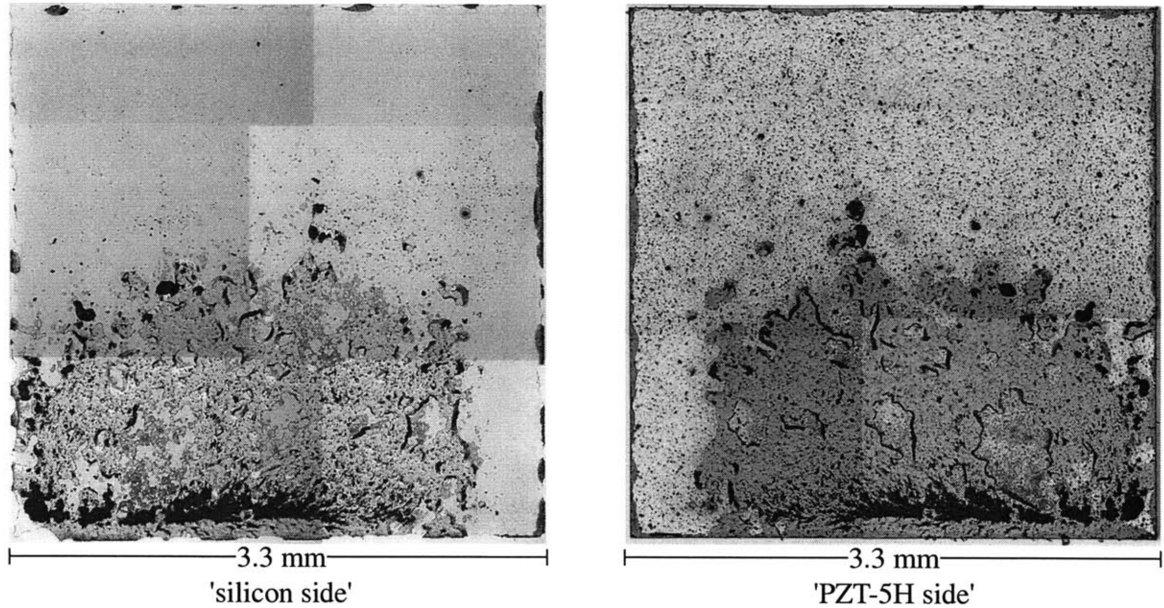

Figure 4-14: Micrograph of fracture surface of specimen B.

These features indicate two possible failure modes for these specimens. The first, which is suggested by the large fractured regions in the piezoelectric material, is that the PZT-5H element contained a flaw that led to fracture of the PZT-5H at a low load. The other possible failure mode is that a section of the interface was poorly bonded and fracture was able to begin in the bond itself. Once a portion of the solder layer failed, the local stress on the well-bonded regions increased and lead to fracture in the PZT-5H. If the latter case is the true mode of failure, it is possible that poor bonding may have been caused by contamination on the surface and inadequate cleaning.

Despite the uncertainty with respect to the exact failure mode of the specimen, the potential limiting factors of the bond strength can be identified. The primary mode of failure that was observed in the specimens with high failure stresses was clearly adhesive failure between the PZT-5H and the titanium adhesion layer. This failure is believed to be a combination of the low strength of the PZT-5H, as indicated by the pull-out, and the quality of adhesion of the titanium film. The lower failure stresses that were incurred in specimens A, B, and D are believed to be due to flaws in the PZT-5H material or a poorly bonded interface. However, the qualitative evaluation of

bond quality discussed in Section 4.6 indicates that homogenous bonds with few voids can be formed, and suggests that poorly bonded interfaces can be avoided. Thus, it appears that the limiting factor of the bond strength is the PZT-5H material and its interface with the titanium adhesion layer.

4.8 Conclusions and Recommendations

A process to produce thin-film gold-tin bonds between piezoelectric elements and silicon substrates has been developed. The bonding method was selected based on the requirements of the MHT device. The process has been developed such that void-free bonds can routinely be fabricated. Bonds were cross-sectioned and examined to verify the uniformity of the bonds and the absence of voids. Simple tensile tests were conducted on PZT-5H elements bonded to silicon. The results, although limited, indicate the strength of the bond is limited by the strength of the titanium - PZT-5H interface. It is unclear whether a different adhesion layer would result in higher bond strengths, since fracture of the PZT-5H itself is often observed when the interface fails.

While a bond process has been developed, the degree of mechanical characterization of bond quality has been limited. In order to ensure reliable device design and an optimal fabrication process, further tests must be conducted. In particular, the fatigue behavior and long term reliability of the bond need to be studied. In addition, a detailed study with systematic variations in the process conditions is required in order to ensure an optimal process. The fatigue behavior of the bond is probably best observed through the operation of prototype devices. Actual devices permit accurate representation of the stress-state at the interface and allow a large number of cycles to be applied. The study of the effect of the process parameters on bond quality could be conducted using a specimen similar in geometry to the DCB or 4-point bend specimens discussed in Chapter 2. These specimens would decrease the sensitivity of the measured values to the exact geometry of the specimen. While these tasks are required to fully validate the bonding technology, the current work has clearly

demonstrated the potential to employ gold-tin bonds to bond piezoelectric elements to silicon in MHT devices.

Chapter 5

Conclusions and Recommendations

This work has addressed several issues that are critical to the development of MHT devices. These issues, while particularly relevant to MHT devices, may also have relevance in the development of other microscale devices. Three distinct topics have been investigated in the current work: silicon fusion bonding, strength of SOI membranes, and gold-tin bonding. In each area, key accomplishments have been made. The key achievements of this work are highlighted below.

- A four-point bend delamination specimen was employed to measure the toughness of silicon fusion bonds. It was demonstrated that the specimen was effective for characterizing low toughness bonds, but was not suited for testing bonds where the toughness approaches that of the bulk material.

- Silicon fusion bond toughness was measured as a function of processing conditions for bonds with toughnesses lower than 2.5 J/m^2. It was shown that while the initial contacting conditions, such as time and pressure do not have a significant effect on bond quality, the anneal temperature and time have a profound impact on bond toughness.

- The fracture strength of membranes fabricated from SOI wafers using deep reactive ion etching was measured. The results indicated that the fracture strength, which was considerably lower than that reported for deep reactive ion etched bulk silicon, was highly dependent on the SOI manufacturer.

- A process has been developed for producing void-free thin-film gold-tin eutectic bonds between silicon substrates and piezoelectric elements. Tensile tests demonstrated that the strength of the bonds is limited by the PZT-5H/solder interface.

While significant progress has been made in this work, the results of the work also lead to additional questions and demonstrate the need for further investigation of certain issues. Based on this, several recommendations for future work are itemized below.

- To fully map the effect of process parameters on silicon fusion bond toughness, additional tests must be completed. It is likely that an alternative specimen geometry will be required, so that bonds with higher toughnesses can be tested.
- To provide a more reliable strength value for the design of SOI membrane structures, variation in the fabrication and processing of such structures must be reduced. While variation will always be present in strength data of silicon, which is brittle, reduction of the variation would allow the data to be fit to a statistical distribution and permit the use of probabilistic design techniques.
- In order to refine the gold-tin bonding process that has been developed, a systematic investigation of processing conditions on the bond strength is required. To complete this study, however, it is highly recommended that a mechanical testing specimen, which is less sensitive to geometry than a tensile specimen, be employed.
- To ensure the reliability of MHT devices, a detailed study of the effects of cyclic loading on the gold-tin bond must be completed.

Despite these issues, which should be investigated further, it is clear that this work has made progress and provided insight into the principal materials and structures concerns that must be addressed to permit the development of MHT devices.

Appendix A

Photolithography Masks

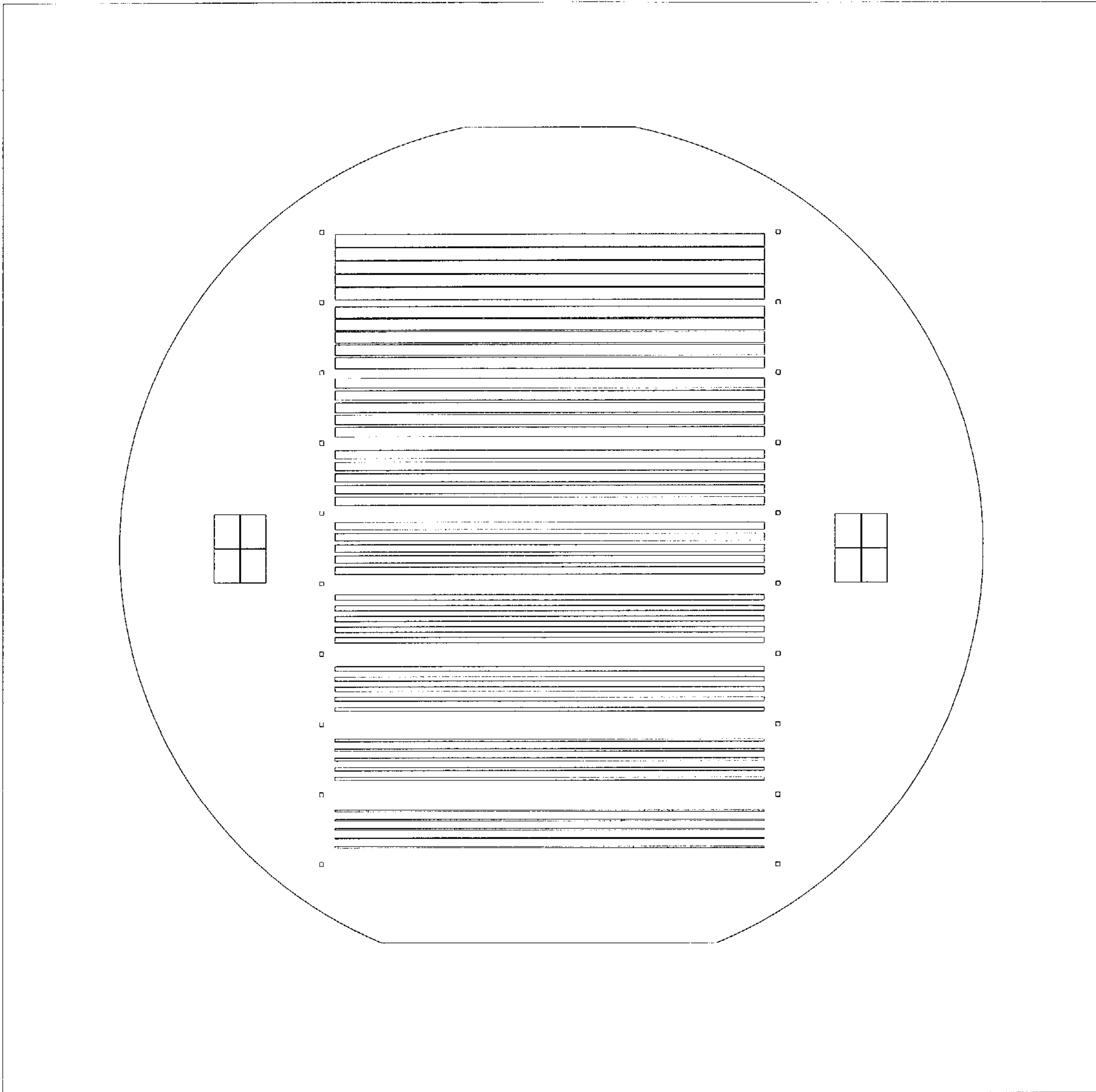

Figure A-1: Mask layout to define shallow grooves in standard 4-point specimen.

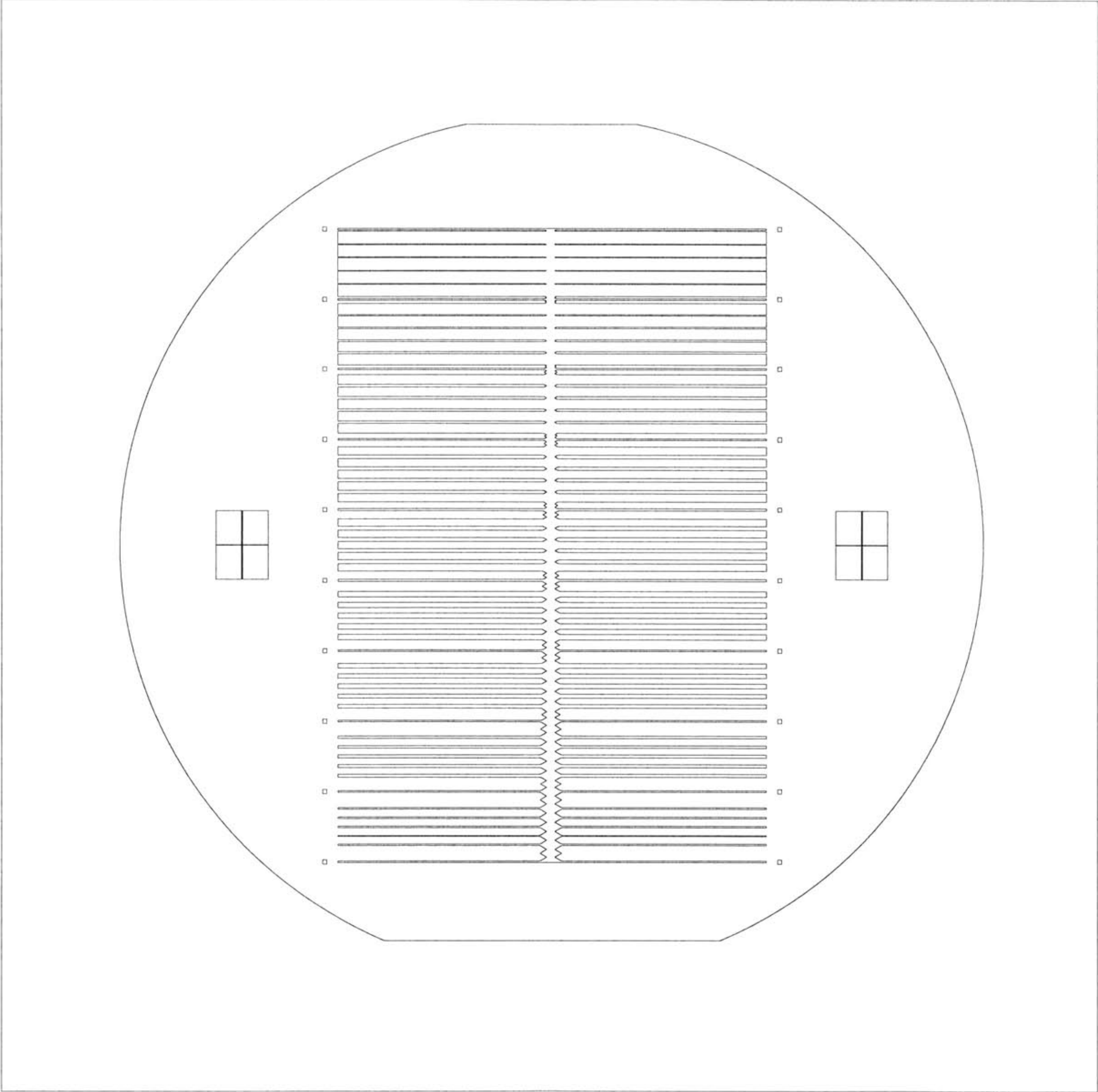

Figure A-2: Mask layout to define shallow grooves in 4-point chevron specimen.

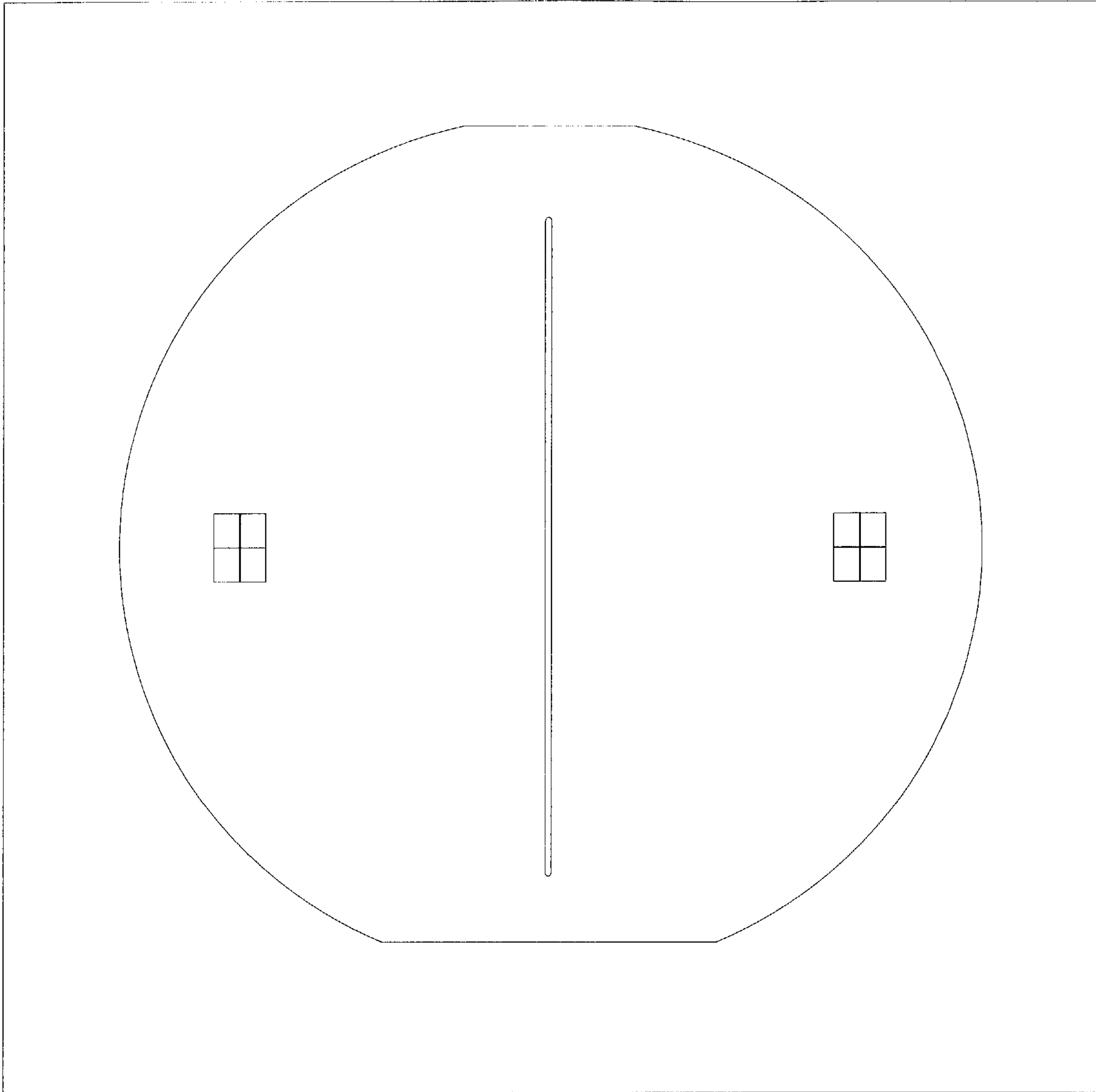

Figure A-3: Mask layout to define deep trench in 4-point specimens.

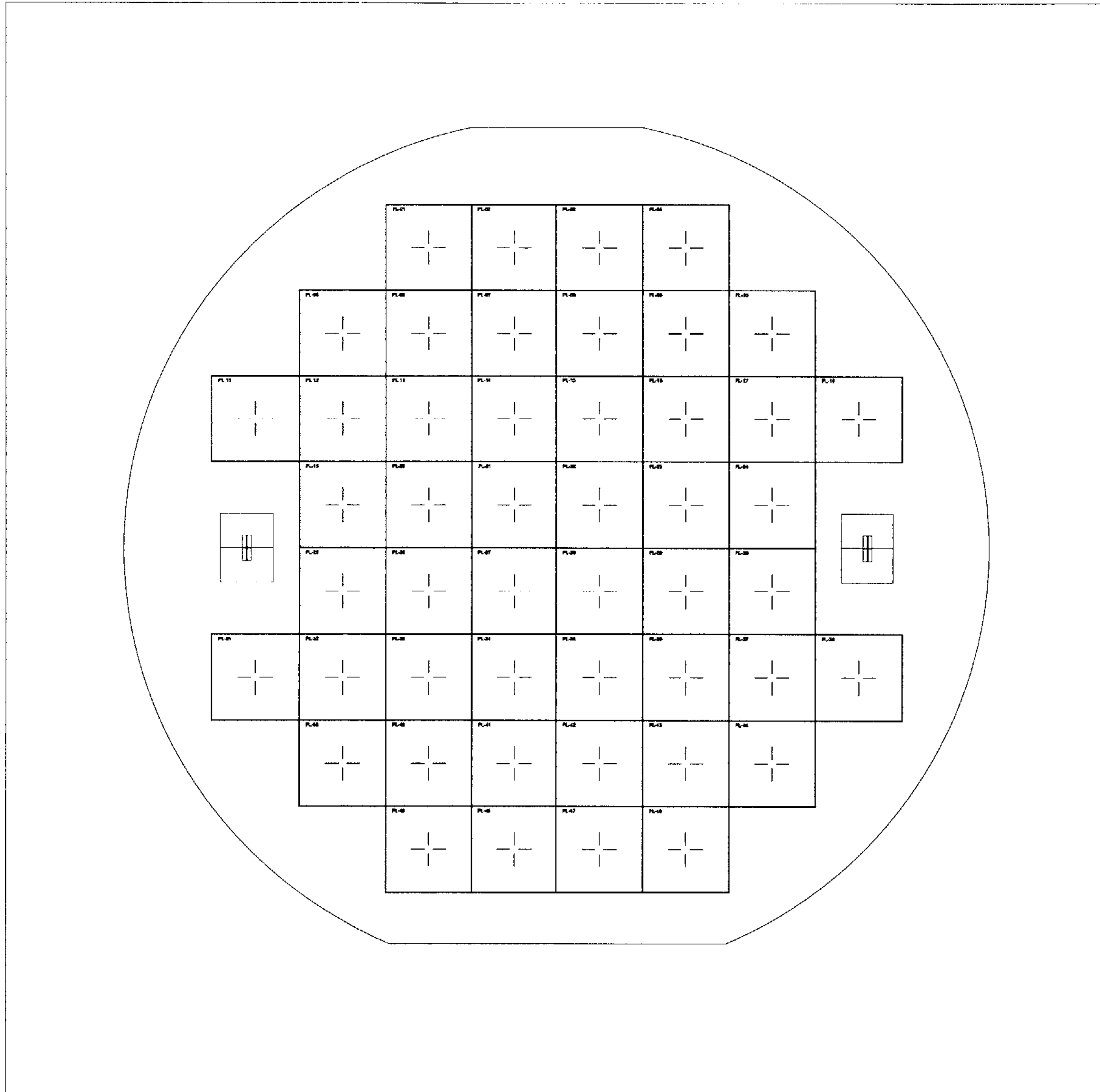

Figure A-4: Mask layout to define alignment marks and specimen edges in device layer of fracture strength specimen.

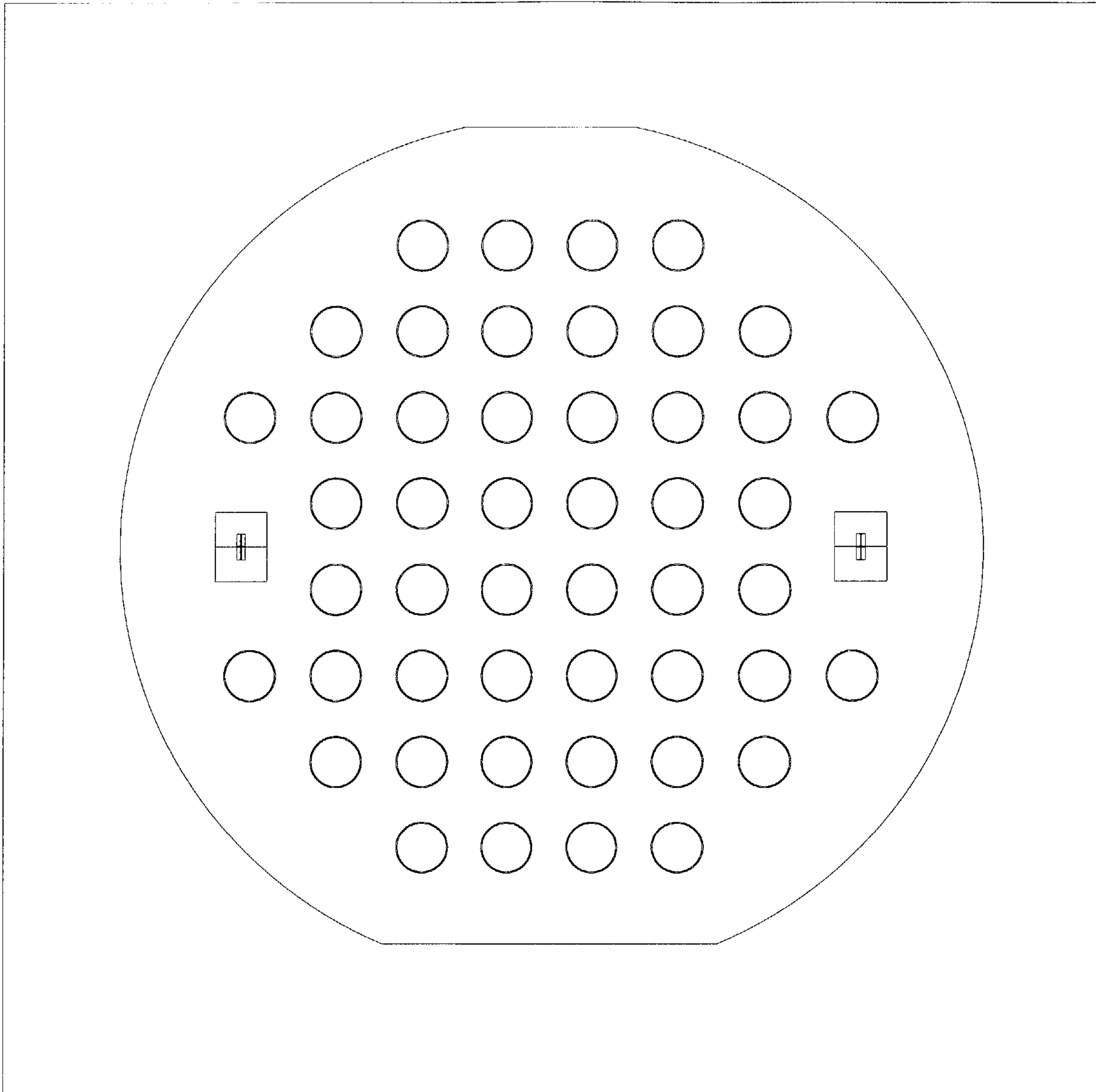

Figure A-5: Mask layout to define deep trenches in handle wafer of fracture strength specimen.

Appendix B

Finite Element Code

Silicon membrane specimen finite element model: 3-D main model.

```
! si_mainmodel.txt

! This is a 3-D model of the silicon membrane specimen (half
!   model).  It is used to determine the effect of off-center
!   loading on the stress in the fillet.

! This model includes the basic structure of the specimen,
!   but does not include the fillet at the base of the
!   trench.  To determine the stresses in the actual fillet,
!   this model must be run in conjunction with
!   si_submodel.txt, which includes the fillet geometry.
!   The results of this model are transferred and used in
!   si_submodel.txt, using the ANSYS submodeling technique.

! This is a linear model.

! The units used in the model are N, mm, s

finish
/clear

/filname,si_mainmodel.txt
/title,Coarse Model

/prep7
csys,1

!---Geometry---

r1 = 3000.0e-3            ! outer radius
r2 = 2850.0e-3            ! inner radius
r3 = 2750.0e-3

z1 = 410.0e-3        ! thickness

z2 = 300.0e-3
z3 = 400.0e-3

eps = 1e-5

!---Mesh Density---

N1=2
N2=2
N3=2
N4=4
N5=3
N6=2
N8=6
N9=48

!---Loading----

Force = -2.0        ! force

NO = 4                     ! offset in elements
os = ((2750/n9)*NO)*.001   ! offset in mm

!---Material Properties---

mp,ex,1,165.0e3
mp,prxy,1,0.22

!---Element Types---

et,1,solid95
et,2,solid45

!---Keypoint Definition---

k,1,0,0,z1
k,2,r3,0,z1
k,3,r2,0,z1
k,4,r1,0,z1
k,5,0,0,z3
k,6,r3,0,z3
k,7,r2,0,z3
k,8,r1,0,z3
k,9,r3,0,z2
k,10,r2,0,z2
k,11,0,0,0
k,12,r2,0,0
k,13,0,0,z2

k,101,0,90,z1
k,201,r3,90,z1
k,301,r2,90,z1
k,401,r1,90,z1
k,501,0,90,z3
k,601,r3,90,z3
k,701,r2,90,z3
k,801,r1,90,z3
k,901,r3,90,z2
k,1001,r2,90,z2
k,1101,0,90,0
k,1201,r2,90,0

k,111,0,180,z1
k,211,r3,180,z1
k,311,r2,180,z1
k,411,r1,180,z1
k,511,0,180,z3
k,611,r3,180,z3
k,711,r2,180,z3
k,811,r1,180,z3
k,911,r3,180,z2
k,1011,r2,180,z2
k,1111,0,180,0
k,1211,r2,180,0

!---Lines---

1,1,2        ! Line 1
1,2,3        ! Line 2
1,3,4        ! Line 3
1,1,5        ! Line 4
1,2,6        ! Line 5
1,3,7        ! Line 6
1,4,8        ! Line 7
1,5,6        ! Line 8
1,6,7        ! Line 9
1,7,8        ! Line 10
1,5,11 ! Line 11
1,6,9        ! Line 12
1,7,10 ! Line 13
1,9,10 ! Line 14
```

```
l,10,12       ! Line 15
l,11,12       ! Line 16

l,1,201       ! Line 17
l,201,301     ! Line 18
l,301,401     ! Line 19
l,201,601     ! Line 20
l,301,701     ! Line 21
l,401,801     ! Line 22
l,5,601       ! Line 23
l,601,701     ! Line 24
l,701,801     ! Line 25
l,601,901     ! Line 26
l,701,1001    ! Line 27
l,901,1001    ! Line 28
l,1001,1201   ! Line 29
l,11,1201     ! Line 30

l,1,211       ! Line 31
l,211,311     ! Line 32
l,311,411     ! Line 33
l,211,611     ! Line 34
l,311,711     ! Line 35
l,411,811     ! Line 36
l,5,611       ! Line 37
l,611,711     ! Line 38
l,711,811     ! Line 39
l,611,911     ! Line 40
l,711,1011    ! Line 41
l,911,1011    ! Line 42
l,1011,1211   ! Line 43
l,11,1211     ! Line 44

larc,4,401,1,r1            ! Arc 1 Line 45
larc,3,301,1,r2            ! Arc 2 Line 46
larc,2,201,1,r3            ! Arc 3 Line 47
larc,8,801,5,r1            ! Arc 4 Line 48
larc,7,701,5,r2            ! Arc 5 Line 49
larc,6,601,5,r3            ! Arc 6 Line 50
larc,10,1001,13,r2  ! Arc 7 Line 51
larc,9,901,13,r3           ! Arc 8 Line 52
larc,12,1201,11,r2  ! Arc 9 Line 53

larc,411,401,1,r1          ! Arc 10 Line 54
larc,311,301,1,r2          ! Arc 11 Line 55
larc,211,201,1,r3          ! Arc 12 Line 56
larc,811,801,5,r1          ! Arc 13 Line 57
larc,711,701,5,r2          ! Arc 14 Line 58
larc,611,601,5,r3          ! Arc 15 Line 59
larc,1011,1001,13,r2       ! Arc 16 Line 60
larc,911,901,13,r3  ! Arc 17 Line 61
larc,1211,1201,11,r2       ! Arc 18 Line 62

!---Areas---

al,1,4,5,8                 ! Area 1
al,2,5,6,9                 ! Area 2
al,3,6,7,10                ! Area 3
al,8,11,12,14,15,16 ! Area 4
al,9,12,13,14       ! Area 5
al,17,4,20,23              ! Area 6
al,18,20,21,24      ! Area 7
al,19,21,22,25      ! Area 8
al,23,11,26,28,29,30       ! Area 9
al,24,26,27,28             ! Area 10
al,31,4,34,37              ! Area 11
al,32,34,35,38             ! Area 12
al,33,35,36,39             ! Area 13
al,37,43,40,42,11,44       ! Area 14
al,38,40,41,42             ! Area 15

al,7,22,45,48       ! Area 16
al,48,49,10,25             ! Area 17
al,13,27,49,51             ! Area 18
al,15,29,51,53             ! Area 19
al,16,30,53                ! Area 20
al,30,44,62                ! Area 21
al,29,43,62,60             ! Area 22
al,27,41,60,58             ! Area 23
al,25,39,58,57             ! Area 24
al,22,36,54,57             ! Area 25
al,19,33,54,55             ! Area 26
al,18,32,55,56             ! Area 27
al,17,31,56                ! Area 28
al,1,17,47                 ! Area 29
al,2,18,47,46       ! Area 30
al,3,19,46,45       ! Area 31

al,9,24,49,50       ! Area 32
al,8,23,50                 ! Area 33
al,23,37,59                ! Area 34
al,24,38,58,59             ! Area 35
al,21,35,58,55             ! Area 36
al,20,34,59,56             ! Area 37
al,5,20,47,50       ! Area 38
al,6,21,46,49       ! Area 39
al,12,26,50,52             ! Area 40
al,14,28,51,52             ! Area 41
al,26,40,59,61             ! Area 42
al,28,42,60,61             ! Area 43

!---Volumes---

va,13,8,24,25,26,36 ! Volume 1
va,12,7,27,35,36,37 ! Volume 2
va,11,6,34,37,28           ! Volume 3
va,1,6,29,33,38            ! Volume 4
va,2,7,30,32,38,39  ! Volume 5
va,3,8,31,16,17,39  ! Volume 6
va,15,10,23,35,42,43       ! Volume 7
va,14,9,34,21,22,43,42     ! Volume 8
va,4,9,33,40,41,19,20   ! Volume 9
va,5,10,32,18,40,41 ! Volume 10

!---Mesh Definition---

lsel,s,line,,4,7
lsel,a,line,,20,22
lsel,a,line,,34,36
lesize,all,,,N1

lsel,s,line,,12,13
lsel,a,line,,26,27
lsel,a,line,,40,41
lesize,all,,,N2
```

Silicon membrane specimen finite element model: 3-D main model (cont'd).

```
lsel,s,line,,15,15
lsel,a,line,,29,29
lsel,a,line,,43,43
lesize,all,,,N3

lsel,s,line,,11,11
lesize,all,,,N4

lsel,s,line,,3,3
lsel,a,line,,19,19
lsel,a,line,,33,33
lsel,s,line,,10,10
lsel,a,line,,25,25
lsel,a,line,,39,39
lesize,all,,,N5

lsel,s,line,,2,2
lsel,a,line,,9,9
lsel,a,line,,14,14
lsel,s,line,,18,18
lsel,a,line,,24,24
lsel,a,line,,28,28
lsel,s,line,,32,32
lsel,a,line,,38,38
lsel,a,line,,42,42
lesize,all,,,N6

lsel,s,line,,16,16
lsel,a,line,,30,30
lsel,a,line,,44,44
lsel,a,line,,53,53
lsel,a,line,,62,62
lesize,all,,,N8

lsel,s,line,,45,52
lsel,a,line,,54,61
lesize,all,,,N9

!---Mesh Volumes---

vsel,s,volu,,3,4
type,2
mshape,0,3D
vmesh,all

vsel,s,volu,,1,2
vsel,a,volu,,5,7
vsel,a,volu,,10,10
type,1
mshape,0,3D
vmesh,all

vsel,s,volu,,8,9
type,1
mshape,1,3D
vmesh,all

!---Boundary Conditions---

nsel,s,loc,x,r1-eps,r1+eps        ! fix outer edge
d,all,all,0

csys,0

nsel,s,loc,y,0-eps,0+eps          ! symmetry BC
d,all,uy,0

csys,1

alls

!---Solve---

/solu

antype,static

nsel,s,loc,z,z1-eps,z1+eps
nsel,r,loc,y,0-eps,0+eps
nsel,r,loc,x,(0+os)-eps,(0+os)+eps
f,all,fz,force

alls

save
solve
save
finish

/post1
nsel,s,loc,z,z1-eps,z1+eps
nsel,r,loc,x,r2-eps,r2+eps
nsel,u,loc,y,0+eps,45-eps
nsel,u,loc,y,45+eps,90-eps
nsel,u,loc,y,90+eps,135-eps
nsel,u,loc,y,135+eps,180-eps

prnsol,u,z
alls
```

Silicon membrane specimen finite element model: 3-D main model (cont'd).

```
! si_submodel.txt

! This is a 3-D model of the fillet of the silicon membrane
!   specimen (half model).  It is used to determine the
!   effect of off-center loading on the stress in the fillet.
!   This model is only the fillet and serves as a submodel,
!   this file uses information from si_mainmodel.txt and thus
!   it must be run before using this model.

! The fillet is assumed to be a quarter circle.

! This is a linear model.

! The units used in the model are N, mm, s

finish
/clear

/filname,si_submodel
/title,Sub Model

/prep7
csys,1

!---Geometry---

cr = 2750.0e-3
x1 = cr+90.0e-3
x2 = cr+100.0e-3
x3 = cr+200.0e-3

rad = 5.0e-3                    ! fillet radius
fildist = (rad-(rad/(2.0**0.5)))

cz=(300e-3)-rad

z1=cz+100e-3
z2=cz+rad+100e-3
z3=cz+rad+110e-3

sp1=45
sp2=90
sp3=135
sp4=180

eps=1e-5

!---Mesh Density---

N1=2
N2=3
N3=2
N4=N2
N5=2
N6=87
N7=22

!---Material Properties---

mp,ex,1,165.0e3
mp,prxy,1,0.22

!---Element Type---

et,1,solid95

!---Keypoints---

k,1,cr,0,z3
k,2,x1,0,z3
k,3,x2+rad,0,z3
k,4,x3,0,z3
k,5,cr,0,z1
k,6,x1,0,z1
k,7,x2,0,z1
k,8,x2+fildist,0,z2-fildist
k,9,x2+rad,0,z2
k,10,x3,0,z2
k,11,cr,0,cz
k,12,x1,0,cz
k,13,x2,0,cz

k,14,cr,sp1,z3
k,15,x1,sp1,z3
k,16,x2+rad,sp1,z3
k,17,x3,sp1,z3
k,18,cr,sp1,z1
k,19,x1,sp1,z1
k,20,x2,sp1,z1
k,21,x2+fildist,sp1,z2-fildist
k,22,x2+rad,sp1,z2
k,23,x3,sp1,z2
k,24,cr,sp1,cz
k,25,x1,sp1,cz
k,26,x2,sp1,cz

k,27,cr,sp2,z3
k,28,x1,sp2,z3
k,29,x2+rad,sp2,z3
k,30,x3,sp2,z3
k,31,cr,sp2,z1
k,32,x1,sp2,z1
k,33,x2,sp2,z1
k,34,x2+fildist,sp2,z2-fildist
k,35,x2+rad,sp2,z2
k,36,x3,sp2,z2
k,37,cr,sp2,cz
k,38,x1,sp2,cz
k,39,x2,sp2,cz

k,101,cr,sp3,z3
k,201,x1,sp3,z3
k,301,x2+rad,sp3,z3
k,401,x3,sp3,z3
k,501,cr,sp3,z1
k,601,x1,sp3,z1
k,701,x2,sp3,z1
k,801,x2+fildist,sp3,z2-fildist
k,901,x2+rad,sp3,z2
k,1001,x3,sp3,z2
k,1101,cr,sp3,cz
k,1201,x1,sp3,cz
k,1301,x2,sp3,cz

k,1401,cr,sp4,z3
k,1501,x1,sp4,z3
```

```
k,1601,x2+rad,sp4,z3
k,1701,x3,sp4,z3
k,1801,cr,sp4,z1
k,1901,x1,sp4,z1
k,2001,x2,sp4,z1
k,2101,x2+fildist,sp4,z2-fildist
k,2201,x2+rad,sp4,z2
k,2301,x3,sp4,z2
k,2401,cr,sp4,cz
k,2501,x1,sp4,cz
k,2601,x2,sp4,cz

!---Lines---

l,1,2               ! Line 1
l,2,3               ! Line 2
l,3,4               ! Line 3
l,1,5               ! Line 4
l,2,6               ! Line 5
l,2,8               ! Line 6
l,3,9               ! Line 7
l,4,10              ! Line 8
l,5,6               ! Line 9
l,6,7               ! Line 10
l,9,10              ! Line 11
l,5,11              ! Line 12
l,6,12              ! Line 13
l,7,13              ! Line 14
l,11,12             ! Line 15
l,12,13             ! Line 16

l,14,15             ! Line 17
l,15,16             ! Line 18
l,16,17             ! Line 19
l,14,18             ! Line 20
l,15,19             ! Line 21
l,15,21             ! Line 22
l,16,22             ! Line 23
l,17,23             ! Line 24
l,18,19             ! Line 25
l,19,20             ! Line 26
l,22,23             ! Line 27
l,18,24             ! Line 28
l,19,25             ! Line 29
l,20,26             ! Line 30
l,24,25             ! Line 31
l,25,26             ! Line 32

l,27,28             ! Line 33
l,28,29             ! Line 34
l,29,30             ! Line 35
l,27,31             ! Line 36
l,28,32             ! Line 37
l,28,34             ! Line 38
l,29,35             ! Line 39
l,30,36             ! Line 40
l,31,32             ! Line 41
l,32,33             ! Line 42
l,35,36             ! Line 43
l,31,37             ! Line 44
l,32,38             ! Line 45
l,33,39             ! Line 46
l,37,38             ! Line 47
l,38,39             ! Line 48

l,4,17              ! Line 49
l,3,16              ! Line 50
l,2,15              ! Line 51
l,1,14              ! Line 52
l,10,23             ! Line 53
l,9,22              ! Line 54
l,8,21              ! Line 55
l,7,20              ! Line 56
l,6,19              ! Line 57
l,5,18              ! Line 58
l,13,26             ! Line 59
l,12,25             ! Line 60
l,11,24             ! Line 61

l,17,30             ! Line 62
l,16,29             ! Line 63
l,15,28             ! Line 64
l,14,27             ! Line 65
l,23,36             ! Line 66
l,22,35             ! Line 67
l,21,34             ! Line 68
l,20,33             ! Line 69
l,19,32             ! Line 70
l,18,31             ! Line 71
l,26,39             ! Line 72
l,25,38             ! Line 73
l,24,37             ! Line 74

larc,7,8,9,rad              ! Line 75
larc,8,9,7,rad              ! Line 76
larc,20,21,22,rad           ! Line 77
larc,21,22,20,rad           ! Line 78
larc,33,34,35,rad           ! Line 79
larc,34,35,33,rad           ! Line 80

l,101,201           ! Line 81
l,201,301           ! Line 82
l,301,401           ! Line 83
l,101,501           ! Line 84
l,201,601           ! Line 85
l,201,801           ! Line 86
l,301,901           ! Line 87
l,401,1001          ! Line 88
l,501,601           ! Line 89
l,601,701           ! Line 90
l,901,1001          ! Line 91
l,501,1101          ! Line 92
l,601,1201          ! Line 93
l,701,1301          ! Line 94
l,1101,1201         ! Line 95
l,1201,1301         ! Line 96

l,1401,1501         ! Line 97
l,1501,1601         ! Line 98
l,1601,1701         ! Line 99
l,1401,1801         ! Line 100
l,1501,1901         ! Line 101
l,1501,2101         ! Line 102
l,1601,2201         ! Line 103
l,1701,2301         ! Line 104
l,1801,1901         ! Line 105
```

Silicon membrane specimen finite element model: 3-D sub-model (cont'd).

```
l,1901,2001           ! Line 106
l,2201,2301           ! Line 107
l,1801,2401           ! Line 108
l,1901,2501           ! Line 109
l,2001,2601           ! Line 110
l,2401,2501           ! Line 111
l,2501,2601           ! Line 112

l,401,1701            ! Line 113
l,301,1601            ! Line 114
l,201,1501            ! Line 115
l,101,1401            ! Line 116
l,1001,2301           ! Line 117
l,901,2201            ! Line 118
l,801,2101            ! Line 119
l,701,2001            ! Line 120
l,601,1901            ! Line 121
l,501,1801            ! Line 122
l,1301,2601           ! Line 123
l,1201,2501           ! Line 124
l,1101,2401           ! Line 125

l,401,30              ! Line 126
l,301,29              ! Line 127
l,201,28              ! Line 128
l,101,27              ! Line 129
l,1001,36             ! Line 130
l,901,35              ! Line 131
l,801,34              ! Line 132
l,701,33              ! Line 133
l,601,32              ! Line 134
l,501,31              ! Line 135
l,1301,39             ! Line 136
l,1201,38             ! Line 137
l,1101,37             ! Line 138

larc,701,801,901,rad              ! Line 139
larc,801,901,701,rad              ! Line 140
larc,2001,2101,2201,rad           ! Line 141
larc,2101,2201,2001,rad           ! Line 142

!---Areas---

al,1,4,5,9            ! Area 1
al,5,6,10,75          ! Area 2
al,2,6,7,76           ! Area 3
al,3,7,8,11           ! Area 4
al,9,12,13,15         ! Area 5
al,10,13,14,16        ! Area 6

al,17,20,21,25        ! Area 7
al,21,22,26,77        ! Area 8
al,18,22,23,78        ! Area 9
al,19,23,24,27        ! Area 10
al,25,28,29,31        ! Area 11
al,26,29,30,32        ! Area 12

al,33,36,37,41        ! Area 13
al,37,38,42,79        ! Area 14
al,34,38,39,80        ! Area 15
al,35,39,40,43        ! Area 16
al,41,44,45,47        ! Area 17
al,42,45,46,48        ! Area 18

al,3,19,49,50         ! Area 19
al,8,24,49,53         ! Area 20
al,11,27,53,54        ! Area 21
al,7,23,50,54         ! Area 22
al,2,18,50,51         ! Area 23
al,76,78,54,55        ! Area 24
al,6,22,51,55         ! Area 25
al,75,77,55,56        ! Area 26
al,10,26,56,57        ! Area 27
al,5,21,51,57         ! Area 28
al,1,17,51,52         ! Area 29
al,4,20,52,58         ! Area 30
al,9,25,58,57         ! Area 31
al,12,28,58,61        ! Area 32
al,15,31,60,61        ! Area 33
al,13,29,57,60        ! Area 34
al,14,30,56,59        ! Area 35
al,16,32,59,60        ! Area 36

al,19,35,62,63        ! Area 37
al,24,40,62,66        ! Area 38
al,27,43,66,67        ! Area 39
al,23,39,63,67        ! Area 40
al,18,34,63,64        ! Area 41
al,78,80,67,68        ! Area 42
al,22,38,64,68        ! Area 43
al,77,79,68,69        ! Area 44
al,21,37,64,70        ! Area 45
al,26,42,69,70        ! Area 46
al,30,46,69,72        ! Area 47
al,32,48,72,73        ! Area 48
al,29,45,70,73        ! Area 49
al,31,47,74,73        ! Area 50
al,28,44,74,71        ! Area 51
al,25,41,71,70        ! Area 52
al,17,33,64,65        ! Area 53
al,20,36,65,71        ! Area 54

al,81,84,85,89        ! Area 55
al,85,86,90,139       ! Area 56
al,82,86,87,140       ! Area 57
al,83,87,88,91        ! Area 58
al,92,89,93,95        ! Area 59
al,90,93,94,96        ! Area 60

al,97,100,101,105     ! Area 61
al,101,102,106,141    ! Area 62
al,98,102,103,142     ! Area 63
al,103,99,104,107     ! Area 64
al,108,105,109,111    ! Area 65
al,106,109,110,112    ! Area 66

al,97,81,116,115      ! Area 67
al,98,82,115,114      ! Area 68
al,99,83,114,113      ! Area 69
al,104,88,113,117     ! Area 70
al,103,87,118,114     ! Area 71
al,102,86,115,119     ! Area 72
al,101,85,115,121     ! Area 73
al,100,84,116,122     ! Area 74
al,105,89,122,121     ! Area 75
al,90,106,121,120     ! Area 76
```

Silicon membrane specimen finite element model: 3-D sub-model (cont'd).

```
al,141,139,120,119  ! Area 77
al,142,140,119,118  ! Area 78
al,107,91,118,117   ! Area 79
al,110,94,120,123   ! Area 80
al,109,93,121,124   ! Area 81
al,108,92,122,125   ! Area 82
al,111,95,125,124   ! Area 83
al,112,96,124,123   ! Area 84

al,33,81,129,128          ! Area 85
al,34,82,128,127          ! Area 86
al,35,83,127,126          ! Area 87
al,40,88,126,130          ! Area 88
al,39,87,127,131          ! Area 89
al,38,86,128,132          ! Area 90
al,37,85,128,134          ! Area 91
al,36,84,129,135          ! Area 92
al,41,89,135,134          ! Area 93
al,42,90,134,133          ! Area 94
al,79,139,133,132         ! Area 95
al,80,140,132,131         ! Area 96
al,43,91,131,130          ! Area 97
al,44,92,135,138          ! Area 98
al,45,93,134,137          ! Area 99
al,46,94,133,136          ! Area 100
al,47,95,138,137          ! Area 101
al,48,96,137,136          ! Area 102

!---Volumes---

va,1,7,28,29,30,31        ! Volume 1
va,2,8,25,26,27,28        ! Volume 2
va,3,9,22,23,24,25        ! Volume 3
va,4,10,19,20,21,22       ! Volume 4
va,5,11,31,32,33,34       ! Volume 5
va,6,12,27,34,35,36       ! Volume 6

va,7,13,45,52,53,54       ! Volume 7
va,8,14,43,44,45,46       ! Volume 8
va,9,15,40,41,42,43       ! Volume 9
va,10,16,37,38,39,40      ! Volume 10
va,11,17,49,50,51,52      ! Volume 11
va,12,18,46,47,48,49      ! Volume 12

va,61,55,67,73,74,75      ! Volume 13
va,62,56,72,73,76,77      ! Volume 14
va,63,57,68,71,72,78      ! Volume 15
va,64,58,69,70,71,79      ! Volume 16
va,65,59,75,81,82,83      ! Volume 17
va,66,60,80,81,76,84      ! Volume 18

va,55,13,85,91,92,93      ! Volume 19
va,56,14,90,91,94,95      ! Volume 20
va,57,15,86,89,90,96      ! Volume 21
va,58,16,87,88,89,97      ! Volume 22
va,59,17,93,98,99,101     ! Volume 23
va,60,18,94,99,100,102    ! Volume 24

!---Mesh Definition---

lsel,s,line,,3,3
lsel,a,line,,19,19
lsel,a,line,,35,35
lsel,a,line,,83
lsel,a,line,,99
lesize,all,,,N1

lsel,s,line,,3
lsel,a,line,,6
lsel,a,line,,10
lsel,a,line,,18
lsel,a,line,,22
lsel,a,line,,26
lsel,a,line,,32
lsel,a,line,,34
lsel,a,line,,38
lsel,a,line,,42
lsel,a,line,,48
lsel,a,line,,82
lsel,a,line,,86
lsel,a,line,,106
lsel,a,line,,96
lsel,a,line,,98
lsel,a,line,,102
lsel,a,line,,106
lsel,a,line,,112
lesize,all,,,N2

lsel,s,line,,1
lsel,a,line,,9
lsel,a,line,,15
lsel,a,line,,17
lsel,a,line,,25
lsel,a,line,,31
lsel,a,line,,33
lsel,a,line,,41
lsel,a,line,,47
lsel,a,line,,81
lsel,a,line,,89
lsel,a,line,,95
lsel,a,line,,97
lsel,a,line,,105
lsel,a,line,,111

lesize,all,,,N3

lsel,s,line,,4,8
lsel,a,line,,20,24
lsel,a,line,,36,40
lsel,a,line,,84,88
lsel,a,line,,100,104

lesize,all,,,N4

lsel,s,line,,12,14
lsel,a,line,,28,30
lsel,a,line,,44,46
lsel,a,line,,92,94
lsel,a,line,,108,110

lesize,all,,,N5

lsel,s,line,,49,51
lsel,a,line,,53,57
lsel,a,line,,59,60
lsel,a,line,,62,64
```

```
lsel,a,line,,66,70
lsel,a,line,,72,73
lsel,a,line,,113,115
lsel,a,line,,117,121
lsel,a,line,,123,124
lsel,a,line,,126,128
lsel,a,line,,130,134
lsel,a,line,,136,137

lesize,all,,,N6

lsel,s,line,,52
lsel,a,line,,65
lsel,a,line,,116
lsel,a,line,,129
lsel,a,line,,58
lsel,a,line,,71
lsel,a,line,,122
lsel,a,line,,135
lsel,a,line,,61
lsel,a,line,,74
lsel,a,line,,125
lsel,a,line,,138

lesize,all,,,N7

!---Mesh Volumes---

vsel,s,volu,,2,4
vsel,a,volu,,6
vsel,a,volu,,8,10
vsel,a,volu,,12
vsel,a,volu,,14,16
vsel,a,volu,,18
vsel,a,volu,,20,22
vsel,a,volu,,24
mshape,0,3D
vmesh,all

vsel,s,volu,,1
vsel,a,volu,,5
vsel,a,volu,,7
vsel,a,volu,,11
vsel,a,volu,,13
vsel,a,volu,,17
vsel,a,volu,,19
vsel,a,volu,,23
mshape,1,3D
vmesh,all

!---Boundary Conditions---

csys,0
nsel,s,loc,y,0-eps,0+eps
d,all,uy,0
csys,1

!---Cut Boundaries---
nsel,s,loc,x,cr-eps,cr+eps

nsel,a,loc,z,cz-eps,cz+eps
nsel,a,loc,x,x3-eps,x3+eps
nwrite

!---Write to database---

alls
save

!---Resume database from coarse model and obtain data--

resume,si_mainmodel,db

/post1
file,si_mainmodel,rst
set
cbdof
finish

!---Resume the submodel database---
resume,

!---Solve----

/solu
antype,static
/input,,cbdo

alls
solve
save
finish


!---Post Processing---
/post1
rsys,1

nsel,s,loc,z,z3-eps,z3+eps
nsel,r,loc,x,Cr-eps,Cr+eps
nsel,u,loc,y,0+eps,45-eps
nsel,u,loc,y,45+eps,90-eps
nsel,u,loc,y,90+eps,135-eps
nsel,u,loc,y,135+eps,180-eps
prnsol,u,z

nsel,s,loc,z,z3-eps,z3+eps
nsel,r,loc,x,x3-eps,x3+eps
nsel,u,loc,y,0+eps,45-eps
nsel,u,loc,y,45+eps,90-eps
nsel,u,loc,y,90+eps,135-eps
nsel,u,loc,y,135+eps,180-eps
prnsol,u,z

dsys,1
rsys,1
nsel,s,loc,x,x2+rad-eps,x2+rad+eps
nsel,r,loc,z,z2-eps,z2+eps
nsort,loc,y,1,0
/page,1000,80,1000,132
/output,check,txt,~/,append
prnsol,u,z
prnsol,s
dsys,0
```

Silicon membrane specimen finite element model: 3-D sub-model (cont'd).

```
! si_fracture.txt

! This is a 2-D axisymmetric model of the silicon membrane
!   specimen.  It is used to determine the maximum stress in
!   the specimen for a given geometry and load.

! The fillet is assumed to be an ellipse and the aspect ratio
!   can be varied from 0.1 to 1.0 (quarter circle).  An aspect
!   ratio of 0.5 is believed to be the most realistic for the
!   current specimens.

! This is a non-linear model.

! Note that all units are given in mm and N, for some
!   reason the program will not mesh arcs less than 10e-6. Thus
!   we use mm as our base unit of length and everything works
!   fine.

finish
/clear,nostart

/filename,si_fracture.txt
/title,Membrane Study

/prep7


!---Geometry---

tether = 0.155
Rmid = (2.845+3.00)/2.0
Ri = Rmid-tether/2.0        ! membrane inner diameter
Ro = Rmid+tether/2.0        ! membrane outer diameter
Rd = 3.500                  ! die outer diameter
Rm = 200.0e-3               ! mesh parameter
tm = 17.53e-3               ! membrane thickness
tw = 400.0e-3               ! wafer thickness
L =  15.0e-3                ! length of fillet from top
H =  0.50*L
RHL = H/L
RF = L

!---Load---

force = 10.0        ! force applied in newtons

!---Variables---

r1 = Ri-Rm
r2 = Ri-tm
r3 = Ri
r5 = Ri+L
r6 = Ro-L
r8 = Ro
r9 = Ro+tm
r10 = Ro+Rm
r11 = Rd

h1 = tm
h3 = tm+H
h4 = tm+Rm
h5 = tw

!---Mesh Parameters---

N1 = 50
N2 = 6
N3 = 6
N4 = 15
N5 = 3
N6 = 48
N7 = 4

eps = 1e-10

!---Coordinate Systems---

local,11,1,r5,h3,0,0,0,0,RHL
local,12,1,r6,h3,0,0,0,0,RHL
csys,0

!---Element Type---

et,1,plane82
keyopt,1,3,1

!---Material Properties---

mp,ex,1,165e3
mp,prxy,1,0.22

!---Keypoints---

csys,0
k,1,0,0
k,2,r1,0
k,3,r2,0
k,4,r5,0
k,5,r6,0
k,6,r9,0
k,7,r10,0
k,8,r11,0
k,9,r5,h1
k,10,r6,h1
k,13,r2,h3
k,14,r3,h3
k,15,r8,h3
k,16,r9,h3
k,17,0,h4
k,18,r1,h4
k,19,r3,h4
k,20,r8,h4
k,21,r10,h4
k,22,r11,h4
k,23,0,h5
k,24,r1,h5
k,25,r3,h5
k,26,r8,h5
k,27,r10,h5
k,28,r11,h5

csys,11
k,11,L,-135,0

csys,12
k,12,L,-45,0
```

Silicon membrane specimen finite element model: 2-D axisymmetric model.

```
!---Lines---

csys,0
l,1,2        ! #1
l,3,2        ! #2
l,3,4        ! #3
l,4,5        ! #4
l,5,6        ! #5
l,6,7        ! #6
l,7,8        ! #7
l,1,17       ! #8
l,2,18       ! #9
l,3,13       ! #10
l,3,11       ! #11
l,4,9        ! #12
l,5,10       ! #13
l,6,12       ! #14
l,6,16       ! #15
l,7,21       ! #16
l,8,22       ! #17
l,17,18      ! #18
l,13,18      ! #19
l,13,14      ! #20

csys,11
l,14,11      ! #21
l,11,9       ! #22

csys,0
l,9,10       ! #23

csys,12
l,10,12      ! #24
l,12,15      ! #25

csys,0
l,16,15      ! #26
l,16,21      ! #27
l,21,22      ! #28
l,18,19      ! #29
l,20,21      ! #30
l,14,19      ! #31
l,15,20      ! #32
l,17,23      ! #33
l,18,24      ! #34
l,19,25      ! #35
l,20,26      ! #36
l,21,27      ! #37
l,22,28      ! #38
l,23,24      ! #39
l,24,25      ! #40
l,26,27      ! #41
l,27,28      ! #42

!---Mesh Density---

lesize,23,,,N1             ! #23
lesize,4,,,N1              ! #4

lsel,s,line,,11,14,3       ! #11,14
lesize,all,,,N2,0.25

lsel,s,line,,12,13         ! #12,13
lsel,a,line,,20,26,6       ! #20,26
lesize,all,,,N2,0.25

lsel,s,line,,29,30         ! #29,30
lsel,a,line,,40,41         ! #40,41
lesize,all,,,N2

lsel,s,line,,3,5,2         ! #3,5
lsel,a,line,,21,22         ! #21,22
lsel,a,line,,24,25         ! #24,25
lesize,all,,,N3

lsel,s,line,,10,15,5       ! #10,15
lsel,a,line,,9,16,7        ! #9,16
lsel,a,line,,8             ! #8
lsel,a,line,,17            ! #17
lesize,all,,,N3

lsel,s,line,,2,6,4         ! #2,6
lsel,a,line,,19,27,8       ! #19,27
lsel,a,line,,31,32         ! #31,32
lesize,all,,,N4,10

lsel,s,line,,33,38         ! #33,34,35,36,37,38
lesize,all,,,N5

lsel,s,line,,1,18,17       ! #1,18
lsel,a,line,,39            ! #39
lesize,all,,,N6

lsel,s,line,,7,28,21       ! #7,28
lsel,a,line,,42            ! #42
lesize,all,,,N7

lsel,all

!---Areas---

al,1,9,18,8  ! #1
al,2,10,19,9 ! #2
al,10,11,21,20      ! #3
al,11,3,12,22! #4
al,12,4,13,23! #5
al,13,5,14,24! #6
al,14,15,26,25      ! #7
al,15,6,16,27! #8
al,16,7,17,28       ! #9
al,18,34,39,33      ! #10
al,34,29,35,40      ! #11
al,36,30,37,41      ! #12
al,37,28,38,42      ! #13
al,19,20,31,29      ! #14
al,32,26,27,30      ! #15

!---Mesh Areas---

asel,s,area,,3,4    ! areas 3,4,6,7
asel,a,area,,6,7
mshape,,2D
amesh,all

asel,s,area,,5,5    ! area 5
```

Silicon membrane specimen finite element model: 2-D axisymmetric model (cont'd).

```
mshape,0,2D
amesh,all

asel,s,area,,14,15  ! areas 14,15
asel,a,area,,2,8,6  ! areas 2,8
mshape,0,2D
amesh,all

asel,s,area,,11,12  ! area 11,12
mshape,0,2D
amesh,all

asel,s,area,,1,1    ! area 1
mshape,0,2D
amesh,all

asel,s,area,,10,10  ! area 10
mshape,0,2D
amesh,all

asel,s,area,,9,9    ! area 9
mshape,0,2D
amesh,all

asel,s,area,,13,13  ! area 13
mshape,0,2D
amesh,all

alls

!---Displacement B.C.---

nsel,s,loc,x,0-eps,0+eps
d,all,ux,0

nsel,s,loc,y,h5-eps,h5+eps
nsel,r,loc,x,r9-eps,r11+eps
!nsel,r,loc,x,3.2-eps,3.2+eps
d,all,uy,0

alls

!---Solve---

/solu
antype,static

nsel,s,loc,x,0-eps,0+eps
nsel,r,loc,y,0-eps,0+eps
f,all,FY,force

nlgeom,on
nropt,full,,off
sstif,on
autots,on
lnsrch,on
neqit,30
cnvtol,f,,0.005,2,1e-8
nsubst

alls

save

solve
finish

!---Post Processing---

/post1
nsel,s,loc,x,r2-eps,r2+eps
nsel,r,loc,y,h3-eps,h3+eps

prnsol,u,y

nsel,all
esel,all
plnsol,s,1

nsel,s,loc,x,(Ri+L-eps),(Ri+L+eps)
nsel,r,loc,y,(tm*(1-0.29874166*1/4)-1e-7),(tm*(1-0.29874166*1/4)+1e-7)
prnsol,s,prin

nsel,s,loc,x,Ri-eps,Rd+eps
```

Silicon membrane specimen finite element model: 2-D axisymmetric model (cont'd).

References

[1] Seward Webb Pulitzer III. Feasibility assessment and design of micro hydraulic solid-state transducers. Master's thesis, Massachusetts Institute of Technology, 1998.

[2] N.W. Hagood IV, D.C. Roberts, L. Saggere, M.A. Schmidt, M. Spearing, K.S. Breuer, R. Mlcak, J.A. Carretero, F. Ganji, H. Li, K.-S. Chen, Y.-H. Su, and S. Pulitzer. Development of micro-hydraulic transducer technology. In *The 10th International Conference on Adaptive Structures and Technologies (ICAST '99)*, October 1999.

[3] N.W. Hagood, D.C. Roberts, L. Saggere, K.S. Breuer, K.-S. Chen, J.A. Carretero, H. Li, R. Mlcak, S. Pulitzer, M.A. Schmidt, S.M. Spearing, and Y.-H. Su. Micro hydraulic transducer technology for actuation and power generation. In *Proceedings of the SPIE: Smart Structures and Materials 2000-Smart Structures and Integrated Systems*, volume 3985, pages 680–688, 2000.

[4] D.C. Roberts, J.L. Steyn, H. Li, K.T. Turner, R. Mlcak, L. Saggere, S.M. Spearing, M.A. Schmidt, and N.W. Hagood. A high-frequency, high-stiffness piezoelectric micro-actuator for hydraulic applications. In *Transducers '01*, 2001.

[5] H. Q. Li, D. C. Roberts, J. L. Steyn, K. T. Turner, J. A. Carretero, O. Yaglioglu, Y.-H. Su, L. Saggere, N. W. Hagood, S. M. Spearing, M.A. Schmidt, R. Mlcak, and K. S. Breuer. A high frequency high flow rate piezoelectrically driven MEMS micropump. In *Solid-State Sensor and Actuator Workshop 2000*, pages 69–72, June 2000.

[6] G. Wallis and D.I. Pomerantz. Field assisted glass-metal sealing. *Journal of Applied Physics*, 40(10):3946–3949, 1969.

[7] E. H. Klaassen, K. Petersen, M. J. Noworolski, J. Logan, N. I. Maluf, J. Brown, C. Storment, W. McCulley, and G. A. Kovacs. Silicon fusion bonding and deep reactive ion etching: a new technology for microstructures. *Sensors and Actuators*, A52:132–139, 1996.

[8] M. A. Schmidt. Wafer-to-wafer bonding for microstructure formation. *Proceedings of the IEEE*, 86(8):1575–1585, August 1998.

[9] A.R. Mizra and A.A. Ayon. Silicon wafer bonding: key to high-volume manufacturing. *Sensors*, December 1998.

[10] A. Mehra, A. Ayon, I.A. Waitz, and M.A. Schmidt. Microfabrication of high-temperature silicon devices using wafer bonding and deep reactive ion etching. *Journal of Microelectromechanical Systems*, 8(2):152–156, 1999.

[11] H.-J. Kress, F. Bantien, J. Marek, and M. Willmann. Silicon pressure sensor with integrated CMOS signal-conditioning circuit and compensation of temperature coefficient. *Sensors and Actuators*, 25(1):21–26, 1990.

[12] L. Spangler and C.J. Kemp. ISAAC-integrated silicon automotive accelerometer. In *Transducers '95*, pages 25–29, 1995.

[13] P. Krause, M. Sporys, E. Obermeier, K. Lange, and S. Grigull. Silicon to silicon anodic bonding using evaporated glass. In *Transducers '95*, pages 228–231, 1995.

[14] S. Weichel, Roger de Reus, and Michael Lindahl. Silicon-to-silicon wafer bonding using evaporated glass. *Sensors and Actuators*, A70:179–184, 1998.

[15] Bruno Miller. Hybrid silicon/silicon carbide microstructures and silicon bond strength tests for the MIT microengine. Master's thesis, Massachusetts Institute of Technology, 1998.

[16] K.T. Turner, A.A. Ayon, D. Choi, B. Miller, and S.M. Spearing. Characterization of silicon fusion bonds using a four-point bend specimen. In *Materials Science of Microelectromechanical Systems (MEMS) Devices III*, volume 657. MRS, September 2000.

[17] J.B. Lasky, S.R. Stiffler, F.R. White, and J.R. Abernathy. Silicon-on-insulator (SOI) by bonding and etch-back. In *International Electron Devices Meeting. Technical Digest*, pages 684–687. IEEE, 1985.

[18] J.B. Lasky. Wafer bonding for silicon on insulator technologies. *Applied Physics Letters*, 48(1):78–80, 1986.

[19] M. Shimbo, K. Furukawa, K. Fukuda, and K. Tanzawa. Silicon-to-silicon direct bonding method. *Journal of Applied Physics*, 60(8):2987–2989, 1986.

[20] U. Gosele and Q.-Y. Tong. Semiconductor wafer bonding. *Annual Review of Materials Science*, 28:215–241, 1998.

[21] U. Gosele, Y. Bluhm, G. Kastner, P. Kopperschmidt, G. Krauter, R. Scholz, A. Schumacher, St. Senz, Q.-Y. Tong, L.-J. Huang, Y.-L. Chao, and T.H. Lee. Fundamental issues in wafer bonding. *Journal of Vacuum Science and Technology A*, 17(4):1145–1152, 1999.

[22] Q.-Y. Tong and U. Gosele. *Semiconductor wafer bonding : science and technology*. Wiley, New York, 1999.

[23] Q.-Y. Tong, G. Cha, R. Gafiteanu, and U. Gosele. Low temperature wafer direct bonding. *Journal of Microelectromechanical Systems*, 3(1):29–35, 1994.

[24] B.E. Roberds and S.N. Farrens. Low temperature silicon direct bonding. In *Proceeding of the First International Symposium on Semiconductor Wafer Bonding: Science, Technology, and Applications*, pages 240–248, 1992.

[25] S.N. Farrens, B.E. Roberds, J.K. Smith, and C.E. Hunt. Analysis of bond characteristics in Si direct-bonded materials. In *Proceeding of the Second International*

Symposium on Semiconductor Wafer Bonding: Science, Technology, and Applications, pages 81–95, 1993.

[26] W.P. Mazara, G. Goetz, A. Caviglia, and B. McKitterick. Bonding of silicon wafers for silicon on insulator. *Journal of Applied Physics*, 64(10):4943–4950, 1988.

[27] H.C. Cao and A.G. Evans. An experimental study of the fracture resistance of bimaterial interfaces. *Mechanics of Materials*, 7:295–304, 1989.

[28] T. Martini, J. Steinkirchner, and U. Gosele. The crack opening method in silicon wafer bonding: how useful is it? *Journal of the Electrochemical Society*, 144(1):354–357, 1997.

[29] P.G. Charalambides, J. Lund, A.G. Evans, and R.M. McMeeking. A test specimen for determining the fracture resistance of bimaterial interfaces. *Journal of Applied Mechanics*, 56:77–82, 1989.

[30] P.G. Charalambides, H.C. Cao, J. Lund, and A.G. Evans. Development of a test method for measuring the mixed mode fracture resistance of bimaterial interfaces. *Mechanics of Materials*, 8:269–283, 1990.

[31] C.H. Tsau, M.A. Schmidt, and S.M. Spearing. Characterization of low temperature, wafer-level gold-gold thermocompression bonds. In *Materials Science of Microelectromechanical Systems (MEMS) Devices II*, volume 605, pages 171–176. MRS, September 1999.

[32] M.-Y. He and J.W. Hutchinson. Crack deflection at an interface between dissimilar elastic materials. *International Journal of Solids and Structures*, 25(9):1053–1067, 1989.

[33] Personal communication with David C. Roberts.

[34] K.E. Petersen. Silicon as a mechanical material. *Proceedings of the IEEE*, 70(5):420–457, 1982.

[35] S.M. Hu. Critical stress in silicon brittle fracture, and effect of ion implantation and other surface treatments. *Journal of Applied Physics*, 53(5):3576–3580, 1982.

[36] C.J. Wilson, A. Omeggi, and M. Narbutovskih. Fracture testing of silicon microcantilever beams. *Journal of Applied Physics*, 79(5):2386–2393, 1996.

[37] K.-S. Chen, A.A. Ayon, K.A. Lohner, M.A. Kepets, T.K. Melconian, and S.M. Spearing. Dependence of silicon fracture strength and surface morphology on deep reactive ion etching parameters. In *Materials Science of Microelectromechanical Systems (MEMS) Devices*, volume 546, pages 21–26. MRS, September 1998.

[38] K.-S. Chen. *Materials characterization and structural design of ceremic micro turbomachinery.* PhD thesis, Massachusetts Institute of Technology, 1999.

[39] K.-S. Chen, A. Ayon, and S.M. Spearing. Controlling and testing the fracture strength of silicon on the mesoscale. *Journal of the American Ceramic Society*, 83(6):1476–1484, 2000.

[40] C.P. Chen and M.H. Leipold. Fracture toughness of silicon. *Ceramic Bulletin*, 59(4):469–472, 1980.

[41] F. Ericson, S. Johansson, and J.-A. Schweitz. Hardness and fracture toughness of semiconducting materials studied by indentation and erosion techniques. *Materials Science and Engineering*, A105/106:131–141, 1988.

[42] J.J. Wortman and R.A. Evans. Young's modulus, shear modulus, and poisson's ratio in silicon and germanium. *Journal of Applied Physics*, 36(1):153–156, 1965.

[43] G.S. Selvaduray. Die bond materials and bonding mechnaisms in microelectronic packaging. *Thin Solid Films*, 153:431–445, 1987.

[44] R.K. Shukla and N.P. Mencinger. A critical review of VLSI die-attachment in high reliability applications. *Solid State Technology*, pages 67–74, July 1985.

[45] G. Sasaki, H. Fukunaga, T. Suga, and K. Tanaka. Mechanism of the anodic bonding between PZT ceramics and silicon wafer. *Materials Chemistry and Physics*, 51:174–177, 1997.

[46] K. Tanaka, E. Takata, and K. Ohwada. Anodic bonding of lead zirconate titanate ceramics to silicon with intermediate glass layer. *Sensors and Actuators*, A69:199–203, 1998.

[47] A.-L. Tiensuu, M. Bexell, J.A. Schweitz, L. Smith, and S. Johansson. Assembling three-dimensional microstructurea using gold-silicon eutectic bonding. *Sensors and Actuators*, A45:227–236, 1994.

[48] P.T. Vianco and J.A. Rejent. Solder bond applications in a piezoelectric sensor assembly. In *Forty-Fifth Annual Symposium on Frequency Control*, pages 266–280. IEEE, 1991.

[49] D.R. Olsen and H.M. Berg. Properties of die bond alloys relating to thermal fatigue. *IEEE Transactions on Components, Hybrids, and Manufacturing Technology*, CHMT-2(2):257–263, 1979.

[50] C. Kallmayer, D. Lin, J. Kloeser, H. Opperman, E. Zakel, and H. Reichl. Fluxless flip-chip attcahment techniques using the Au/Sn metallurgy. In *Proceedings of the Seventeenth Electronic Manufacturing Technology Symposium*, pages 20–28. IEEE, 1995.

[51] Eniko T. Enikov and J.G. Boyd. Electroplated-fluidic interconnects for chemical sensors. *Sensors and Actuators*, A84:161–164, 2000.

[52] S.D. Senturia. *Microsystem Design.* Kluwer, Boston, MA, 2001.

[53] H. Okamato and T.B. Massalski. *Phase Diagrams of Binary Gold Alloys.* ASM International, Metals Park, OH, 1987.

[54] G.S. Matijasevic, C.C. Lee, and C.Y. Wang. Au-Sn alloy phase diagram and properties related to its use as a bonding medium. *Thin Sold Films*, 223:276–1287, 1993.

[55] C.C. Lee and G.S. Matijasevic. Highly reliable die attachment on polished GaAs surfaces using gold-tin eutectic alloy. *IEEE Transactions on Components, Hybrids, and Manufacturing Technology*, 12(3):406–409, 1989.

[56] G.S. Matijasevic and C.C. Lee. A reliability study of Au-Sn eutectic bonding with GaAs dice. In *Proceeding of the 27th Annual Reliability Physics Symposium*, pages 137–140. IEEE, 1989.

[57] G.S. Matijasevic, C.Y. Wang, and C.C. Lee. Void free bonding of large silicon dice using gold-tin alloys. *IEEE Transactions on Components, Hybrids, and Manufacturing Technology*, 13(4):1128–1134, 1990.

[58] M. Nishiguchi, N. Goto, and H. Nishizawa. Highly reliable Au-Sn eutectic bonding with back-ground GaAs LSI chips. In *Electronic Manufacturing Technology Symposium, 1990 Proceedings, Competitive Manufacturing for the Next Decade*, pages 216–222. IEEE, 1990.

[59] C.C. Lee, C.Y. Wang, and G.S. Matijasevic. A new bonding technology using gold and tin multilayer composite structures. *IEEE Transactions on Components, Hybrids, and Manufacturing Technology*, 14(2):407–412, 1991.

[60] C. Christensen and S. Bouwstra. Eutectic bonds on wafer scale by thin film multilayers. In *Proceedings of the SPIE: Micromachining and Microfabrication Process Technology II*, volume 2879, pages 288–290, 1996.

[61] G.R. Dohle, J.J. Callahan, K.P. Martin, and T.J. Drabik. Bonding of epitaxial lift off (ELO) devices with AuSn. In *Proceedings of the 45th Electronic Components and Technology Conference*, pages 423–427. IEEE, 1995.

[62] U.S. Department of Defense, Washington D.C. *MIL-STD-883E: Test Methods and Procedures for Microelectronics*, 1996.

[63] M. Ohring. *The Materials Science of Thin Films.* Academic Press, New York, 1992.